Master Thesis

submitted within the UNIGIS MSc programme
at Z_GIS
University of Salzburg

A combined FastScape χ-value and ^{10}Be erosion rate approach to evaluate topographic equilibrium in evolving landscapes: Examples from Namibia and the central Himalaya

by

Dr. Cassandra Fenton
Student ID: 103407

A thesis submitted in partial fulfilment of the requirements of
the degree of
Master of Science (Geographical Information Science & Systems) – MSc (GISc)

Advisor:

Dr. Gudrun Wallentin

Berlin, Germany, 15 July 2015

ACKNOWLEDGMENTS

I would like to thank Drs. Alexandru Codilean, Simon Merrall, and Gudrun Wallentin for their many challenging and useful discussions about this study. I would also like to thank Dr. Jean Braun for providing me with the FastScape_Chi code, and for prompt and thorough answers to my questions about navigating FastScape.

Science Pledge

By my signature below, I certify that my thesis is entirely the result of my own work. I have cited all sources I have used in my thesis and I have always indicated their origin.

Cassandra R. Fen

Berlin, Germany, 14 July 2015

(Place, Date) (Signature)

ABSTRACT

The FastScape landscape evolution model is a powerful, user-friendly tool that can be used in concert with catchment-wide cosmogenic ^{10}Be erosion/denudation rates to assess states of dynamic equilibrium in landscapes set in different tectonic and climatic environments. FastScape computes chi (χ), a proxy for steady-state river channel elevation, at different model times for a given landscape supplied by raster DEMS. Chi values indicate areas or regions of equilibrium or disequilibrium within a given model domain, and not between domains in different geographic study areas. Chi values are sensitive to DEM domain size and base level, cell resolution, and time, thus, chi values can only be meaningfully compared between catchments within a given domain. Mean, non-zero chi values are higher with larger domain size and for coarser DEM cell size. Cross-comparison of chi values between domains with equal surface areas would only be accurate if the same base-level elevation, cell resolution, and domain size were used. Chi can be used to ascertain if anomalously high ^{10}Be erosion rates are affected by the addition of youthful sediment from landslides, debris flows, or glaciation of river catchments or tributary basins; in this study, glacial settings with high erosion rates show no relationship to chi values. For unglaciated tributary basins in a given catchment, chi values are related to cosmogenic ^{10}Be erosion rates in the following ways: (1) basins in equilibrium have chi values that remain constant with increasing cosmogenic erosion rates; (2) basins in disequilibrium have an inverse relationship between chi values and erosion rates in a setting where erosion is driven predominantly by precipitation; and (3) basins in disequilibrium have a positive correlation between chi values and erosion rates in a setting where tectonic uplift is the dominant force driving erosion.

TABLE OF CONTENTS

Chapter Page

LIST OF TABLES

Table Page

LIST OF FIGURES

Figure Page

LIST OF ANIMATIONS

CHAPTER 1: Introduction

Topography is one of the key factors that control many natural processes of interest to humans. Natural hazards, such as floods and mass movements (e.g., debris flows, landslides, etc.) are often directly related to the topography of an area. Steep slopes and cliffs are prone to mass movements. Watersheds with large drainage areas and steep river gradients are prone to destructive floods (Hengl and MacMillan, 2009; Pike, 2000). While the public and media tend to focus on the natural hazards that result from topography, geoscientists have long been interested in the natural processes that create it. The advancement in recent decades of geomorphometry, the common ground of Earth Science and Geographic Information Science (GISc), provides powerful tools to geoscientists for advanced analysis of topography.

An amalgam of earth science, GISc, mathematics, engineering and computer science, the field of geomorphometry has been revolutionized by the production of high-resolution, gridded topographic data, like those in triangulated irregular networks (TINs) and raster digital elevation models (DEMs) (Hengl and Evans, 2009; Hengl and MacMillan, 2009; Pike, 2000; Pike et al., 2009; Rasemann et al., 2004). Rapid advances in GISc along with growth in computing power, speed and memory, have promoted the increased the expansion of geomorphometry into the Earth sciences (Evans, 2012).

1.1 Landscape Evolution Models

Landscape evolution models try to emulate the processes that form ridgelines, valleys, and plains. On upper slopes of catchments, water currents are weak and dispersive, and hillslope processes dominate, forming convex-up profiles. On lower slopes, water flow merges and focuses, and river profiles become concave (Chen et al., 2014). Geomorphometry has been incorporated into the development and use of landscape evolution models and has increased our understanding of large-scale tectonic and earth-surface processes (Bishop, 2007; Codilean et al., 2006; Coulthard, 2001; Gerya et al., 2013; Goren et al., 2014; Pazzaglia, 2003; Refice et al., 2012; Temme et al., 2011; Tucker and Hancock, 2010). Landscape evolution models are used to study the complex spatio-temporal interactions among surface processes, tectonic forcing, and climatic conditions. These models now often include river basin's dynamic response to lateral erosion in the x and y dimensions, in addition to incision and deposition in the z dimension (Braun and Willett, 2013; Chen et al., 2014; Goren et al., 2014; Hancock et al., 2013; Tucker and Hancock, 2010; Willett et al., 2014; Wohl, 2014).

Dynamic aspects of river networks include channels that shift laterally or expand upstream, drainage divides that migrate across a region, and river-capture events whereby flow from one river is rerouted in a new direction and added to a new river basin (Willett et al., 2014). These processes result in a constantly changing 'map' of river networks over time and ultimately, networks that respond to perturbations in order to establish equilibrium between isostatic or tectonic uplift and river erosion (Braun et al., 2014).

Codilean et al. (2006), Tucker and Hancock (2010), and Chen et al. (2014) have reviewed existing models used to study long-term landscape evolution in the geosciences. Codilean et al.'s (2006) review addressed fundamental issues covered by each model, including the implementation of the various algorithms on numerical grids. A modeler should consider grid type (e.g., structured versus unstructured grids, such as DEMs versus TINs) and the grid resolution (e.g., cell size) when implementing a model algorithm. Each of these has considerable effect on model results (Codilean et al., 2006; Gerya et al., 2013; Kim et al., 2014).

The continuous topography of the domain in a landscape evolution model is approximated through digital terrain models in the form of regular or irregular grids (Codilean et al., 2006; Tucker and Hancock, 2010). Using *x*, *y*, and *z* dimensions, a raster DEM or TIN surface approximates topography exhibiting local minima (e.g., sinks, pits), local maxima (e.g., peaks), and surface specific elements, such as ridge lines, course lines (e.g., valleys, ravines), passes, breaklines, contours, slope lines, and plains within a DEM domain (Hengl and Evans, 2009). Regular grids include structured rectilinear meshes like those found in raster DEMs (Figure 1a), and irregular grids include irregular triangles or unstructured, Voronoi polygons (Figure 1b and c). Though grid choice affects the method used to solve governing equations and their results solved, most landscape evolution models still use either raster DEMs or TINs (Codilean et al., 2006; Hengl and Evans, 2009; Hengl and MacMillan, 2009).

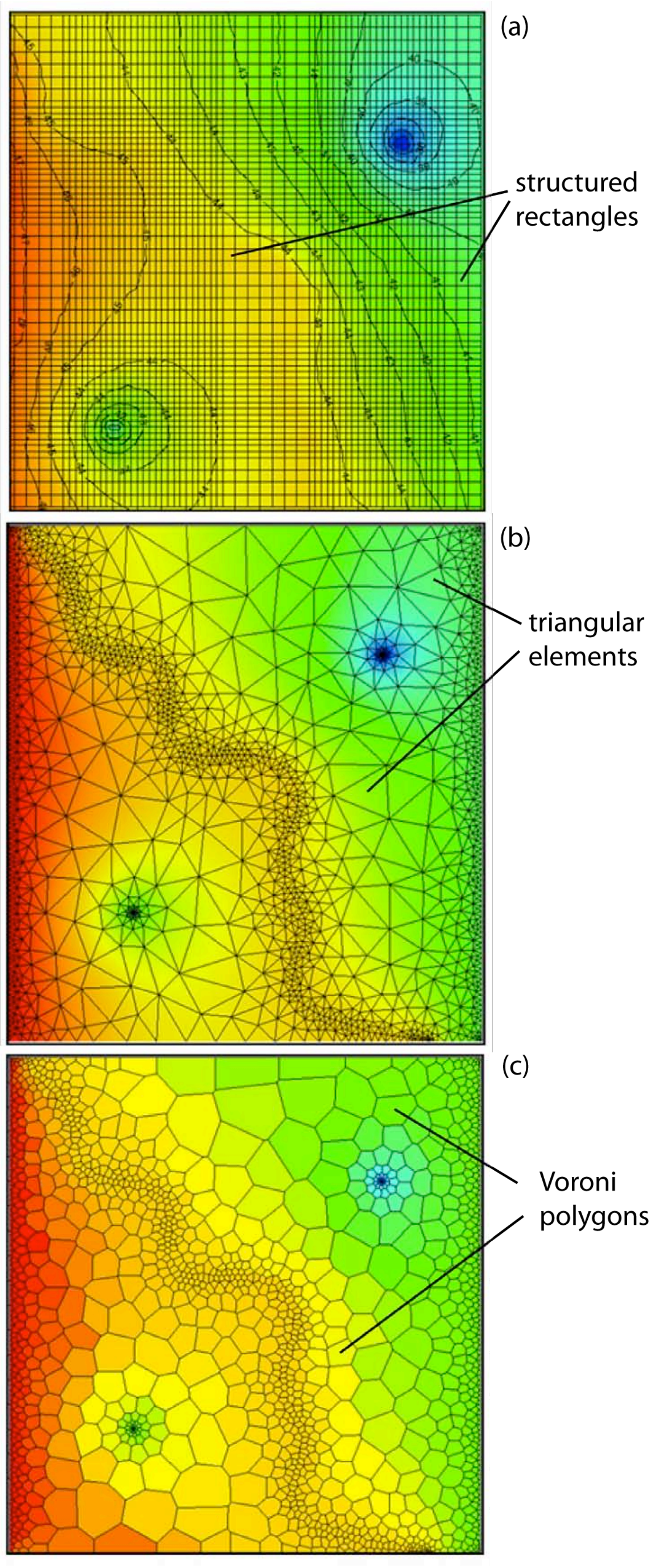

Figure 1. Schematic diagrams illustrating (a) a finite difference model discretized with a structured, rectilinear mesh; (b) a finite element model discretized with an irregular triangular network (TIN); and (c) a finite volume method discretized with irregular Voronoi polygons [modified from (Bogdon, 2013).

1.2 Numerical Models and Mesh Types

The computational modeling of any physical process includes the following steps:

- problem definition,
- mathematical model, and
- computer simulation.

Earth-surface geoscientists are primarily interested in defining problems that involve the interactions between climate (precipitation) and tectonics (uplift), and the results they have on topography over time. The translation of real physical processes into a mathematical representation of those processes lies in the capability of the geoscientist to distinguish and isolate relevant processes that operate within a system, while ignoring others, such that the model itself is relatively easy to understand, implement and interpret, yet still remains a valid representation of reality (Codilean et al., 2006; Peiró and Sherwin, 2005).

Mathematical modeling of a problem involves definition of the governing equations, such as Equation 1:

$$I = KA^{m}S^{n} \qquad \text{Eq. (1),}$$

where I is fluvial incision (a function of elevation, or height, with time), K is a dimensional coefficient of erosion, A is catchment area (directly related to channel discharge), S is channel gradient, and m and n are constants. This equation is the simplest, general form describing the rate of fluvial incision as a function of stream power, unit stream power, or basal shear stress (Codilean et al., 2006; Whipple and Tucker, 1999). It models how erosion in and by a river channel increases with increasing drainage area (e.g., precipitation and, thus, discharge) and increasing slope.

Governing equations, like Equation 1, 'idealize' the physical reality of the problem of interest, and in most cases, must be solved numerically, rather than analytically. Numerical models, such as the finite difference method (FDM), finite element method (FEM), and finite volume method (FVM) are used to determine solutions to the governing, partial differential equations in landscape evolution models (Tucker and Hancock, 2010). Before a model can be solved with one of the above methods, its domain must be discretized. Cell-based flow-routing algorithms, the foundation of landscape evolution models, are fundamentally linked to a spatial discretization scheme. Discretization, or the selection of grid type, is somewhat dependent on the numerical method used in a model. Most often, the FDM discretizes the domain into structured rectangles or squares, and the FEM discretizes into unstructured triangular elements. The FVM can use rectangles or triangles, but most often it uses unstructured Voronoi polygons (Bogdon, 2013).

The finite difference method uses structured rectilinear grids/meshes to solve the strong or differential form of the governing equations. In the FDM, functions are represented by their values at certain grid points and derivatives are approximated by local Taylor expansion through differences in these grid-point values. Raster DEMs are very suitable as initial (elevation) conditions in landscape evolution models that employ the finite difference method. Elevations in raster DEMs are stored in a uniform spatial structure with a single characteristic cell size, and a landscape's geometry is represented by a matrix of heights (z) for plan coordinates (x, y) in a given domain (Codilean et al., 2006; Hengl and Evans, 2009; Longley and Goodchild, 2005). Rectilinear grids are easy to understand, and have conservative solutions that are easy to calculate; however, the finite difference method and rectilinear meshes do have some disadvantages. Rectilinear grids cannot be efficiently refined around areas of interest, such as areas with steep topography or cliffs, or at model boundaries (Bogdon, 2013; Hengl and Evans, 2009; Peiró and Sherwin, 2005). Evenly spaced grids under-sample areas with more complex topography (e.g., very steep slopes, cliffs, and fault lines). Likewise, structured grids over-sample smooth or flat topography. Rectilinear mesh grids also typically require more computational overhead to keep track of the neighborhood of data around each cell and they make it more challenging to compute accurate gradients (slopes) during computations because data points often fail to fall on a regular grid (Kim et al., 2014).

Re-projection of a raster DEM can lead to a loss of accuracy, because the initial grid loses its regular structure depending on the new projection. Furthermore, distances between raster DEM cell centers in cardinal and diagonal directions have a negative impact on the precision of many hydrological models in which raster DEMs are used (Hengl and Evans, 2009; Longley and Goodchild, 2005). Use of an equal-area projection or, if the domain is small enough, a UTM projection helps minimize these effects.

The FEM and FVM use the integral form of governing equations and unstructured elements such as triangles and polygons to discretize model domains. The FEM and FVM are better suited than the FDM to deal with complex geometries in multi-dimensional problems, as integral formulations do not rely on any special mesh structure (Peiró and Sherwin, 2005). The FEM approximates solutions to differential equations with boundary conditions by using variational methods to minimize an error function and produce a stable solution. The FEM connects many simple element equations over many small subdomains in order to approximate the more complex differential equation over the larger domain of the entire problem (Peiró and Sherwin, 2005). Like the FDM and FEM, the FVM calculates values at discrete locations on a mesh. The mesh can be either structured or unstructured. The finite volume refers to the small volume around each node point (Figure 1). Volume integrals are conservative and evaluated as fluxes (Peiró and Sherwin, 2005). This numerical method is gaining traction in its application, particularly in the field of fluid dynamics (Bogdon, 2013), but landscape evolution models still tend to use either FDM or FEM.

Unstructured TIN meshes, used in FEM landscape evolution models, have the advantage that they are easily generated and tailored to the specific topography of areas of interest. Most importantly, the TIN structure varies the density of sampled points, and therefore the size of triangles, so they can be adjusted to reflect the relief of the surface being modeled. Typically, more points with smaller spacing are used in areas of higher relief or rougher surfaces. TINs also use larger spacing where relief if more subdued or smoother. TINs more accurately depict steep cliffs, fault lines, and other discrete and/or abrupt changes in elevation, using the same number of points as mesh grids (Hengl and Evans, 2009; Kim et al., 2014; Longley and Goodchild, 2005). The vector-based TIN structure represents a land surface as contiguous non-overlapping triangular elements with apices at given points. Following Delaunay's criterion, triangles are positioned so that they are closest to those with angles of similar values (Deren and Xiao-Yong, 1991; Okabe and Yamada, 2001; Peuquet, 1984). Though based on point raster DEMs with *x*, *y*, and *z* coordinates, TINs instead store data in a topological, vector data structure that manages information about the nodes comprising each triangle and the neighbors of each triangle (Hengl and Evans, 2009; Longley and Goodchild, 2005).

A second major advantage of irregular meshes is that they are self-adapting within a landscape evolution model (Codilean et al., 2006; Tucker et al., 2001). The resolution of the mesh automatically varies anywhere on the landscape model as a function of the model's surface-process rates at that locality. Thus, where rates of landscape evolution (e.g., erosion) are high, such as on steep hillslopes or stream knick-points, the TIN mesh resolution becomes finer so as to capture increased detail of the topography at that locality. Conversely, at locations where rates of change are low, the mesh resolution adapts to a coarser mesh. This is computationally more efficient than running the whole model with a high-resolution domain, represented by a raster DEM, which would be necessary to accurately characterize the localities.

The disadvantage that accompanies this adaptability is that irregular meshes have a much more complex data structure, and therefore require more complex algorithms and more computational storage space; if not configured properly, landscape evolution models using self-adapting TIN meshes can be computationally more intensive models than using raster DEMs (Codilean et al., 2006). The mesh type used in a numerical model affects the computational demands of the model, as well as the accuracy of its results. Although the vector TINs versus raster DEMs debate is still unresolved, in most applications, raster DEMs are used as a standard (Gerya et al., 2013; Hengl and Evans, 2009; Kim et al., 2014).

Realistically, geoscientists do not write their own algorithms each time they wish to study the geodynamics of a region. Most often, a geoscientist chooses from readily available software that has been developed around a specific numerical method, and thus specific mesh type. Selection of which landscape model to use is based not only on the specific question being posed, but on the accuracy, if not popularity, of the model in a geoscientist's field of research. It is rare that a geoscientist chooses which of the above numerical methods or mesh type is used in a landscape evolution model (Bogdon, 2013), unless they write a new model algorithm.

1.3 Mesh Resolution

Though geoscientists may be limited in their choice of numerical technique and/or mesh type, they have more options when it comes to the mesh resolution they employ in their models. Cost and coverage/extent of DEMs are usually the first, and often limiting, factors to consider in the selection process, and they are often the limiting factors. Fortunately, NOAA NCEI (National Oceanic and Atmospheric Administration, National Centers for Environmental Information [formally known as the National Geophysical Data Center]), USGS EROS (United States Geological Survey, Earth Resources Observation and Science Center), and NASA (the *National Aeronautics and Space Administration*) in cooperation with both the

National Geospatial-Intelligence Agency (NGA) and The Ministry of Economy, Trade, and Industry of Japan (METI) offer free, global or near-global coverage DEMs with cell sizes ranging from 30 m to 9.3 km. Freely available, finer resolution DEMs (3-m to 30-m cell sizes) are available for the contiguous United States land topography and for selected areas in Alaska through the USGS National Elevation Dataset (NED) (Farr et al., 2007; METI NASA, 2012; NOAA NCEI, 2015; USGS, 2015; USGS EROS, 2012). Finer resolution DEMs, including those created through LiDAR surveys are often available, but for limited areas and often at cost.

Terrain analysis, particularly distinguishing valleys from hillslopes, is a fundamental step in landscape evolution models (Braun and Willett, 2013; Goren et al., 2014; Pelletier, 2013; Willett et al., 2014). Drainage network extraction methods often rely on contributing area or length and user-defined thresholds that define the transition from hillslope to valley floors in DEMs (Braun and Willett, 2013; Giannoni et al., 2005; Goren et al., 2014; Hancock and Evans, 2006; Montgomery and Dietrich, 1992; O'Callaghan and Mark, 1984; Pelletier, 2013; Tarolli and Dalla Fontana, 2009; Tribe, 1991, 1992; Willett et al., 2014). Hillslope-to-valley transitions become more obvious as DEM grid size decreases due to the better representation of hillslope morphology (Tarolli and Dalla Fontana, 2009). According to Montgomery and Foufoula-Georgiou (1993), even moderately steep topography requires at maximum a 30-m DEM resolution to accurately depict the hillslope-valley transition. Though finer-resolution DEMs may capture topography more realistically than coarser-resolution DEMS, it is important that geoscientists also consider computer resources when selecting a DEM (mesh) resolution. Finer-resolution DEMs require more computing resources than coarser resolutions, when being used in landscape evolution models. DEMs that are most commonly used in landscape evolution models are the 90-m SRTM (Shuttle Radar Topography Mission) and 30-m ASTER (Advanced Spaceborne Thermal Emission and Reflection Radiometer) images.

1.4 Motivation for this Thesis

Various surface processes act on and shape the Earth's surface on a wide range of temporal and spatial scales. These processes include fluvial and glacial incision, transport and deposition, aeolian processes, hillslope processes and karst formation. Rates of landscape evolution are primarily established by the efficiency of river incision in a region, particularly in tectonically active areas with relatively large mean slopes. In such environments, channel incision generates slopes, which destabilize over time, and causes mass movement by gravity-driven processes. The sediment resulting from these gravity-driven processes is then deposited in a river channel, where flowing water acts as the main transport agent toward lower elevations (Whipple, 2004; Whipple and Tucker, 1999). Most landscape evolution studies have mainly studied the balance of erosion and incision in the negative vertical dimension ($-z$) and uplift/exhumation in the positive vertical dimension ($+z$) (Chen et al., 2014; Codilean et al., 2006; Whipple, 2004; Wohl, 2014). When these processes are in balance with one another, a landscape is said to be in dynamic equilibrium (Braun et al., 2014; Bull, 1991; Gilbert, 1877; Hack, 1975; Sklar and Dietrich, 1998; Whipple, 2004; Whipple and Tucker, 1999).

Earth-surface scientists have long searched for a metric that distinguishes the tectonic signal from the climate signal in topography, whether it is in equilibrium or not. Recently, Willett et al., (2014) published a paper introducing chi (χ), a quantitative proxy for steady-state river channel elevation derived from a landscape evolution model. In their paper, Willett et al. (2014) use chi to produce present-day snapshots of the dynamic state of river basins in China, Taiwan, and the southeastern United States, and to evaluate whether or not these regions are in dynamic equilibrium.

Though the Willett et al. (2014) study convincingly shows where regions or select areas of regions are in equilibrium, the study did not specify whether absolute chi values can be used to quantify states of equilibrium between different regions, or if driving forces of erosion – precipitation and tectonism – can be distinguished. This thesis aims to investigate whether absolute chi values can be used to characterize the state of equilibrium for regions with vastly different present-day tectonic and climate settings.

CHAPTER 2: Aims and Objectives

FastScape is one of several landscape evolution models that computes the dynamic response of river basins to the presence or absence of isosatic/tectonic forcing and varying climatic conditions (Braun and Willett, 2013). It is also the numerical model that is the basis for the calculation of chi in Willett et al. (2014). In this study, chi results are calculated for (1) a region in the desert climate and passive continental margin of Namibia, and (2) a region in the central Himalaya, where active mountain building and a wet, monsoonal climate dominate.

Willett et al. (2014) have already investigated the sensitivity chi to various concavity (*m/n*) parameters and earth-surface parameters, in addition to uplift and precipitation rates. This thesis mainly focuses on domain size (e.g., number of cells and surface area within a domain) and grid resolution (e.g., 90-m SRTM vs. 30-m ASTER), and how they affect resultant FastScape chi values in the Namibia and Himalaya study areas.

An obvious parameter that is missing from the list above is mesh type (e.g., raster DEM versus TIN surface). Willett et al. (2014) use a combination of the FastScape (Braun and Willett, 2013) and Divide-and-Capture (DAC; Goren et al., 2014) algorithms to calculate present-day chi values for their study areas. The numerical component of the Divide and Capture (DAC) landscape evolution model used in Goren et al. (2014), and subsequently in Willett et al. (2014), is based on the FastScape model and equations, but DAC uses a TIN and Delaunay triangulation to represent topography during execution of the FastScape algorithm. Braun and Willett (2013) note that the FastScape algorithm does not depend on the position of the nodes used to describe the landscape and that nodes can be positioned at the corners of a regular rectangular mesh or not. A user-friendly version of the DAC code, however, is not yet readily available (L. Goren, pers. comm., 2014), whereas the code for mesh-grid based FastScape is provided upon request (Braun, 2013). Chi-value calculations were added to the FastScape algorithm in August 2014 (J. Braun, pers. comm., 2014), and are based on the chi (χ) equations derived by Willett et al. (2014). As presently coded, FastScape uses raster DEMs as topographic input.

In addition to the sensitivity of chi to model domain parameters, this thesis also investigates the extent to which chi is sensitive to the actual rate at which landscapes are changing. Namibian and central Himalayan landscapes are eroding at widely different rates (e.g., 10^1

m/Ma and 10^3 m/Ma, respectively). Comparison of their chi values tests how useful the new chi-value metric is (Willet et al., 2014) by evaluating whether chi simply acts as (a) an 'on/off' metric for dynamic equilibrium, or (b) a metric that indicates ‘degrees’ of landscape evolution.

Three possible outcomes will be explored:

- **Namibia and the central Himalaya are each in dynamic equilibrium:** χ-values will be very similar (essentially the same) for (a) both regions, and (b) throughout the drainage networks in each region.
- **Namibia or the central Himalaya is in dynamic equilibrium**, the other is not: χ-values will be the same throughout the drainage networks in the equilibrated region. The region in disequilibrium will exhibit χ-values that vary significantly within its drainage, and that are significantly different from χ-values in the equilibrated region.
- **Neither Namibia nor the central Himalaya is in dynamic equilibrium**: χ-values will vary significantly (a) throughout the drainage networks in each region, and (b) vary significantly between regions due to the different tectonic settings (active vs. passive).

Relationships between published, basin-wide cosmogenic ^{10}Be erosion rates and chi values are also explored for specific basins in Namibia and central Himalaya river catchments to determine if there is any correlation between erosion rates and chi values. Because basins with lower chi values will migrate and increase their drainage area at the expense of basins with higher chi values (Willett et al., 2014), it is hypothesized that basins in disequilibrium with higher cosmogenic ^{10}Be erosion rates will have lower average chi values in a setting where erosion is dominated by precipitation. In a setting where uplift is the dominant driving force, a positive relationship between chi values and ^{10}Be erosion rates is expected for basins in disequilibrium, because chi is directly related to increases or decreases in elevation (Figure 2). Basins that are in equilibrium are expected to have constant chi with increasing ^{10}Be erosion rates.

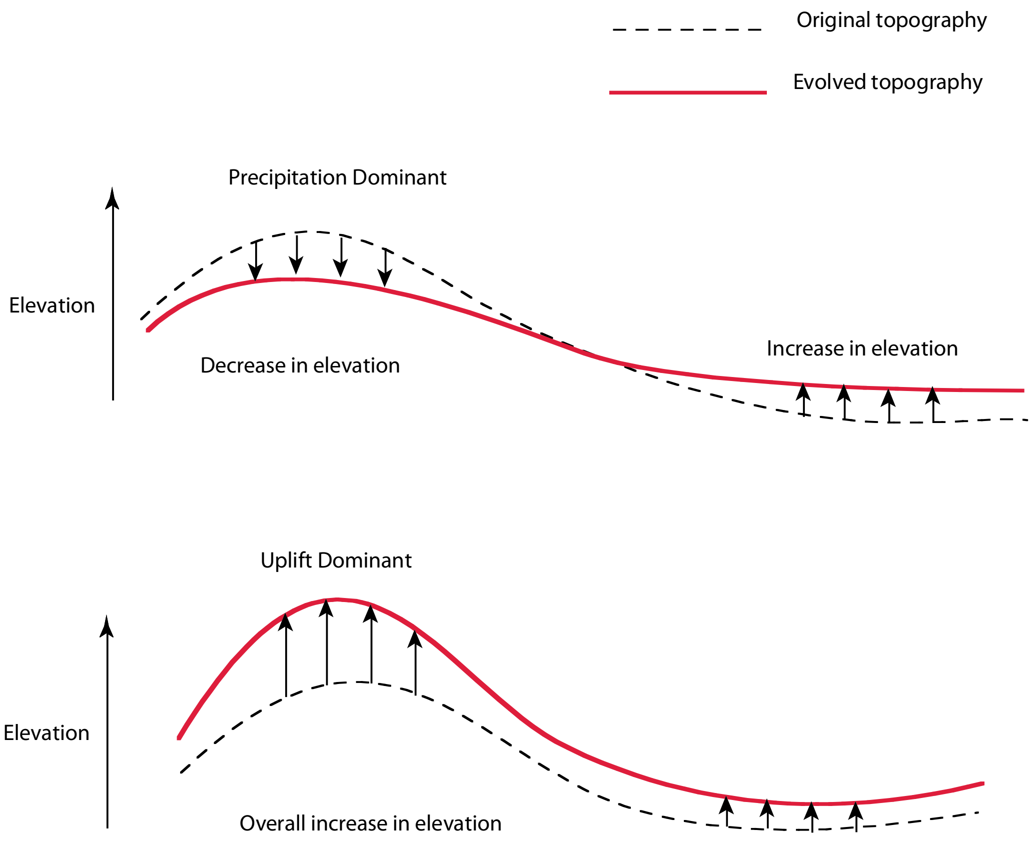

Figure 2. Schematic diagram of landscape erosion in precipitation- and uplift-dominant settings.

CHAPTER 3: Background and Literature Review

Landscape evolution is commonly studied from the perspective that river-channel incision controls topography. Migrating drainage divides in and between catchments drive the evolution of river networks in the vertical and horizontal directions over time. The actual state of a landscape may be transient in nature and may reflect the effects of erosive and transport processes that occur on different time scales (Chen et al., 2014).

Through the use of complex mathematical expressions of fluxes (e.g., geomorphic transport laws), landscape evolution models, and newer geochronologic methods (e.g., cosmogenic dating), geoscientists can quantify surface-process rates and sequential topographic changes through time (Wohl, 2014). Quantification of processes and rates highlights the large-scale, long-term links among climate, tectonics, and erosion and the role of rivers in landscape evolution.

3.1 FastScape

FastScape is a landscape evolution model, which uses the stream-power law, a regular, rectangular mesh, and the single-flow-direction approximation of O'Callaghan and Mark (1984) to calculate discharge (ϕ) as a function of time and space. Almost all landscape evolution models route water and sediment down the path of the steepest slope (Figure 3) using this method or an adaptation of it (Codilean et al., 2006). In the process of calculating elevation and chi values as the landscape evolves, land-surface characteristics (e.g., elevation and slope) are determined by FastScape in order to accurately route flow (Braun and Willett, 2013; Goren et al., 2014; Willett et al., 2014). FastScape performs a watershed analysis to determine catchment areas and stream networks; it extracts hydraulic attributes of base level, flow directions, flow paths, and accumulated flow (upstream drainage area) from a specified DEM.

FastScape calculates new elevations for each cell in a model domain as it evolves the landscape over time. To make it easier to visualize the FastScape model, animations have been created to show topographic evolution over 50 Ma of model time for two small domains in Namibia and the central Himalaya (Animations 1 to 4; found at cassandrafenton.blogspot.de). Namibia experiences much lower precipitation and uplift rates than does the central Himalaya, and erosion in Namibia occurs on a much smaller scale. This difference is clear, particularly when comparing Animations 2 and 4, which show a fairly stable Namibian landscape, in contrast to a rapidly uplifted and subsequently, heavily eroded central Himalaya. Notice in Animation 4 that headward erosion of rivers into the highlands is driving the overall lowering of the topographic surface.

Once elevations are calculated, FastScape computes chi based on the resultant topography and drainage network (Braun, 2013; Braun and Willett, 2013). Chi values are based on the geometry and dynamic state of a river network at any given time step in the model (Willet et al., 2014).

In 2013, Braun and Willett presented the new FastScape algorithm. It solves the basic stream-power equation, which governs channel incision and landscape evolution, through a network of nodes in x and z space. The rate of channel incision ($\partial z/\partial t$) is directly proportional to the hydraulic shear stress (τ) exerted by a river onto a channel bed

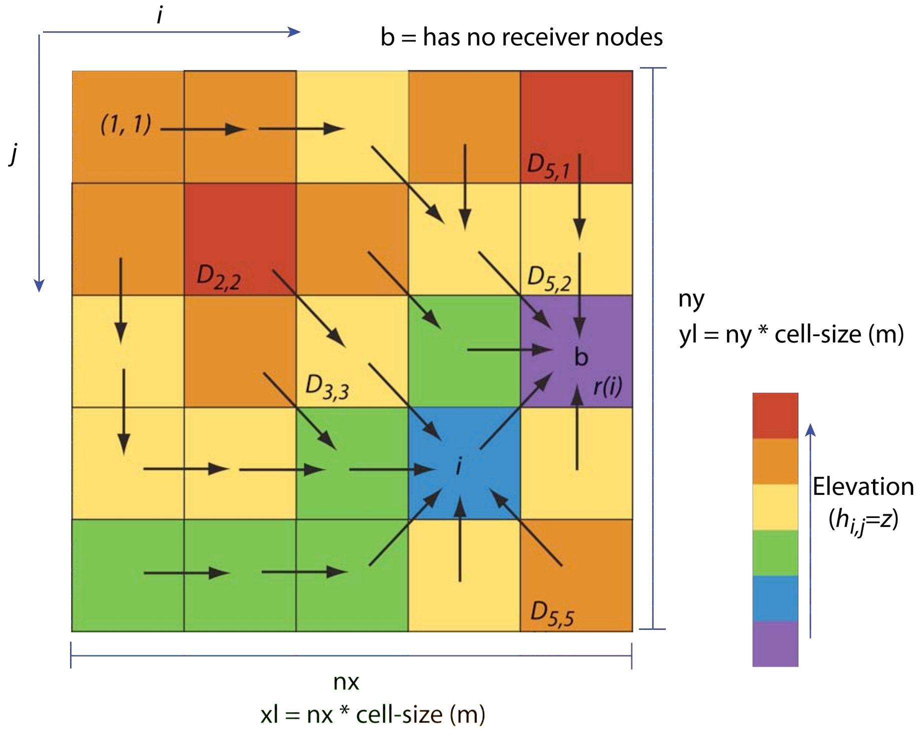

Figure 3. Schematic diagram of a DEM showing relative heights ($h_{i,j}$) for each pixel and the direction of water flow (black arrows) along steepest slopes. FastScape creates a regular finite-difference grid from this file where each pixel represents a node ($n_{i,j}$) with height ($h_{i,j}$). The total number of grid points (n_p) is determined by nx and ny, which are the number of cells in the east-west and north-south directions. In this diagram nx and ny are both 5. In the cases of Namibia 4101 and Himalaya 4101 nx and ny are both 4101.

$$\tau = k\phi^{p}S^{n} \qquad \text{Eq. (2)}$$

where ϕ is either total discharge or discharge per unit channel width, S is local slope, and k is a constant (Whipple and Tucker, 1999). It follows that overall change in incision will be the difference between uplift (U) and erosion of the channel bed:

$$\frac{\partial z}{\partial t} = U - KA^{m}S^{n} \qquad \text{Eq. (3)}$$

where z is elevation, A is the contributing drainage area and K is a factor that varies based on lithology, mean annual precipitation of a region, channel width, flood frequency and channel hydraulics, and m and n are positive empirical constants (Whipple and Tucker, 1999). Because parameters total discharge *(ϕ)* and A are related, ϕ can be substituted for A in Equation 3, resulting in the following equation (Braun and Willett, 2013):

$$\frac{\partial z}{\partial t} = U - K_{f}\phi^{m}S^{n} \qquad \text{Eq. (4)}$$

where ϕ is the product of drainage area (A) and precipitation rate or, in the case of spatially variable precipitation, the surface integral of the precipitation rate over the drainage area A (Braun, 2013; Braun and Willett, 2013).

Slope is the first-order derivative of elevation (z), thus, Equation 4 is actually a nonlinear transport/advection equation with a spatially variable transport velocity that can be rewritten as follows (Braun and Willett, 2013; Willett et al., 2014):

$$\frac{\partial z}{\partial t} = U - K_{f}\phi^{m}\left(\frac{\partial z}{\partial x}\right)^{n} \qquad \text{Eq. (5).}$$

This type of equation is very difficult to solve numerically because the solution typically requires small time increments and/or complex finite difference schemes to assure stability and accuracy (Braun and Willett, 2013; Tucker and Hancock, 2010).

Braun and Willett (2013) presented a new algorithm, which computes discharge (ϕ) that is an $O(n_p)$ rather than $O(n_p^2)$ computational problem and is adapted to parallel computing architecture; the number of operations needed to determine a solution varies as n_p rather than n_p^2, where n_p is the number of grid points in the model domain. It can thus be used to solve Equation 5 on grids containing 10^8 nodes on a laptop computer and, potentially, up to 10^{10}

nodes on a large multi-processor computer (Braun and Willett, 2013). Furthermore, Braun and Willett (2013) incorporate a more stable and more accurate implicit method to integrate Equation 5. This guarantees that much larger time steps can be used, further increasing the overall computational efficiency of the method. Computation time increases linearly with the number of points used to discretize the landscape of interest. The model uses an implicit scheme for the time integration of Equation 5, and is thus unconditionally stable; accuracy of the model is not lost at the expense of using large time steps (Braun and Willett, 2013).

Willett et al. (2014) also use the stream-power incision law in their chi model; however, they present the equation as a function of drainage area (*A*) rather than discharge (ϕ):

$$\frac{\partial z}{\partial t} = U - K_f A^m \left(\frac{\partial z}{\partial x} \right)^n \qquad \text{Eq. (6).}$$

When uplift and erosion are spatially and temporally constant, the steady-state solution of Eq. 6 becomes the following:

$$z(x) = z_b + \left(\frac{U}{KA_0} \right)^{\frac{1}{n}} \chi \qquad \text{Eq. (7)}$$

where z_b is the river network's base-level elevation at $x = x_b$. The chi value (χ) is an integral function of position *x* in the channel network, such that:

$$\chi = \int_{x_b}^{x} \left(\frac{A_0}{A(x')} \right)^{\frac{m}{n}} dx' \qquad \text{Eq. (8)}$$

where A_0 is an arbitrary scaling area and the integration is performed upstream from base level (x_b) to position *x*. If uplift or erosion varies in space and/or time, and these variations are known, the solution for elevation (*z*) and for chi (χ) can still be obtained through equations 7 and 8 (Willett et al., 2014).

3.1.1 FastScape's Finite Difference Method

In FastScape, the landscape of interest is represented as a series of nodes (n_p) with elevations (*h*) in *x*-*y* space and n_b of the nodes fixed at base level (Figure 3). When a raster DEM is used to define initial topography, FastScape assigns starting elevations ($h_{i,j}$) to each node with *x*-*y* coordinates. To execute the FastScape algorithm, it is first necessary to create an array of nodes (Figure 4) that represent the flow path of water to base level, and then to determine how those nodes are ordered (Figure 5), such that discharge can be calculated by progressively adding the contribution of each node to the total stream discharge or its contributing area to the total drainage area (Braun and Willett, 2013). The calculation of chi (χ) is subsequent to the calculation of discharge or drainage area, based on the relationships of these variables as described in the equations above.

FastScape computes neighbors for each node, and determines which neighbor node defines the steepest descent/slope. This neighbor node is called the receiver node of node i and is noted $r(i)$ (Figure 3 and Figure 4). Each node has a single receiver, except base-level nodes (b_i), which have none. Local minima in the landscape correspond to nodes that are their own receiver ($r(i) = i$). Nodes that contribute discharge or area to node i are called donor nodes ($D_{i,j}$) (Figure 3) for $j=1,\cdots,d_i$ where d_i is the number of nodes having i as a receiver and thus $r(Di,j)=i$. The number of donor nodes to node i is limited by the number of neighbors to node i. A rectangular grid makes it simple to compute the list of neighbors ($N_{i,j}$, for $j=1,\cdots,n_i$), where n_i is the number of neighbors connected to i (Braun and Willett, 2013; O'Callaghan and Mark, 1984).

Once the stack of receiver node information $r(i)$ for each node i is calculated, the stack is inverted (Figure 5) into a list of donor nodes (e.g., a donor array $D_{i,j}$). An array (d_i) of the number of donors per node is also built for each node i. This information is stored in a single dimension array D_i and an index array δ_i. Each node has only one receiver and thus can only be in one donor array and only appear once in that array. This ensures that the list of donor nodes can be stored in an array of length n_p (Braun and Willett, 2013).

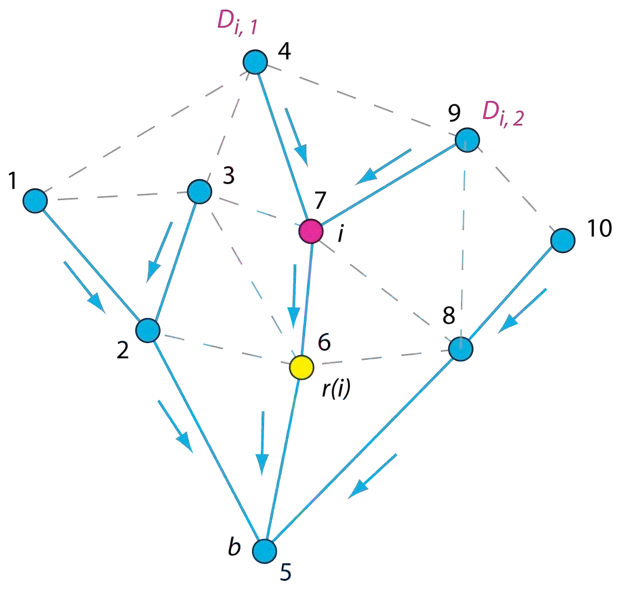

Figure 4. Nodal representation of the flow path of water for an arbitrary landscape (modified from (Braun and Willett, 2013). Nodes (circles) are connected by solid and dashed lines. Solid blue lines indicate the connections between nodes that follow the steepest descent. Blue arrows indicate the direction of water flow. Dashed lines represent the connections between nodes, but which are not used to construct the flow-path network. Node b represents base level. The yellow node r(i) is the receiver node from node I (magenta circle). Nodes $D_{i,1}$ and $D_{i,2}$ form the list of donor nodes to node i. Numbers in the figure are in an arbitrary order. Ordering of the nodes for FastScape calculations are shown in Figure 5.

To create the donor array $D(i,j)$ for node i, d_i is initialized to zero for $i = 1,\ldots,n_p$ and the receiver information for node i is used (Figure 3), where:

$$d_{r(i)} = d_{r(i)} + 1 \qquad \text{for } i = 1,\ldots,n_p \qquad \text{Eq. (9).}$$

The list of donors for all nodes is stored in an array of dimension n. The array d_i is then transformed into an index array δ_i, which contains the location of the donor array for node i in an array of dimension n, such that:

$$\delta_{n_p+1} = n_p + 1 \qquad \text{Eq. (10)}$$

$$\delta_i = \delta_{i+1} - d_i \qquad \text{for } i = n_p,\ldots,1,\text{-}1 \qquad \text{Eq. (11).}$$

The donor array for node i is built according to:

$$D\left(\delta_{r(i)} + w_{r(i)}\right) = i \qquad \text{for } i = 1,\ldots,n_p \qquad \text{Eq. (12)}$$

and

$$w_{r(i)} = w_{r(i)} + 1 \qquad \text{for } i = 1,\ldots,n_p \qquad \text{Eq. (13)}$$

where w_i is an integer working array initialized to zero and vector (D) of length n_p, contains the donor information $D_{i,j}$:

$$D_{i,j} = D(\delta_i + j - 1) \qquad \text{for } j = 1,\ldots,\delta_{i+1} - \delta_i \qquad \text{Eq. (14).}$$

FastScape then creates a vector stack $s(i)$ that contains the list of nodes from 1 to n_p and in the specific node order (Figure 5) that FastScape uses to perform computation of discharge (ϕ) and to solve the governing landscape evolution equation (Equation 5).

The FastScape algorithm begins its discharge computations at nodes that have no donors, such that the inverted stack starts at the top of a catchment and proceeds downhill following the receiver-node information, which define the water flow path (Figure 5). Thus, FastScape calculates the contribution of each node to the discharge (or drainage area), ending with the total discharge (or drainage area) at node *i*. At confluences, the inverted stack jumps to the top of the subcatchment of each of the tributaries where FastScape systematically and progressively computes the contribution to discharge from these subcatchments before proceeding to the next node *i*, beyond the confluence (Braun and Willett, 2013).

Using the inverted stack, the computation of the discharge or drainage area is based on the following equations:

$$\phi(i) = a(i)\nu(i) \qquad \text{for } i = 1,\ldots,n_p \qquad \text{Eq. (15)}$$

$$\phi(r(s(i))) = \phi(r(s(i))) + \phi(s(i)) \qquad \text{for } i = n_p,\ldots,1,-1 \qquad \text{Eq. (16)}$$

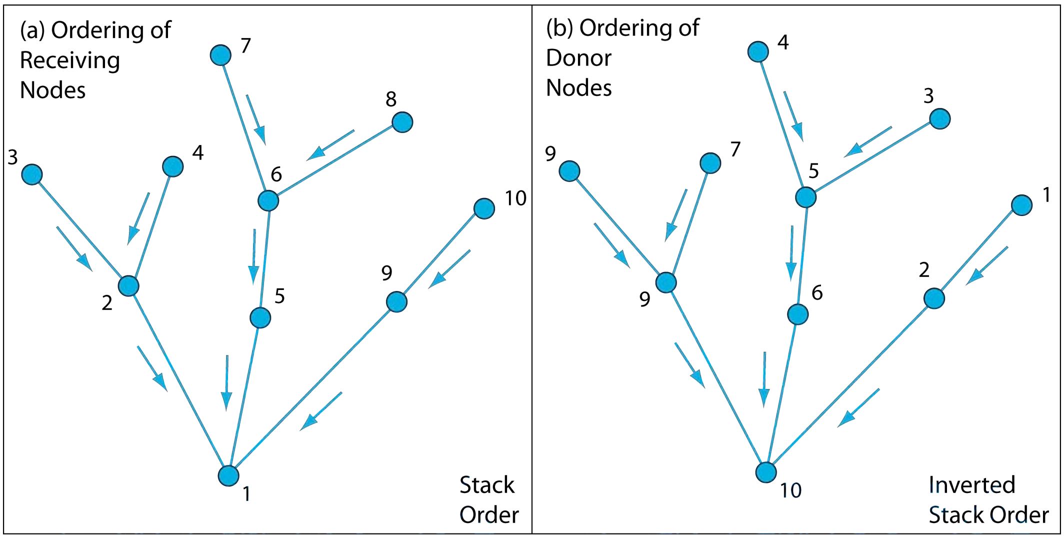

Stack ($s(i)$) node i	for
1	$i = 1$
2	
3	
4	
5	
6	
7	
8	
9	
10	$i = n_p$

Inverted Stack ($s(i)$) node i	for
10	$i = n_p$
9	
8	
7	
6	
5	
4	
3	
2	
1	$i = 1$

Figure 5. Schematic diagram of node order in the stack and the inverted stack (modified from (Braun and Willett, 2013). Blue arrows indicate the flow path of water in the downhill direction. (a) Stack nodes are ordered from the receiving nodes at base level (e.g., node 1) to the upstream nodes, where it is noted which nodes receive from other nodes (i.e., Node 1 is the receiving node for Nodes 2, 5, and 9). (b) After the stack has been inverted, the resulting order starts with donor nodes at the tops of catchments (e.g., Nodes 1, 3, 4, 7, and 9). All upstream nodes are processed before computations 'move downstream.'

where *ϕ(i)* is the discharge at node *i*, *v(i)* is the net precipitation rate over the catchment area *a(i)* upstream of node *i*. The precipitation rate *v(i)* can vary spatially within a region (Braun and Willett, 2013), but in the case of uniform precipitation, the following equation holds true:

$$A(i) = a(i) \quad \text{for } i = 1,\ldots,n_p \qquad \text{Eq. (17)}$$

$$A(r(s(i))) = A(r(s(i))) + A(s(i)) \quad \text{for } i = n_p,\ldots,1,\text{-}1 \qquad \text{Eq. (18).}$$

Note that in the case of a rectangular mesh, such as that used in this study, $a(i) = \Delta x \times \Delta y$ for all *i* and the drainage area can be computed by integer summation (Braun and Willett, 2013).

$$q_s(i) = a(i)\phi\frac{\partial h(i)}{\partial t} \quad \text{for } i = 1,\ldots,n_p \qquad \text{Eq. (19)}$$

$$q_s(r(s(i))) = q_s(r(s(i))) + q_s(s(i)) \quad \text{for } i = n_p,\ldots,1,\text{-}1 \qquad \text{Eq. (20).}$$

(Braun and Willett, 2013) then use a simple first-order finite difference scheme to compute both the spatial derivative (the slope) of the height field (Equation 21) and its time derivative (the rate of change of landscape height; Equation 22):

$$\frac{\partial h(i)}{\partial x} = \frac{h(i) - h(r(i))}{\Delta x_i} \qquad \text{Eq. (21)}$$

$$\frac{\partial h(i)}{\partial t} = \frac{h^{t+\Delta t}(i) - h^t(i)}{\Delta t} \qquad \text{Eq. (22)}$$

where Δx_i is the distance between node *i* and its receiver *r(i)*, and Δt is the time step in the algorithm. The right-hand sides of Equations 21 and 22 are substituted into Equation 5, such that

$$\frac{h^{t+\Delta t}(i) - h^t(i)}{\Delta t} = -KA^m\left(\frac{h^t(i) - h^t(r(i))}{\Delta x_i}\right)^n \qquad \text{Eq. (23),}$$

which is the explicit first-order finite-difference scheme to solve the stream-power equation (Equation 5). The right-hand term of the equation (and thus the slope) is computed at time *t*. The implicit form of the finite difference method, as used by FastScape, where the right-hand side term is computed at time $t+\Delta t$ is as follows:

$$\frac{h^{t+\Delta t}(i) - h^{t}(i)}{\Delta t} = -KA^{m}\left(\frac{h^{t+\Delta t}(i) - h^{t+\Delta t}(r(i))}{\Delta x_{i}}\right)^{n} \qquad \text{Eq. (24).}$$

Equation 24 ensures much greater stability and allows much larger time steps Δt (Braun and Willett, 2013).

3.2 Understanding Chi (χ)

River networks shape landscapes into ridges and valleys as rivers incise through bedrock. Within a river catchment, basin geometries are created by the configuration of these valleys and ridges, where an area of land is bounded by ridgelines acting as drainage divides. Surface water collects in basin headwaters and flow downstream to a single point of lower elevation along a stream or river channel. Channel geometry, channel slope, and network topology adjust towards a balance between tectonic or isostatic uplift and erosion. Climatic conditions, such as temperature and precipitation, and the erodibility of the rock type(s) in a region play a major role in this dynamic river-network reorganization (Braun and Willett, 2013; Goren et al., 2014; Willett et al., 2014; Yanites and Kesler, 2015).

Most studies of river systems tend to focus on the balance of uplift and erosion in the vertical direction (*z*) within existing river channels, and they assume that the map-view of basin geometry remains more or less fixed in time (Kirby and Whipple, 2012; Pritchard et al., 2009; Willett et al., 2014). Willett et al. (2014) integrate the view that drainage divides are mobile and they migrate accordingly across landscapes in the *x*- and *y*- directions as they adjust towards equilibrium elevations and positions. Furthermore, Willet et al. (2014) suggest that a landscape that is in equilibrium will have stationary drainage divides. Chi, as defined by Equation 8, is the quantitative proxy introduced by Willett et al. (2014) that helps visualize equilibrium and disequilibrium in a drainage network and allows for prediction of ridgeline migration.

Chi is limited to the analysis of river channels (Willett et al., 2014), and its values are calculated at each point in a stream moving from base level to headwaters. Chi values are lowest at base level and highest in headwaters for any given catchment (Figure 6). In order for a river network to be in geometric equilibrium in map view, chi values on either side of drainage divides throughout the network must have equal values. Conversely, maps showing different chi values on either side of divides indicate a river network that is in disequilibrium.

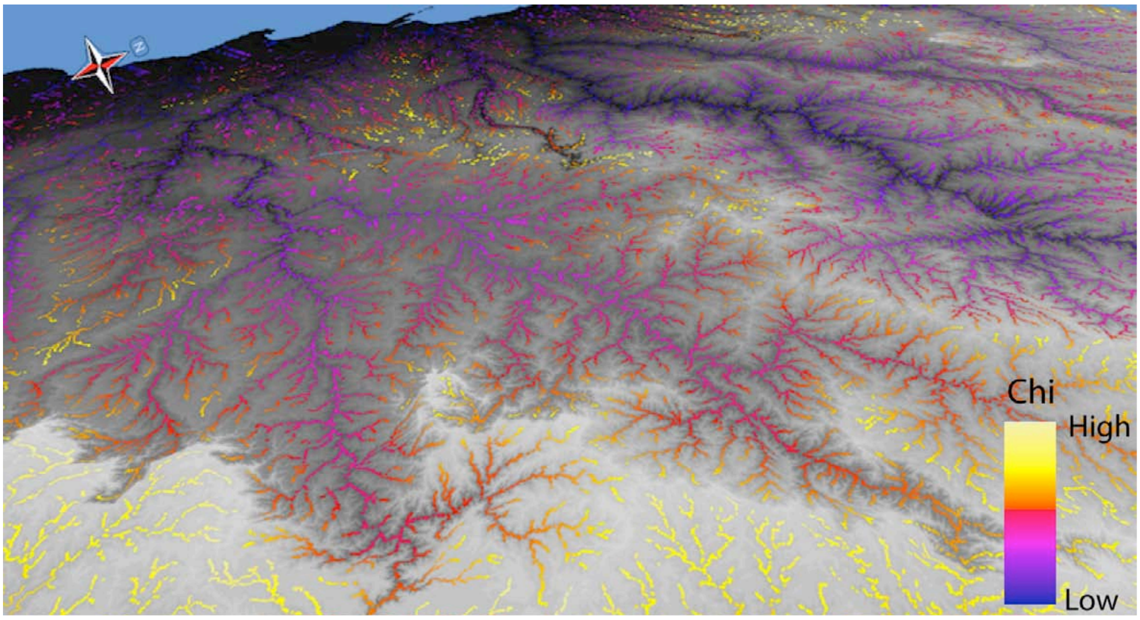

Figure 6. Oblique 3D ArcGlobe view of chi values for drainage networks in the Namibia 4101 domain as calculated by FastScape at the 25 Ma time step. The blue region in the upper left-hand corner represents the Atlantic Ocean and base level in this model. Notice that chi values are lowest (blue) near base level and then increase moving upstream towards the Great Escarpment in the bottom of the image.

Basins with lower chi values will migrate and increase their area at the expense of basins with higher chi values (Willet et al., 2014).

Where two stream-flow paths originate at a common drainage divide and end at a common base level, their steady-state elevation profiles may differ depending on the topologic and geometric structure of the river network. Notice the lower and higher chi values along the shared drainage divide of Basins I and II, respectively, in Figures 7 and 8. The steady-state elevation (chi) of the channel head in Basin II is higher than that of the channel in Basin I; the divide is not stable. The river network will adjust itself laterally and vertically until the difference in steady-state elevations of the channel heads is zero, at which point, equilibrium will have been achieved (Willett et al., 2014). In effect, Basin I will erode into the headwall slopes, forcing the ridgeline to migrate towards Basin II. This, in turn, causes the overall lowering of the ridgeline elevation.

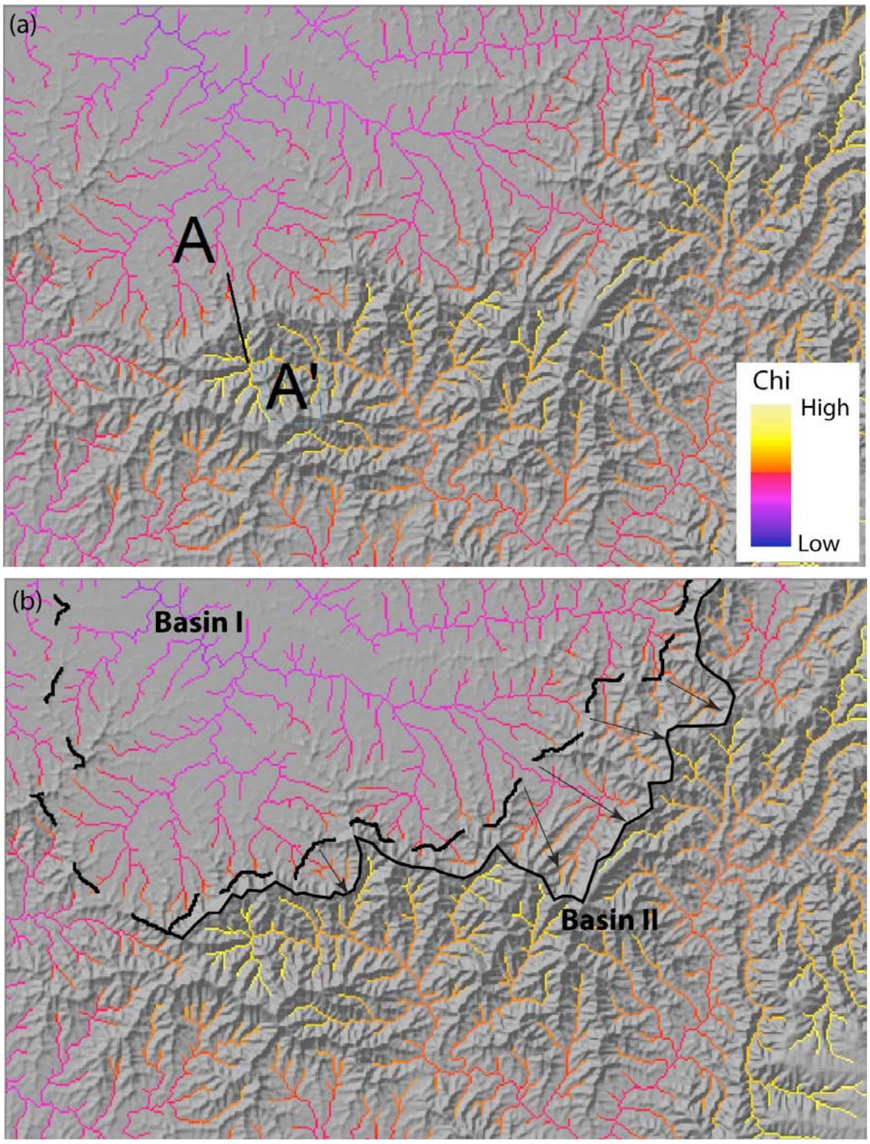

Figure 7. Map view of two drainage basins with chi values in their respective river networks. The straight black line in (a) is that which the elevation profile in Figure 8a is drawn along. The dashed black line in (b) represents the drainage divide between Basins I and II based on present-day geometry. The solid black line indicates the divide's position after 25 Ma of FastScape model time. Arrows indicate the direction of basin expansion and divide migration.

Figure 7 illustrates the migration of the drainage divide between Basins I and II. After 25 Ma of model time, the drainage divide has migrated towards and into Basin II. This has the effect of increasing the basin area and channel length of the former and decreasing the basin area and channel length of the latter. When chi values are equal on either side of the divide, ridgeline migration will stops and a stable drainage divide will be achieved. Even after 25 Ma of model time, the chi values in Basins I and II are still significantly different and indicate disequilibrium (Figure 7). The difference in chi values predict that with further modeling, Basin I will continue to expand at the expense of Basin II until equilibrium is achieved.

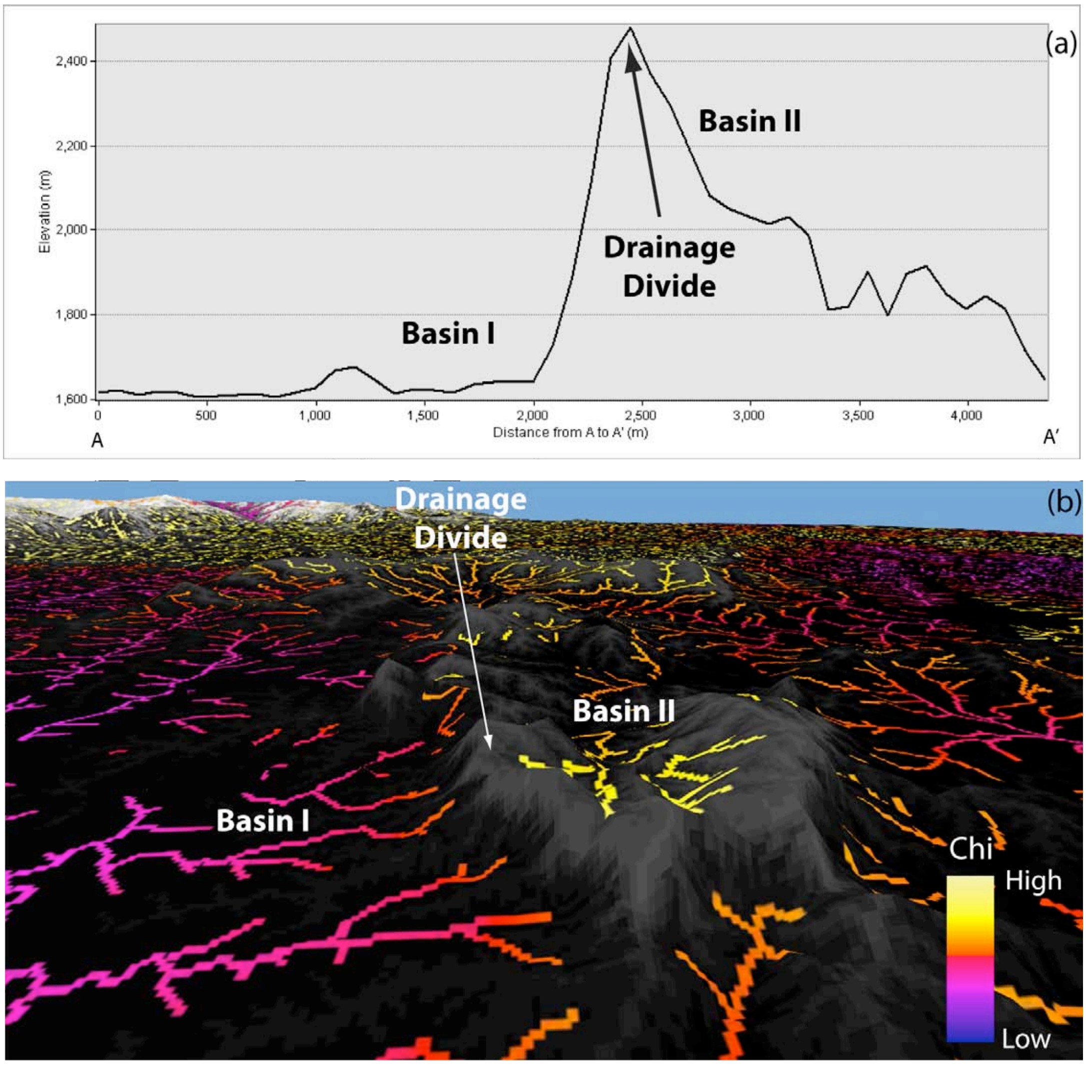

Figure 8. FastScape results for an area in the Himalaya 4101 domain after 25 Ma of model time with. (a) An elevation profile across the drainage divide between Basins I and II, as shown in Figure 7a and (b) a 3D oblique ArcGlobe view of the drainage divide and the chi values of Basins I and II on either side of it. The blue region in this image represents sky and does not represent base level.

3.3 Basin-Wide Cosmogenic ^{10}Be Erosion Rates

Cosmogenic nuclides, such as ^{3}He, ^{10}Be, ^{14}C, ^{21}Ne, ^{26}Al, and ^{36}Cl, are produced by spallation reactions induced by high-energy nucleons, secondary thermal neutron capture reactions, and muon-induced reactions (Gosse and Phillips, 2001). The production of in-situ terrestrial cosmogenic nuclides is dominantly controlled by the flux of galactic cosmic rays (with energies >100 MeV) through the Earth’s atmosphere (Cerling and Craig, 1994). This flux of nucleons (primarily protons and alpha-particles) is modulated by the strength of the Earth’s magnetic field; during periods of weaker magnetic strength, the flux is higher. Secondary neutrons responsible for cosmogenic nuclide production at the Earth’s surface are created during nucleonic interactions between galactic cosmic rays and elements in the Earth’s upper atmosphere. These secondary particles penetrate rocks, striking target atoms (e.g., O, Mg, Si, etc.) and cause spallation reactions that produce terrestrial cosmogenic nuclides (Gosse and Phillips, 2001). Cosmogenic ^{10}Be is the most commonly used and it is regularly measured in quartz-bearing lithologies.

The production rates of these nuclides in rocks are highest at the Earth's surface (e.g., 0-4 cm depth) and are dependent not only on the Earth's magnetic field strength, but also on the latitude and elevation where the rock sample of interest is located. Production rates increase with increasing latitude, where the modulation of the Galactic cosmic-ray flux by the geomagnetic field is weaker, and with increasing elevation, where there is "less atmosphere" to be penetrated by secondary particles before reaching Earth's surface (Gosse and Phillips, 2001; Dunai, 2010). Because neutrons, which cause most nuclide production, attenuate with depth, sample depth affects production rates. Generally, with increasing depth, the production rate of a cosmogenic nuclide decreases exponentially (Gosse and Phillips, 2001). Topographic shielding, as well as erosion, burial, and cover (i.e. soil, snow, dust, etc.) also affect the concentrations of cosmogenic nuclides in a given rock/mineral sample by decreasing production or shielding the rock entirely from production at all. Production rates of cosmogenic nuclides are reported relative to sea-level and high-latitude, and scaling factors are calculated for each sample site based on elevation and latitude (Gosse and Phillips, 2001). Shielding factors based on surrounding topography and sample depth are also determined and used to correct production rates.

Cosmogenic ^{10}Be concentrations in amalgamated quartz-rich sediment samples collected at basin outlets can be used to determine denudation/erosion rates of river. This amalgamation approach assumes that the quartz grains in the amalgamation originate in all parts of a catchment, that each grain records the ^{10}Be concentration starting at the time it spent at its source until its sample-collection-time position, and that each grain thus records the erosion rate at its source. The amalgamation of quartz grains acts as a catchment-average erosion rate. For example, quartz grains that originate in a slowly eroding source within the catchment will have higher ^{10}Be concentrations. Conversely, rapidly eroding landforms within a catchment will produce sediment more quickly, thus the grains spend less time on slopes and in stream basins, and thus they have lower cosmogenic ^{10}Be concentrations (Bierman, 1994; Bierman and Nichols, 2004; von Blanckenburg, 2005; Cockburn and Summerfield, 2004; Granger et al., 1996; Granger and Schaller, 2014).

The average cosmogenic nuclide concentration in well-mixed stream sediment yields the average erosion rate in a catchment, as long as the following assumptions hold true: (1) sediment is supplied at a rate that is proportional to the erosion rate; (2) the mineral being analyzed (e.g., quartz) is evenly distributed throughout the entire catchment; and (3) the cosmogenic nuclide in question was or were absent prior to erosion and exposure of the source (bed)rock at the Earth's surface (Bierman, 1994; Bierman and Nichols, 2004; von Blanckenburg, 2005; Cockburn and Summerfield, 2004; Granger et al., 1996; Granger and Schaller, 2014).

The production rate of ^{10}Be within a catchment, or basin, is determined using scaling factors and topographic shielding factors related to the drainage basin characteristics, such as elevation, relief, and roughness of terrain. Scaling factors for basin-wide, cosmogenic ^{10}Be erosion-rate studies are calculated by delineating the watershed and integrating elevation and latitude upstream of a cosmogenic sample site within a given basin. DEMs, typically 90-m or 30-m in resolution, are used to calculate a basin's mean elevation (von Blanckenburg, 2005; Codilean, 2006; Schaller et al., 2001). Codilean (2006) presents a GISc method based on relief shadow modeling to calculate the proportion of the incoming cosmic radiation that is shielded by a sample site's surrounding topography also using DEMs. The method is suitable for implementation in any GIS system with raster capabilities, as well as in landscape evolution models.

CHAPTER 4: GISc Methods and FastScape Input Parameters

4.1 GIS Methods

Study areas in Namibia and the central Himalaya (Figures 9 and 10) were selected that encompass basins with reported cosmogenic ^{10}Be erosion rates (Figures 11 and 12; Andermann, 2011; Bierman et al., 2007; Codilean et al., 2008, 2014; Godard et al., 2012; Wobus et al., 2005). NASA SRTM (Shuttle Radar Topographic Mission) 90-m DEMs of the study areas were downloaded as GeoTIFF files from the CGIAR-CSI Digital Elevation Database v4. CGIAR. ASTER GDEMs (30-m cell size) were also downloaded for study areas from the Japan Space Systems website (METI NASA, 2012).

NASA SRTM digital elevation data that is currently being distributed by NASA/USGS contains no-data voids where water or dark, heavy shadows prevented the quantification of elevation during data collection. These voids, though typically small, cause the DEM data to be less useful (CGIAR-CSI, n.d.), particularly in cases of hydrological modeling or numerical modeling (e.g., FastScape_Chi). Researchers at CGIAR-CSI further process original SRTM DEMs in order to fill in the no-data voids through production of vector contours and points, and the re-interpolation of these derived contours back into a raster DEM. Interpolated DEM values are then used to fill in the original no-data voids within the SRTM data (CGIAR-CSI, n.d.). ASTER GDEMs are not void-filled.

SRTM DEMs were loaded into ArcGIS (version 10.2.2) and mosaics made to create continuous DEM coverage of the areas of interest. Mosaics were also made of ASTER GDEMs. To test the effect domain size has on chi values, two domain sizes, were selected from the SRTM DEMs. The first domain contains 4101 cells x 4101 cells in study areas Namibia 4101 and Himalaya 4101. Subset domains of 1601 cells x 1601 cells of Namibia 4101 and Himalaya 4101 were created (Namibia 1601 and Himalaya 1601; Figures 11 and 12). The numbers 4101 and 1601 specify the number of cell rows (*ny*) and cell columns (*nx*) in each domain in FastScape.

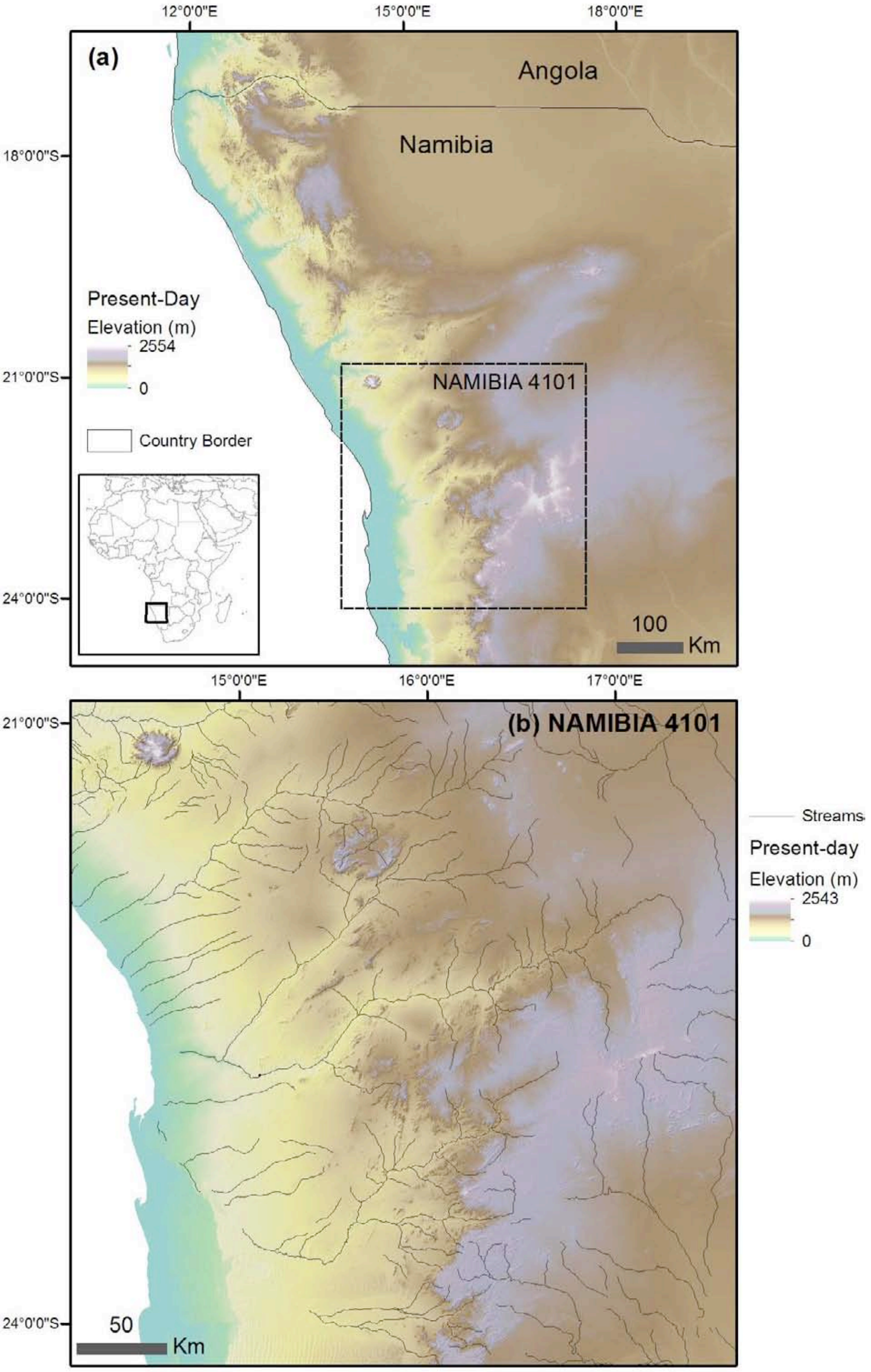

Figure 9. SRTM (90-m) shaded relief maps of present-day (a) Namibia and (b) study area Namibia 4101. The extent of Namibia 4101 is marked in map (a) by a dashed-line box. Streams are indicated by thin black lines. Inland water data was provided by (DIVA-GIS, 2015). All Namibia maps in this study are projected in the WGS84 UTM Zone 33S coordinate system.

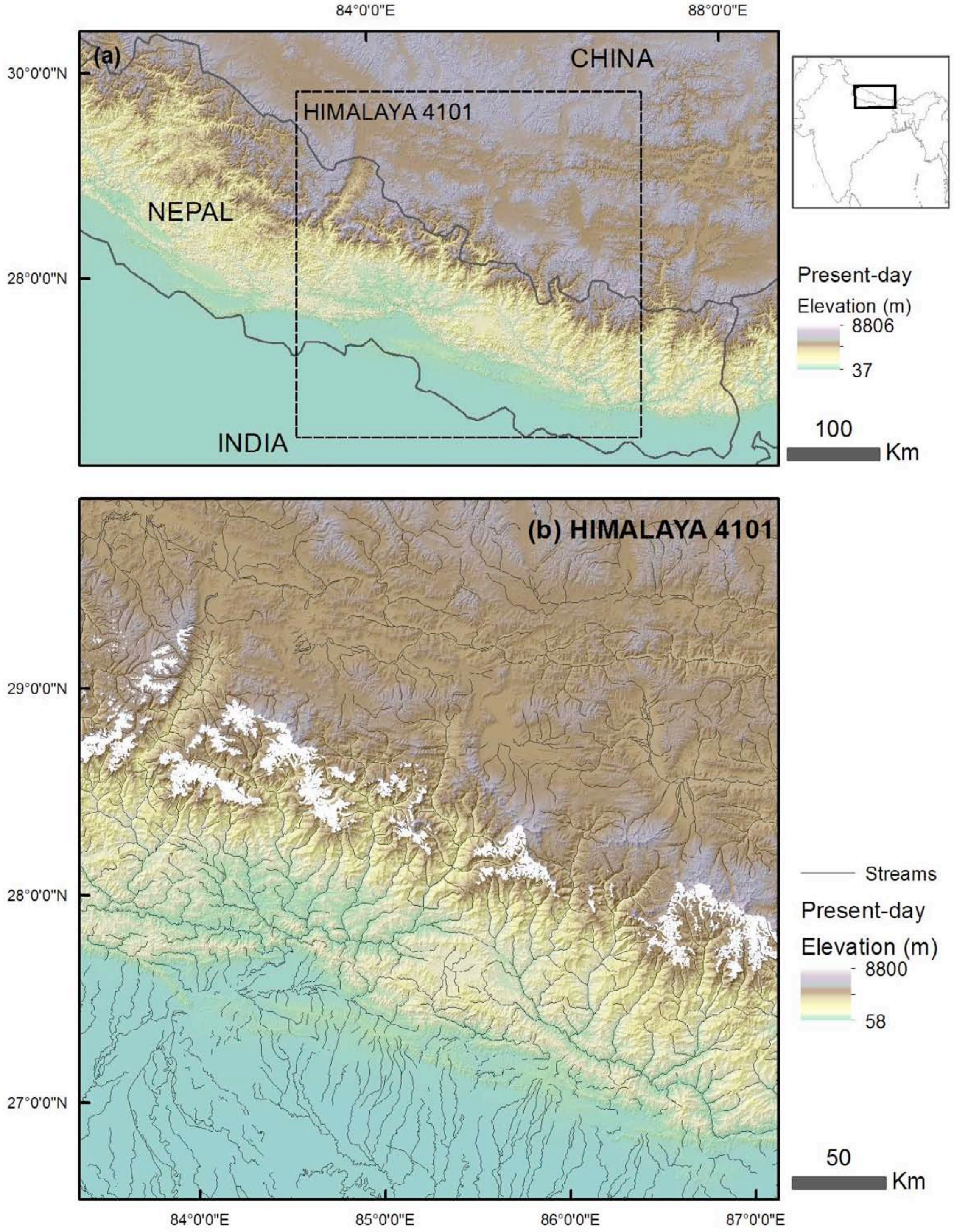

Figure 10. SRTM (90-m) shaded relief maps of the present-day (a) central Himalaya Mountains in Nepal and (b) study area Himalaya 4101. The extent of Himalaya 4101 is marked in map (a) by a dashed-line box. Black lines and white polygons indicate present-day streams and glaciers, respectively. Inland-water and 2010 glacier data were provided by (DIVA-GIS, 2015) and the (International Centre for Integrated Mountain Development (ICIMOD), 2015). All Himalaya maps in this study are projected in the WGS84 UTM Zone 45N coordinate system. Though the Himalaya are an active mountain range, fault lines were not mapped because uplift is treated as uniform in the FastScape model in this study.

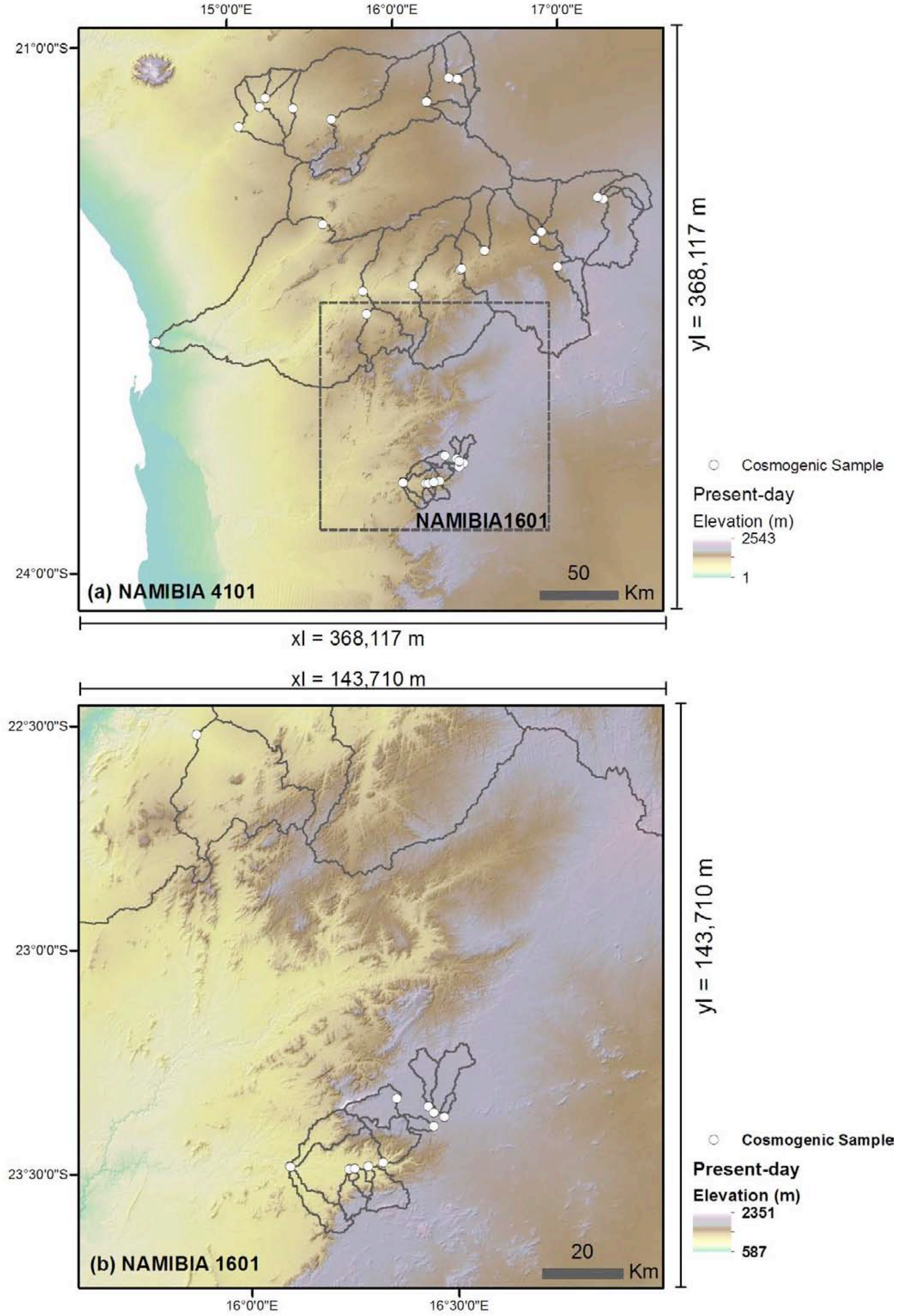

Figure 11. Present-day shaded relief, 90-m SRTM maps of study areas (a) Namibia 4101 and (b) Namibia 1601 with drainage basins (gray outlines) and associated cosmogenic^{10}Be sample sites (Codilean et al., 2008, 2014; Matmon et al. with Bierman, Kyle Keedy Nichols, 2007; Nichols, 2007).

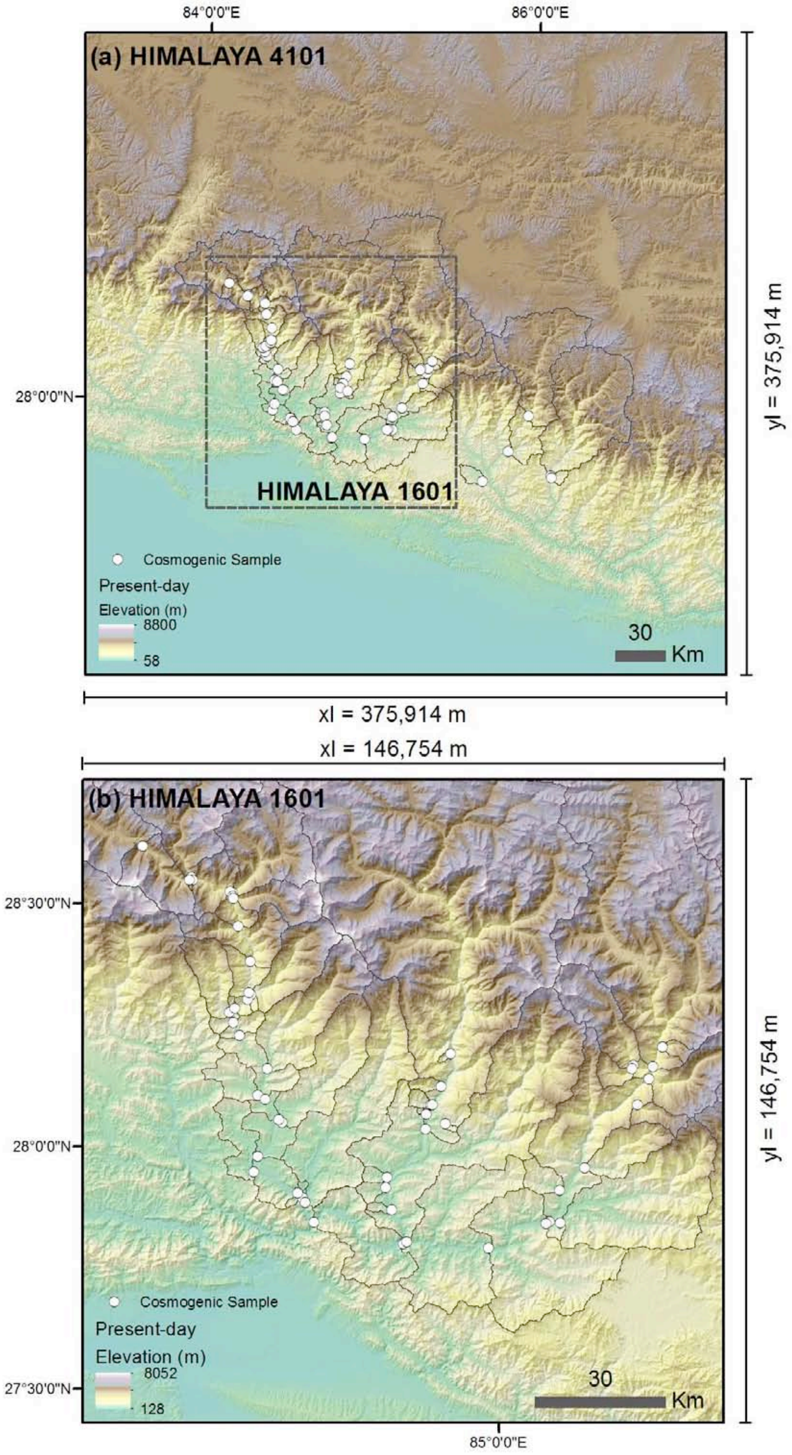

Figure 12. Present-day shaded relief, 90-m SRTM maps of study areas (a) Himalaya 4101 and (b) Himalaya 1601 with drainage basins (gray outlines) and associated cosmogenic ^{10}Be sample sites (Andermann, 2011; Godard et al., 2012; Wobus et al., 2005).

Two other domains (Namibia ASTER and Himalaya ASTER; Figure 13) were created from ASTER GDEMs with the same areas as those specified in Namibia 1601 and Himalaya 1601. The computer available during this study could not allocate enough memory to run FastScape with 30-m data for the larger areas covered by Namibia 4101 and Himalaya 4101, thus only the smaller subset domain was run with the finer 30-m resolution. Because the cell size is smaller, the number of cell columns and rows increased to 4794 and 4747 for Namibia ASTER and Himalaya ASTER, respectively. Square domains were used in this study ($nx = ny$), but FastScape can model rectangular domains as well ($nx \neq ny$)

All DEMs were projected in the appropriate WGS84 UTM projected coordinate system for Namibia (Zone 33S) and the central Himalaya (Zone 45N). The *Sink (Spatial Analyst)*, *Fill (Spatial Analyst), Flow Direction (Spatial Analyst)*, and *Flow Accumulation (Spatial Analyst)* tools were used to ensure that input DEMs used in the FastScape model have no sinks and continuous stream networks. Data were then exported as ESRI BIL (Band Interleaved by Line) files. FastScape uses the BIL file to help define the x (longitude), y (latitude), and z (elevation) geometry of the area to be modeled. In UTM projection, DEM latitudes and longitudes, as well as elevations, are stored as meters.

During initiation of FastScape computations, the first column and row are skipped as FastScape defines the rectilinear grid used in the finite difference method solution. Resultant chi-value and elevation DEMs are returned with 4100 columns and 4100 rows, and 1600 columns and 1600 rows, for the larger and smaller domains, respectively. The same occurs with Himalaya 4101 and Himalaya 1601 domains. This slightly changes the cell size in each of the new DEMs created by FastScape. To compare elevation and chi values produced from the Namibia 4101 and Himalaya 4101 domains to FastScape results produced in the Namibia 1601 and Himalaya 1601 domains, the larger domains were georeferenced and clipped to the same domain size as the smaller domains. Then they were resampled to the cell sizes of the smaller domains. The clipped Namibia 4101 and Himalaya DEMs were resampled using the *Resample (Data Management)* tool in ArcGIS and the nearest neighbor resampling technique.

4.2 FastScape Input Parameters

The FastScape algorithm requires user input to characterize the land surface that will be modeled/evolved. Table 1 and Appendix A list parameters used in FastScape input files for study areas in Namibia and the Himalaya.

4.2.1 Initial Conditions and Basic Geometry (Defining Domain and Cell Sizes)

First, FastScape requires in this case initial topography and definition of the basic geometry of the model domain. These initial conditions are supplied through information taken from a raster DEM. The DEM data used to define the initial topography in FastScape must be stored in a binary, direct access file as the number of columns (*nx*), rows (*ny*), and elevation (*z*) values (Figure 3). Values can be either real or integer numbers, as long as the lengths (e.g., two, four, or eight bytes) are specified (Braun, 2013; Braun and Willett, 2013). In this study, reprojected WG84 UTM ESRI BIL data are band 32-bit signed integer files with one band. The basic geometry of the model domain is further delimited by parameters *xl* and *yl*, which give the total length in meters in the east-west and north-south directions, where *xl* and *yl* are both equal to *nx* and *ny* times the cell size (Table 1; Figures 3, 11, 12, and 13; Appendix A). Cell-size information is found in the metadata of each BIL file.

4.2.2 Geomorphic Settings: Uplift, Precipitation, and Cosmogenic ^{10}Be Erosion Rates

Climatic and tectonic information in the study areas must be specified in the model. FastScape input parameters include variables for varied or uniform precipitation and uplift rates (Table 1). If rates vary in space, the user must specify the uplift and/or precipitation rates at the four corners of the model domain (Figure 14). Values are specified for *precipitation_v1*, *precipitation_v2*,… and/or for *uplift_v1*, *uplift_v2*…, in a counter-clockwise manner, starting from the lower left-hand corner of the domain. If the rates are uniform, only one rate (*precipitation_v1* and/or *uplift_v1*) must be specified. Units in FastScape are in m/yr.

Table 1. Values used in FastScape input files for Namibian and Himalayan study areas (Appendix A). Footnotes below summarize the variables, which are discussed in greater detail in the text and in the FastScape User Guide (Braun, 2013).

	NAMIBIA 4101	HIMALAYA 4101	NAMIBIA 1601	HIMALAYA 1601	NAMIBIA ASTER	HIMALAYA ASTER
Number of threads/cores to use						
num_threads[1]	8	8	8	8	8	8
Initial Topography						
restart[2]	-2	-2	-2	-2	-2	-2
convert[3]	little_endian	little_endian	little_endian	little_endian	little_endian	little_endian
DEM	NAMBI.bil	N4101.bil	NSMAL.bil	HSMAL.bil	NASTI.bil	HASTI.bil
Basic Geometry						
nx[4]	4101	4101	1601	1601	4794	4747
ny[5]	4101	4101	1601	1601	4794	4747
xl[6]	368117.31	375914.33	143710.27	146754.17	143754.00	146787.12
yl[7]	368117.31	375914.33	143710.27	146754.17	143754.00	146787.12
Time Steps						
dt[8]	100000.	100000.	100000.	100000.	100000.	100000.
nstep[9]	500	500	500	500	500	500
nfreq[10]	50	50	50	50	50	50
Fluvial Erosion Law						
law[11]	2	2	2	2	2	2
m[12]	0.4	0.4	0.4	0.4	0.4	0.4
n[12]	0.9	0.9	0.9	0.9	0.9	0.9
k_f[13]	0.1e-05	0.1e-05	0.1e-05	0.1e-05	0.1e-05	0.1e-05
Boundary Conditions						
Boundary_condition[14]	0001	1000	0001	0001	0001	0001
Precipitation						
precipitation_n[15]	1	0	0	0	0	0
precipitation_v1[16]	0.005 *	1.0	0.2	1.0	0.2	1.0
precipitation_v2[16]	0.25 *	--	--	--	--	--
precipitation_v3[16]	0.45 *	--	--	--	--	--
precipitation_v4[16]	0.005 *	--	--	--	--	--
Uplift Rate						
uplift_n[17]	0	~0.01 (See Footnote 18)	0	~0.01 (See Footnote 18)	0	~0.01 (See Footnote 18)
uplift_v1[18]	0.010e-03	--	0.010e-03	--	0.010e-03	--
uplift_v2[18]	--	--	--	--	--	--
uplift_v3[18]	--	--	--	--	--	--
uplift_v4[18]	--	--	--	--	--	--
Plotting Options[19]						
plot_chi	1	1	1	1	1	1
plot_DEM	2	2	2	2	2	2
plot_rate	1	1	1	1	1	1
vtk[19]	1	1	1	1	1	1

Note: -- indicates the parameter is not applicable. * See text for details.

[1] Number of threads/processors to be used during the FastScape run to speed up processing time. Limited to the number of threads/processors on the computer in use.

[2] When restart is set to -1, a binary 16-bit signed integer DEM file with nx*ny integer*2 numbers is used to define the initial topography in the FastScape model. When restart = -2 the DEM file is a binary 32-bit signed integer with nx*ny integer*4 numbers.

[3] Raster data exported as a ESRI BIL file has a little endian byte order. This information is found in the .hdr file accompanying the .bil file.

[4] Number of grid points in the x-direction (e.g., columns).

[5] Number of grid points in the y-direction (e.g., rows).

[6] Length of domain model in east-west direction (longitude). Equal to nx*cell size (using UTM projection in meters). In the respective UTM projections for the original Namibian and Himalayan SRTM DEMs, cell sizes are 89.72681625 and 91.66406561 m, respectively. In the respective UTM projections for the original Namibian and Himalayan ASTER GDEMs, cell sizes are 29.98623302 and 30.92208078 m, respectively.

[7] Length of domain-model in north-south direction (latitude). Equal to ny*cell size (using UTM projection in meters). In the respective UTM projections for the original Namibian and Himalayan DEMs, cell sizes are 89.72681625 and 91.66406561 m, respectively. In the respective UTM projections for the original Namibian and Himalayan ASTER GDEMs, cell sizes are 29.98623302 and 30.92208078 m, respectively.

[8] Time-step length (years)

[9] Number of time steps

[10] Specifies the frequency of FastScape output files.

[11] Specified fluvial erosion (incision) law to be used: 1 = the unit stream-power law, assuming a linear slope dependence (where n=1); 2 = the general unit stream-power law. See text for details. The default setting for *law* is an implicit finite-difference implementation of the partial differential equations. When -1 or -2 are used, the explicit form of the finite-difference implementation is used.

[12] The discharge exponent (m) and the slope exponent (n) in the fluvial erosion-law equations.

[13] The K coefficient in the fluvial erosion-law equations.

[14] Boundary_condition value is a 4-digit integer, where each integer corresponds to the bottom, right, top, and left sides (boundaries) of the domain model (Figure 14): 0 = reflective boundary; 1 = base-level boundary where height (h) is set to 0; see text for more detailed explanation.

[15] Precipitation function: 0 = constant for every cell; 1 = resulting precipitation function is a bilinear interpolation of the v1, v2, v3, and v4 values (Figure 14) inside the domain.

[16] Precipitation rate (m/year).

[17] Uplift function: 0 = constant; 1 = resulting uplift function is a bilinear interpolation of the v1, v2, v3, and v4 values (Figure 14) inside the domain.

[18] Uplift rate (m/year). For Namibia, this value was set at 0.010e-03 m/yr based on isostatic uplift rates reported in (Stollhofen et al., 2014). The uplift rate for the Himalayas is based on the following Fortran code and an initial uplift rate of ~0.01 m/yr for the central Himalaya (Lavé and Avouac, 2000, 2001). After 100,000 years, the uplift rate decreases from 0.005 m/yr to 0.010e-03 m/yr, the same as that of Namibia:

```
!/uplift_start/
uplift=0.010
if (time.gt.1.e5) uplift=uplift/1000.
!/uplift_stop/
```

[19] Output files are printed every nfreq for specified variables. In this case, results for time- and space-dependent χ, topography, and erosion rates are printed in .bmp images, .dem files, and .vtk files. These can be viewed with software such as ArcGIS, QGIS, and Paraview.

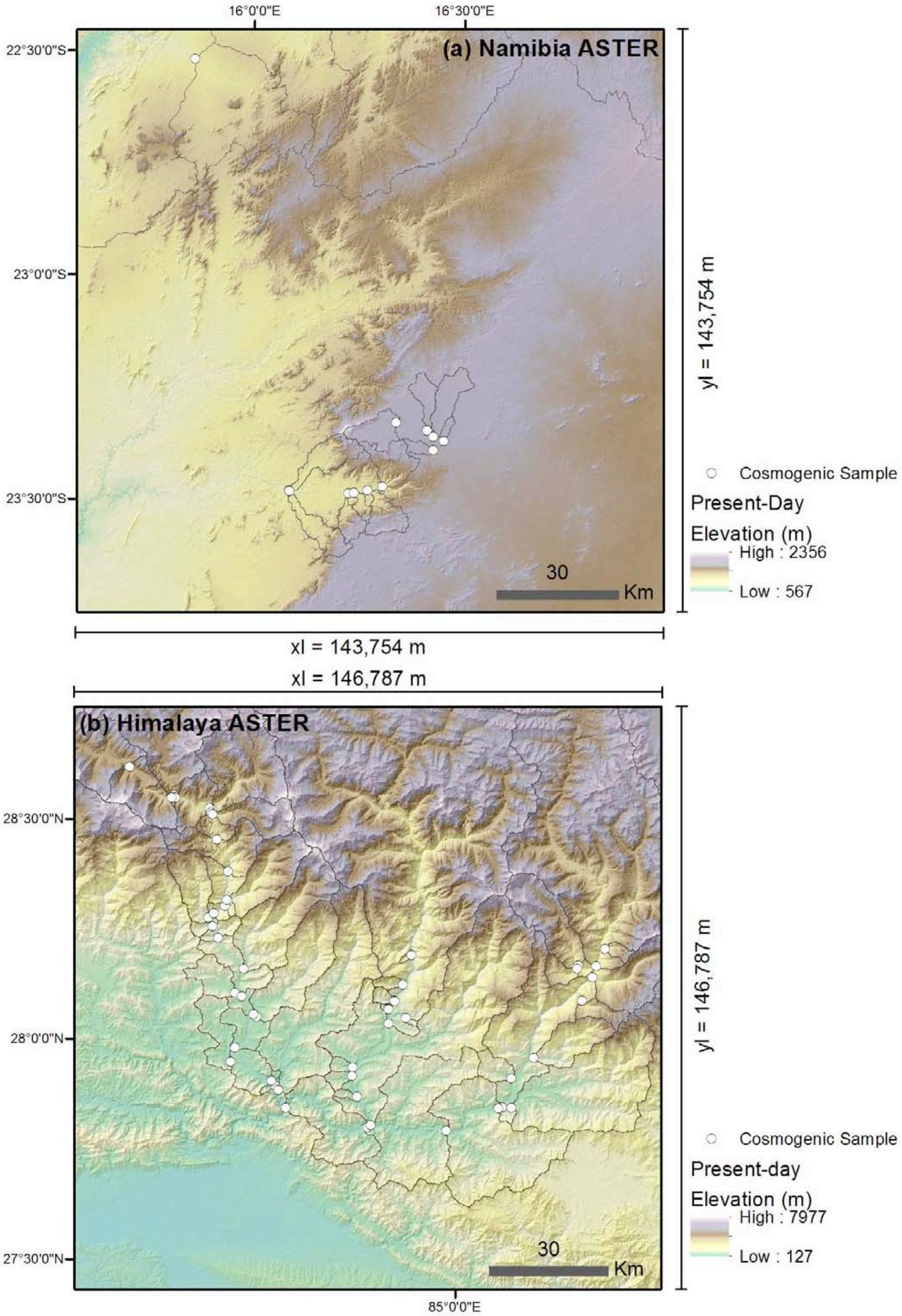

Figure 13. Present-day shaded relief, ASTER GDEMs (30-m) of study areas (a) Namibia ASTER and (b) Himalaya ASTER with drainage basins (gray outlines) and associated cosmogenic ^{10}Be sample sites (Andermann, 2011; Codilean et al., 2008, 2014; Godard et al., 2012; Bierman et al., 2007; Wobus et al., 2005).

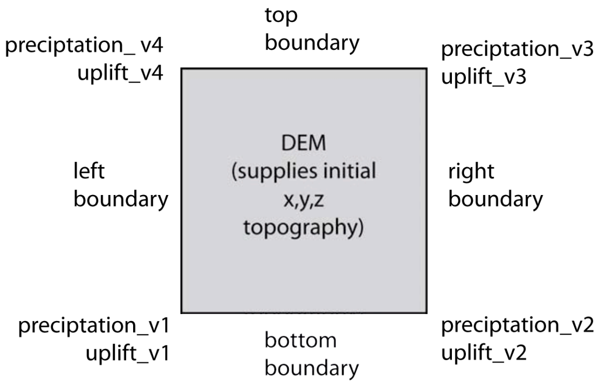

Figure 14. A schematic diagram illustrating the location of FastScape algorithm parameters in relation to the initial topography and boundary conditions.

Namibia is located on the southwestern coast of Africa (Figure 9) along a passive continental margin, where tectonic activity is minimal and weathering and erosion are the dominant surface processes. Passive margin geomorphology is produced by positive and negative feedback between uplift from crustal tectonics -- horizontal crustal extension, flexural loading and unloading, mantle-convection heat flow, and pre-existing lithospheric structures -- and Earth-surface processes, such as denudation and sedimentation, which are controlled by climate. Isostatic response to denudation helps shape Namibia's topography, which is characterized by a wide coastal plain pediment to the west, a steep coast-parallel Great Escarpment, and rolling highlands east of the escarpment (Figure 15) (Bierman and Caffee, 2001; Van der Wateren and Dunai, 2001). Elevation ranges from sea level to 2554 meters (Figure 9). According to Stollhofen et al. (2014) Namibia has been experiencing an uplift rate of 0.0012 ± 0.005 cm/yr for the past ca. 2.5 Ma. Where the Great Escarpment is not a distinct, massive feature, it is dissected, and the transition from the hyper-arid, coastal Namib Desert to the humid highlands is more gradual. Precipitation along the coast is approximately 5 cm/yr, whereas the highlands above the escarpment receive between 25 cm/yr in the southeast and 45 cm/yr in the northeast (Bierman and Caffee, 2001). Basins of interest to this study (Codilean et al., 2008, 2014; Bierman et al., 2007) drain to sea level in the east.

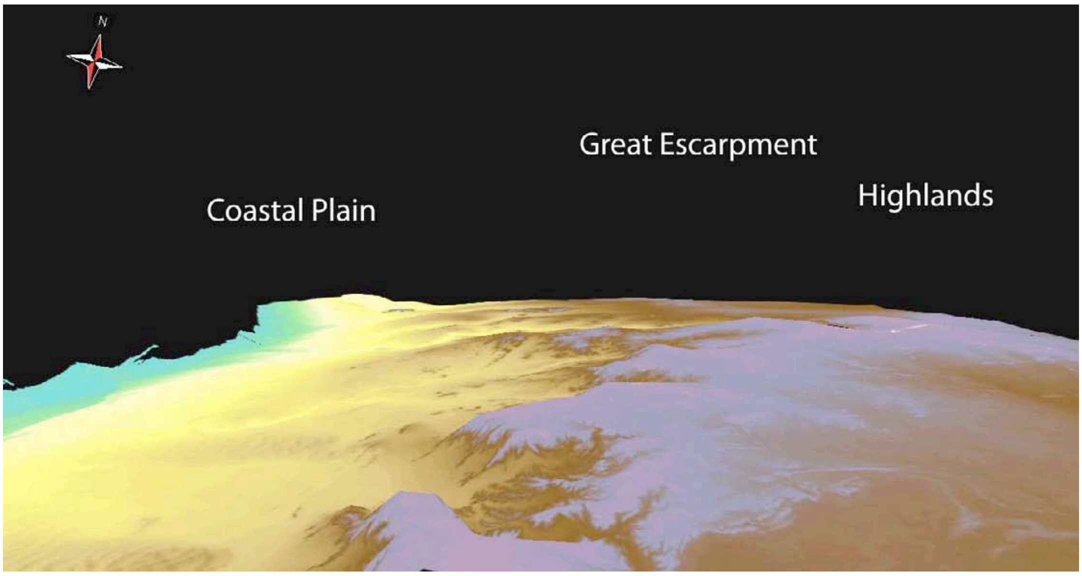

Figure 15. An oblique ArcGlobe view of a 90-m SRTM of Namibia 4101. The elevation scale (1 to 2543 m) and scale colors are the same as those in Figure 9b. A vertical exaggeration of 7 is used to demonstrate the steep transition in topography that occurs at the Great Escarpment. ArcGlobe does not display scales or legends.

The Himalaya are a mountain chain that has been experiencing active mountain-building for the past ~20 Ma due to a continent-to-continent collision between India and Eurasia (Dupont-Nivet et al., 2010; Molnar and Tapponnier, 1975). The chain is one of the youngest and highest mountain ranges on Earth. The mountains extend approximately 2500 km from east to west between India and China (Figure 10). High relief characterizes the Himalaya, with elevations that range from ~200 m in the low-lying Ganges Plains to 8850 m peaks in the Higher Himalaya. This change in elevation occurs over a short ~250-km distance in a roughly north-south direction. The Tibetan Plateau, which borders the Higher Himalaya to the north exhibits low relief, but has overall elevations greater than 5000 m. The region of interest for this study (Himalaya 4101; Figures 10 and 16) is an area in the central Himalaya of Nepal. Basins of interest to this study (Andermann, 2011; Godard et al., 2012; Wobus et al., 2005) have headwaters on the Tibetan Plateau and in the Higher Himalaya that drain to the Ganges Plains in the south, where the waters join the Ganges River. Active uplift is occurring in the central Himalaya at a rate of ~50 - 150 cm/yr (Lavé and Avouac, 2000, 2001; Scherler et al., 2014), which is two to three orders of magnitude greater than the weak uplift occurring in Namibia. Precipitation rates in the Himalaya are an order of magnitude higher than rates in Namibia.

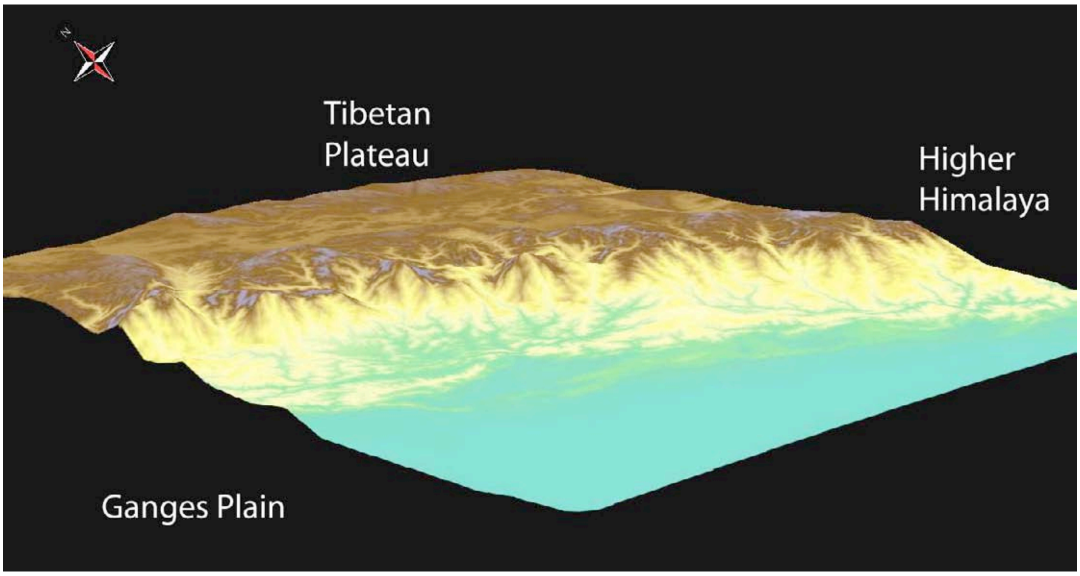

Figure 16. An oblique ArcGlobe view of a 90-m SRTM of Himalaya 4101. The elevation scale (54 m to 8800 m) and scale colors are the same as those in Figure 10b. A vertical exaggeration of 5 is used. ArcGlobe does not display scales or legends.

Mean precipitation rates range from 120 cm/yr to 210 cm/yr for small Himalayan basins, whereas larger, main-stem basins have mean precipitation rates of 50 to 100 cm/yr (Table 2; Andermann, 2011).

In FastScape models of the Namibia 4101, Namibia 1601, and Namibia ASTER domains, a uniform uplift rate of 0.000010 m/yr was selected (Stollhofen et al., 2014); every cell in the DEM has the same uplift rate. Because the area of Namibia 1601 and Namibia ASTER is significantly smaller and mostly in the wetter regions of Namibia, a uniform precipitation rate of 0.200 m/yr was set for both models. Namibia 4101 was first run with a uniform precipitation rate of 0.200 m/yr to compare these results to those produced by FastScape modeling of Namibia 1601 and Namibia ASTER. A second Namibia 4101 model run used precipitation rates based on drier conditions along the coast (*precipitation_v1* and *v4* = 0.005 m/yr) and wetter conditions in the northeast *(precipitation*v_3 = 0.45 m/yr) and southeast (*precipitation_v2* = 0.25 m/yr) (Table 1; Figure 14; Bierman and Caffee, 2001). A bilinear interpolation of these *v1*, *v2*, *v3*, and *v4* values inside the domain was computed by FastScape.

A uniform precipitation rate of 1 m/yr was used in the Himalaya 4101, Himalaya 1601, and Himalaya ASTER models. A tilted uplift rate, with a slightly higher rate on the northern boundary than on the southern boundary, was initially prescribed as the uplift parameter in

FastScape. This would have been simplified version of differential uplift in the High Himalaya and Tibetan Plateau relative to the Ganges Plain; however, with this tilted uplift, FastScape was not able to resolve local minima problems, nor was it able to create a fully connected stream network, on which calculation of representative chi values relies. The uplift rate for each of the three Himalaya models was, thus, defined using a Fortran script within FastScape (Table 1) that initiated a uniform 'pulse' of uplift for the first 100,000 years at a rate of 0.010 m/yr. Approximately 1000 m of elevation was initially added to the Himalaya landscape in this manner. From that point in time onward, uplift was decreased to the same slow uplift as that Namibia experiences due only to denudation and isostasy. Similar to models run in Willett et al. (2014) this 'pulse' uplift helps force river basin reorganization, in order to see the effect on chi values in this study.

Table 2. Summary of precipitation, uplift, and cosmogenic ^{10}Be erosion rates of study areas in Namibia and the central Himalaya.

	Present-Day Elevation (m)	**Average Elevation ± Standard Deviation (m)**	**Precipitation Rate (cm/yr)**	**Uplift Rate (cm/yr)**	**Published ^{10}Be Erosion Rates (m/Ma)**
Namibia	0 - 2554	1107 ± 500	5 - 45	0.0012	3 - 18
Central Himalaya	58 - 8800	3051 ± 2212	50 - 210	5-150	214 - 6689

Erosion rates are not input parameters required by FastScape, but presenting published cosmogenic ^{10}Be erosion rates here for select basins in Namibia and the Himalaya (Table 2) helps provide further perspective on the different geomorphic settings found in these regions.

Based on cosmogenic ^{10}Be in quartz-bearing bedrock, dry-river, stream-channel samples, and desert-surface samples, Bierman and Caffee (2001) inferred that the Namibian landscape (e.g., the Namib Desert, the Great Escarpment, and the adjacent Namibian highlands) has been in topographic steady-state characterized by slow erosion for at least the past million years. They also suggest that their cosmogenic data do not support a model of significant and on-going escarpment retreat.

Cosmogenic ^{10}Be data from stream and river sediment indicate that the Namibian landscape is eroding more rapidly than exposed bedrock outcrops (~3 m/Ma), and that the Great Escarpment is eroding more rapidly (~16 m/Ma) than the basins in the highlands (~5 m/Ma) or on the coast plain (~8 m/Ma) (Bierman and Caffee, 2001). Bierman and Caffee (2001) further conclude that Namibian erosion rates have reached a steady state and have not been changing over long periods of time. Codilean et al. (2008; 2014) report erosion rates that range from 4 to 18 m/Ma for small catchments in Namibia, and determine a slope-erosion rate relationship, which indicates catchments that have erosion rates that are slope dependent are not in topographic steady state.

As expected, erosion rates in the more humid and tectonically active Himalaya are significantly different than those in more arid and tectonically inactive Namibia (Table 2). Cosmogenic ^{10}Be erosion rates (~90 to ~7400 m/Ma) reported for 69 select central Himalaya catchments (Andermann, 2011; Godard et al., 2012; Wobus et al., 2005) are two to three orders of magnitude higher than those reported for Namibia catchments. The Himalaya is experiencing ongoing denudation that accompanies active uplift. The range has also experienced glacial erosion and still has many active glaciers (Figure 10). Different camps of geoscientists argue that the Himalaya are or are not in a state of dynamic equilibrium (Andermann, 2011; Dortch et al., 2011; Finnegan et al., 2008; Godard et al., 2012, 2014; Henck et al., 2011; Hirschmiller et al., 2014; Kirby et al., 2003; Kirby and Harkins, 2013; Ouimet et al., 2010, 2009; Reynhout, 2011; Scherler et al., 2014; Vance et al., 2003). Lavé and Avouac (2001) argue that erosion (denudation) rates in the central Himalaya balance high rates of tectonic uplift through bedrock landsliding, which is in turn, driven by fluvial incision. The debate has not been resolved and continues to be a hot topic in Earth-science research.

4.2.3 Fluvial Erosion Law

In its current version, FastScape includes fluvial erosion laws, but no hillslope processes equations (Braun, 2013; Braun and Willet, 2013). Users can select from the following governing equations corresponding to the (1) unit stream-power law assuming linear slope dependence (n = 1; Equation 25); (2) unit stream-power law (Equation 26); and (3) the ξ – q model of Davy and Lague (2009):

$$\frac{\partial h}{\partial t} = -K_f \phi^m S \qquad \text{Eq. (25)}$$

$$\frac{\partial h}{\partial t} = -K_f \phi^m S^n \qquad \text{Eq. (26)}$$

$$\frac{\partial h}{\partial t} = -K_f \phi^m S^n + \frac{Q_s}{\alpha Q_w} \qquad \text{Eq. (27)}$$

where Q_s and Q_w are sedimentary and water discharge, respectively. In this study, the unit stream-power law is used (Eq. 26) in concert with K_f, m, and n values (Table 1) similar to those used by Willet et al. (2014). Exhaustive sensitivity testing on these variables ($m/n = 0$ to 0.60) showed that m/n values of 0.35 to 0.50 were optimal for calculating chi in their study areas (Willet et al., 2014).

4.2.4 Boundary Conditions: Setting Base-Level

Boundary conditions for each FastScape model are set with a 4-digit integer. The first, second, third and fourth integers corresponding to the bottom, right, top, and left sides (boundaries) of the model domain (Figure 14). FastScape offers four types of boundary conditions represented by the integers 0, 1, 2, or 3 (Braun, 2013).

When a boundary is set at 0, the boundary is reflective, meaning that no water flux passes through the boundary. The boundary nodes have a limited number of neighbors ($N(i,j)$) to which they can potentially drain. There is an exception to this condition: If the opposite boundary is also set at 0, a periodicity is assumed between the opposing boundary sides. The two opposite sides of the mesh communicate with each other in such a way that nodes on one boundary have nodes on the other boundary as neighbors. In this way, water that flows across one boundary must 'reappear' on the other boundary (side) (Braun and Willett, 2013).

A boundary set at 1 is set at base level, and the boundary's height is fixed through the entire model run. When adjacent boundaries are each set at 2, all but the corner are defined as reflective; the corner they share is set at base level ($h(b_i) = h_0(t)$). A boundary set at 3 defines, all but the center of the boundary at base level. The rest of the boundary is reflective.

Rivers in the areas of interest flow predominantly to the east in Namibia and to the south-southwest in the Himalaya. Except for Himalaya 4101, the left boundary of each domain is defined as the base-level boundary condition in the FastScape models of Namibia and Himalaya. The base-level boundary condition for Himalaya 4101 is set at the bottom, because of the position of the major stream draining the basins in the area with respect to the DEM coverage.

4.2.5 Local Minima and Time Steps

Though the FastScape model begins its analysis with a depressionless DEM, local minima or 'sinks' are sometimes created during computation due to how the x (longitude), y (latitude), and z (elevation) values respond to uplift and precipitation parameters – the driving forces in the algorithm. If these sinks are not nodes on a model boundary, they create closed basins, which exist in the digital topography, but not in reality. The closed basins disconnect stream networks, and create their own base levels (z_{cb}) to which cells in a given catchment will drain. Subsequently, chi values calculated for a closed basin are relative to z_{cb} rather than z_b, which is defined at one or more of the model boundaries.

FastScape computes discharge based on the principle of water conservation. When the algorithm encounters a sink node that is not situated along a boundary, the node is read as a local minimum, meaning its elevation is lower than that of all its neighbor nodes. This node drains the discharge through a point that is not on a model boundary, and thus that precipitation/discharge does not reach base level. Minima are likely to arise in areas of the modeled landscape that are flat and where random perturbations have been added by FastScape in order to seed drainage network growth, and thus, connectedness (Braun and Willett, 2013).

Though FastScape offers a computational solution, where the user can specify a situation where evaporation or infiltration compensates for precipitation that does not reach a model boundary, this is not the most realistic choice for the Namibia and the Himalaya models. Instead, the second computational solution offered by FastScape is used. In this case, the algorithm finds a path for water to flow toward a model boundary by forming one or a series of 'lakes,' and determines the 'sill' of each lake, where water will flow from its lowest elevation. By specifying that all modeled precipitation must drain through the model boundaries, Braun and Willett (2013) ensure that FastScape behaves in a predictive manner, rather than becoming significantly dependent on the formation of local minima.

During the ordering phase in construction of the stack, FastScape tags each node with a catchment number $c(i)$ denoting the base-level node to which it inevitably drains. When a node is identified as self-draining, the tag is assigned a negative number. FastScape then identifies all nodes with negative catchment numbers and that have a neighbor with a positive catchment number. In this manner, FastScape is able to select the node that is the lowest in elevation and identify the neighbor as the sill of the catchment. This sill is then forced by the algorithm to become the receiver node of the local minima, and all nodes in that catchment are assigned to the positive catchment of the sill node. The sink nodes will then drain into a neighboring node, rather than draining themselves (Braun and Willett, 2013). Not all sinks can be dealt with in just a single pass of the algorithm, as there will be cases where nodes with negative catchment numbers still have no neighbor nodes with positive catchment numbers; iterations of the algorithm are required.

As FastScape continues in successive iterations, the sills are eroded, sinks are removed, the number of negative catchment nodes decreases, until finally, the algorithm converges, and the digital stream networks become fully connected. It is important to note that the rate of convergence is difficult to predict and is highly dependent on the digital landscape geometry. Braun and Willett (2013) state that the maximum number of iterations is likely bounded by the square root of n_p in rectangular grids, and that in most cases only the first several time steps of the model run are affected by local minima.

This is not the case for the Namibia and Himalaya models. Up to 10,000 time steps (at $dt = 1$, 100, and 1000 years) using either the implicit or explicit solution of the finite difference method for each model still produced local minima and disconnected stream networks. It is only with larger time steps of $dt = 10{,}000$ or 100,000 and after >25 Ma of model time that a connected stream network, and thus connected chi network is created. This is a significant period of time, whether model or geologic in nature, which causes significant changes to the landscape (e.g., erosion of ridge divides, approaching stream capture in some drainages). Thus, FastScape analysis of Namibia and Himalaya models cannot reasonably calculate a network of χ values for the present-day topography.

CHAPTER 5: RESULTS

A total of 50 Ma model time was needed in FastScape to remove local minima and create fully connected stream networks in Namibia 1601 and Himalaya 1601, thus results for all domains, including the ASTER domains are first presented for the 50 Ma time step, in order to compare chi values. Results for the 25 Ma results for Namibia 4101 and Himalaya 4101 are then presented.

5.1 FastScape Results after 50 Ma (model time)

Elevations in the present-day Namibia 4101 domain range from 0 m to ~2540 m. DEMs in the Namibia 1601 (90-m cell size) and Namibia ASTER (30-m cell size) domains, which are located further inland and on the Great Escarpment have present-day elevations ranging from ~590 to ~2350 m and ~570 to ~2360 m, respectively. For the first part of this study, uniform precipitation and uplift rates of 0.20 m/yr and uplift rate of 0.010e-03 m/yr, respectively, were used in each Namibia model domain. Base level is set at sea level for Namibia 4101, whereas base level is set at 587 m and 567 m for Namibia 1601 and Namibia ASTER, respectively. These are the lowest elevations found along the western boundary of each domain. After 50 Ma of FastScape model time, Namibia 4101 elevations range from 0 to ~2350 m and associated non-zero chi values are between 3 m and ~79,000 m. After 50 Ma, Namibia 1601 and Namibia ASTER elevations range from 587 to ~2600 m and 569 to ~2410 m, respectively. Associated non-zero chi values for these domains are between 3 and ~57,000 and between 1 and ~32,000, respectively (Table 3; Figures 17, 18, 19, and 23).

Elevations in the present-day Himalaya 4101 domain (58 – 8800 m) are considerably higher than those in the present-day Namibia 4101 region. The Himalaya 1601 (90-m cell size) and Himalaya ASTER (30-m cell size) domains have present-day elevations ranging from ~130 to ~8050 m and ~130 to ~7980 m, respectively. With the uniform, 'pulsed' uplift rate of 0.010 m/yr for the first 100,000 years of the FastScape model, approximately 1000 m of elevation was added to range of elevations after the first 100,000 years of the Himalaya models. A precipitation rate of 1 m/yr did not create

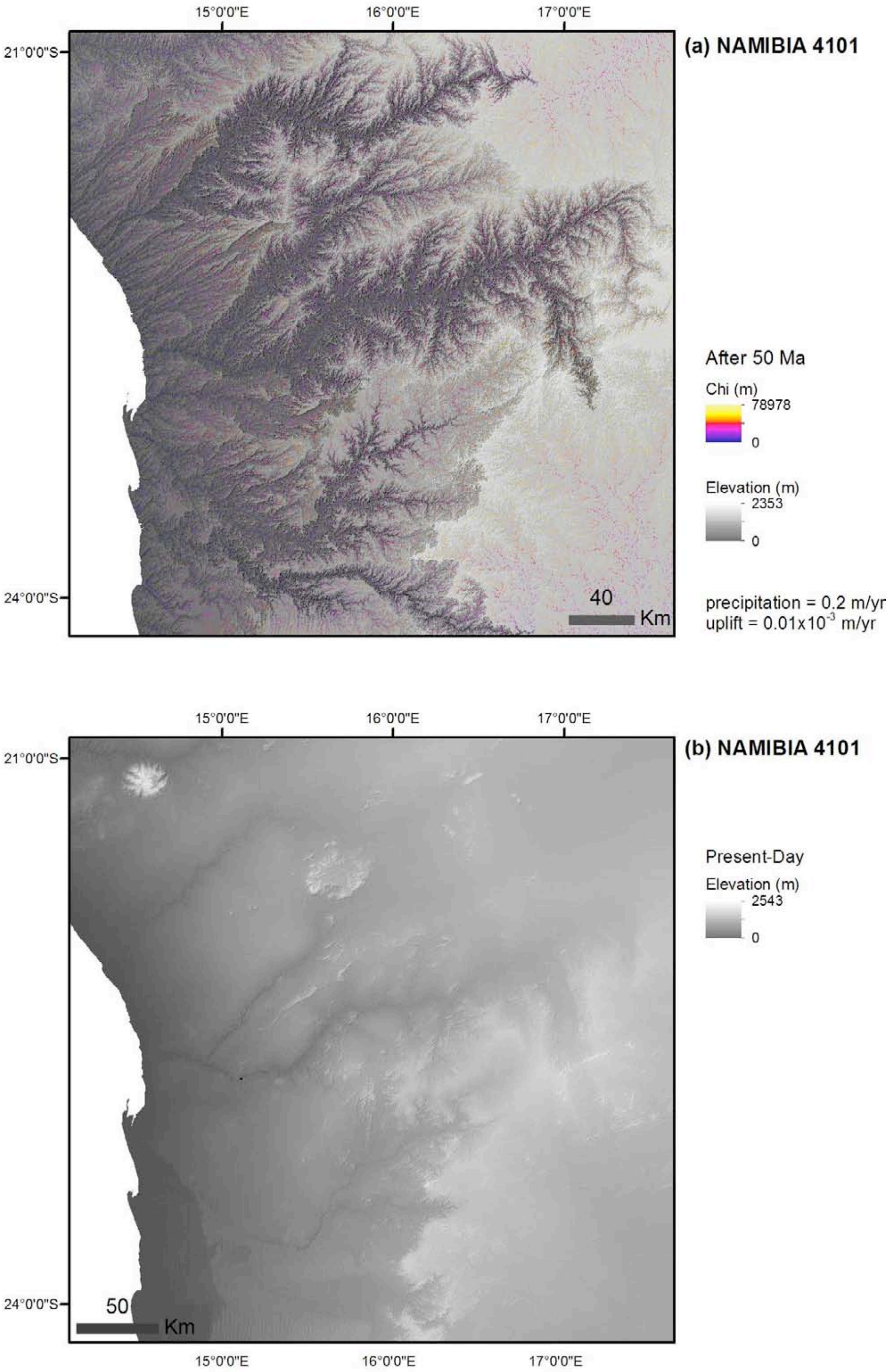

Figure 17. Comparison of topography from a 90-m shaded-relief DEM produced after 50 Ma (a) by FastScape and (b) present-day, shaded-relief topography for the Namibia 4101 study area. Chi values are also shown overlying the 50 Ma topography. Precipitation and uplift values used in FastScape input (Table 1) are listed.

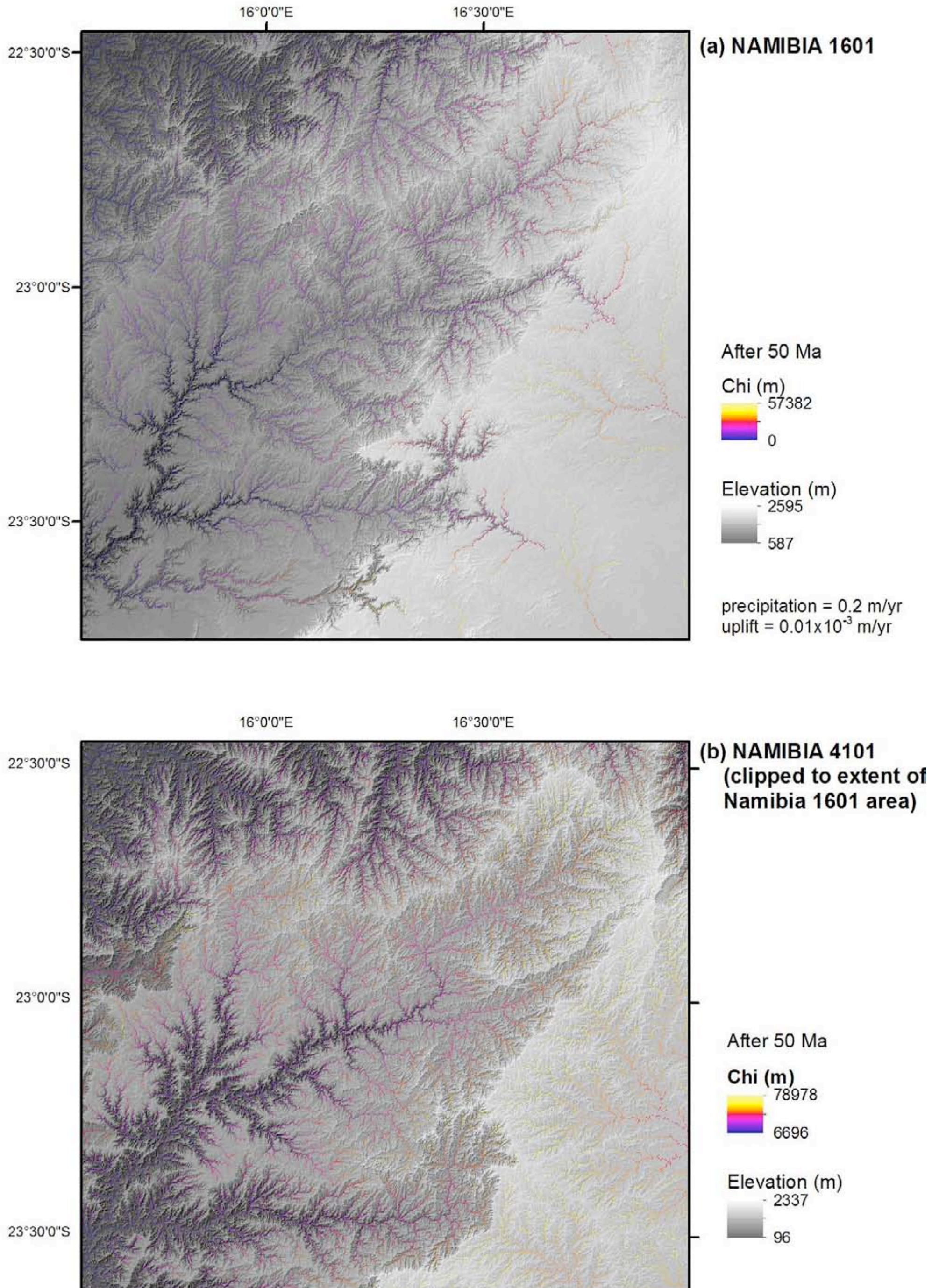

Figure 18. FastScape chi-value and topographic, shaded-relief 90-m DEM results after 50 Ma for the (a) Namibia 1601 study area compared to (b) results clipped from the Namibia 4101 domain. Precipitation and uplift values used in FastScape input (Table 1) are listed.

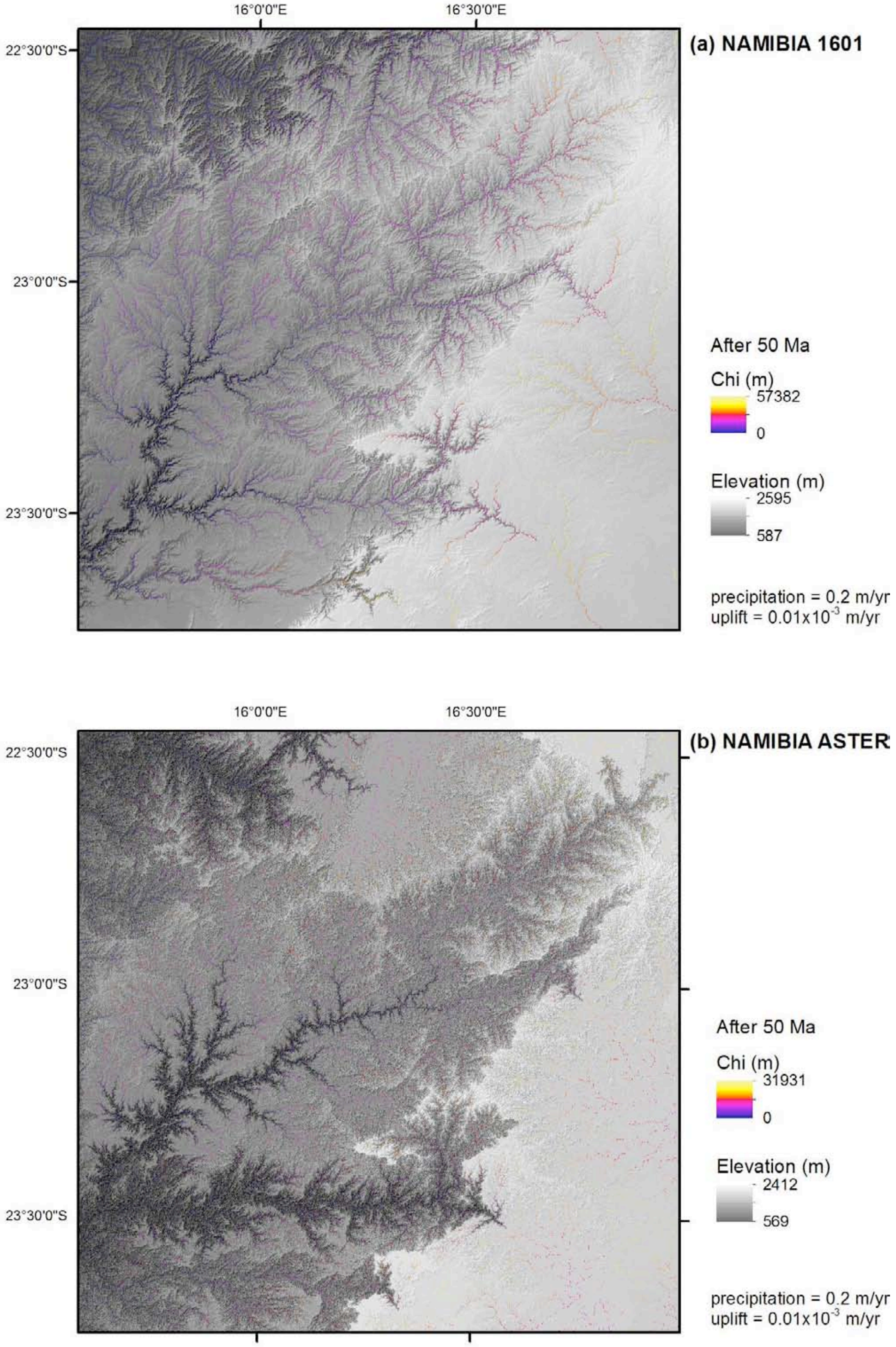

Figure 19. Comparison of FastScape chi values and topography from (a) a 90-m shaded-relief DEM produced after 50 Ma by FastScape for the Namibia 1601 domain, and (b) a 30-m shaded-relief DEM topography for the Namibia ASTER domain. Precipitation and uplift values used in FastScape input (Table 1) are listed.

enough erosion to keep elevations from becoming unrealistically high when a uniform uplift rate had been used throughout the entire model run. The 'pulsed' uplift rate was used to create an uplift scenario that somewhat mimics active uplift and that is significantly different to that used in the Namibia model. Base-level elevations of 58, 128, and 127 are set for Himalaya 4101, Himalaya 1601 and Himalaya ASTER, respectively. These are the lowest elevations found along the western boundary of each domain. After 50 Ma of FastScape model time, Himalaya 4101 elevations changed to a range of ~1560 to ~6230 m, with associated non-zero chi values that are between 3 m and ~129,000 m. After 50 Ma, elevations in Himalaya 1601 and Himalaya ASTER domains range from 128 to ~7250 m and 127 to ~7240 m, respectively. Associated non-zero chi values for these domains are between 3 and ~58,000 m and between 1 and ~37,000 m, respectively (Table 3; Figures 20, 21, 22, and 23).

Table 3. Elevation and non-zero chi-value results from FastScape after 50 Ma and 25 Ma model time. For the purpose of comparison, uniform precipitation rates of 0.2 and 1 m/yr, and uniform uplift rates of 0.00010 m/yr and 0.010 (pulsed) m/yr were used for the Namibia and Himalaya domains, respectively listed below.

Results after 50 Ma of model time in FastScape	**DEM Cell Size (m)**	**Domain Area (10^4 km^2)**	**Initial Elevation (m)**	**Elevation After 50 Ma (m)**	**Average Elevation ± Standard Deviation (m)**	**Range of Non-Zero Chi Values (m)**	**Average Non-Zero Chi Values ± Standard Deviation (m)**
Namibia 4101	~90	13.6	0 - 2543	0 - 2353	1084 ± 613	3 - 78,978	28,828 ± 13,564
Namibia 4101 (results clipped to Namibia 1601 extent)	~90	2.1	587 - 2351	96 - 2337	1300 ± 488	6696 - 78,978	33,628 ± 11,771
Namibia 1601	~90	2.1	587 - 2351	587 - 2595	1672 ± 426	3 - 57,382	12,820 ± 9,513
Namibia ASTER	~30	2.1	567 - 2356	569 - 2412	1343 ± 920	1 - 31,931	10,753 ± 5,515
Himalaya 4101	~90	14.1	58 - 8800	1057 - 6228	2554 ± 1598	3 - 128,699	48,582 ± 21,625
Himalaya 4101 (results clipped to Namibia 1601 extent)	~90	2.2	128 - 8052	1557 - 4098	1583 ± 66	13,554 - 112,611	42,468 ± 13,429
Himalaya 1601	~90	2.2	128 - 8052	128 - 7251	604 ± 504	3 - 58,187	19,780 ± 8,454
Himalaya ASTER	~30	2.2	127 - 7977	127 - 7243	1342 ± 920	1 - 36,587	12,993 ± 5,727
Results after 25 Ma of model time in FastScape							
Namibia 4101	~90	13.6	0 - 2543	0 - 2458	1190 ± 524	4 – 82,961	27,762 ± 14,329
Namibia 4101*	~90	13.6	0 - 2543	0 - 2651	1211 ± 485	4 – 90,925	32,085 ± 13,783
Himalaya 4101	~90	14.1	58 - 8800	1307 - 7092	3161 ± 1918	3 - 122,349	42,123 ± 19,612

Note: * bilinear interpolation of precipitation rate was used in this model. See Table 1 for details.

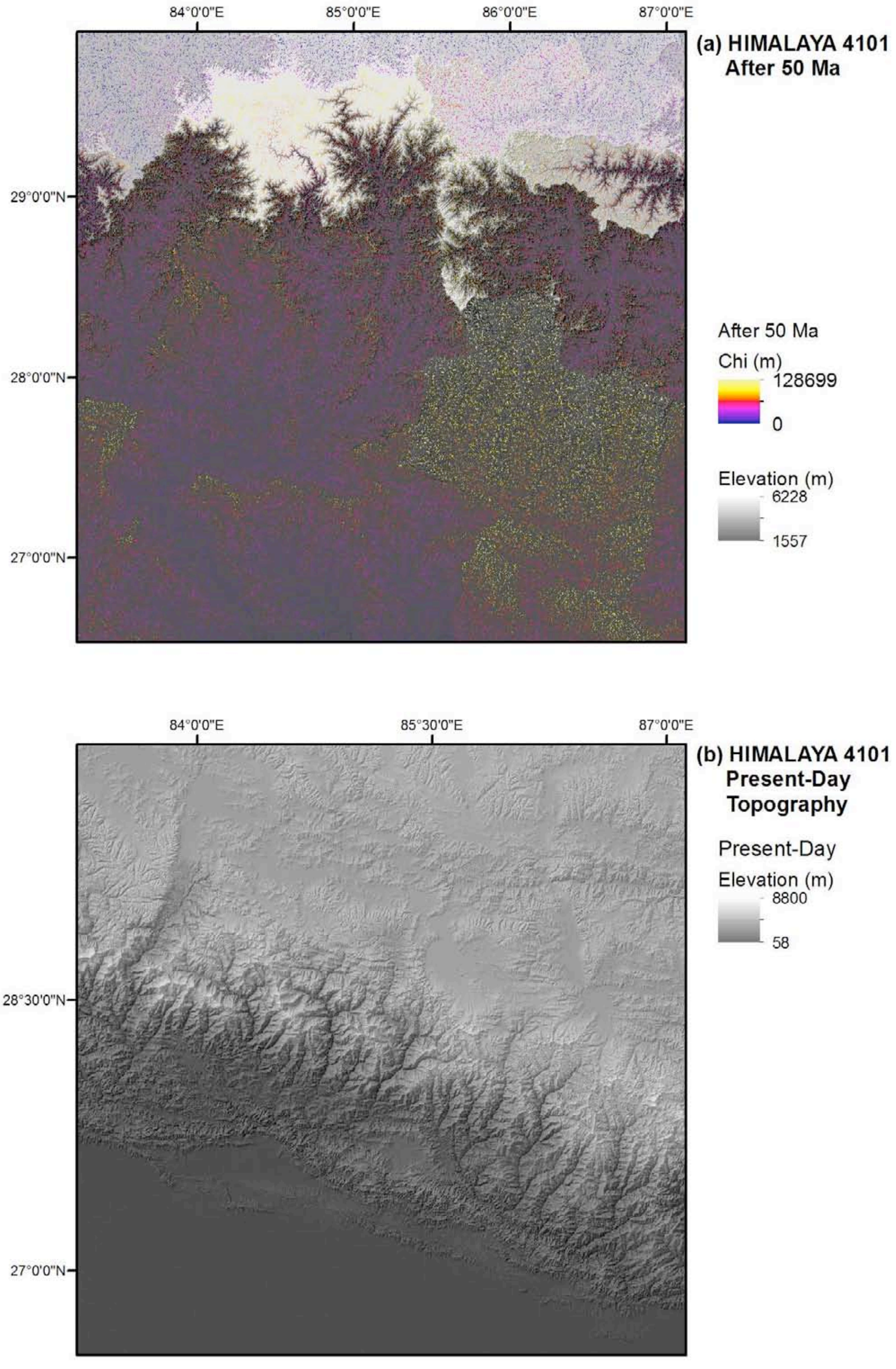

Figure 20. Comparison of topography from a 90-m shaded-relief DEM produced after (a) 50 Ma by FastScape and (b) present-day, shaded-relief topography for the Himalaya 4101 study area. Chi values are also shown overlying the 50 Ma topography. Precipitation and uplift values used in FastScape input (Table 1) are listed.

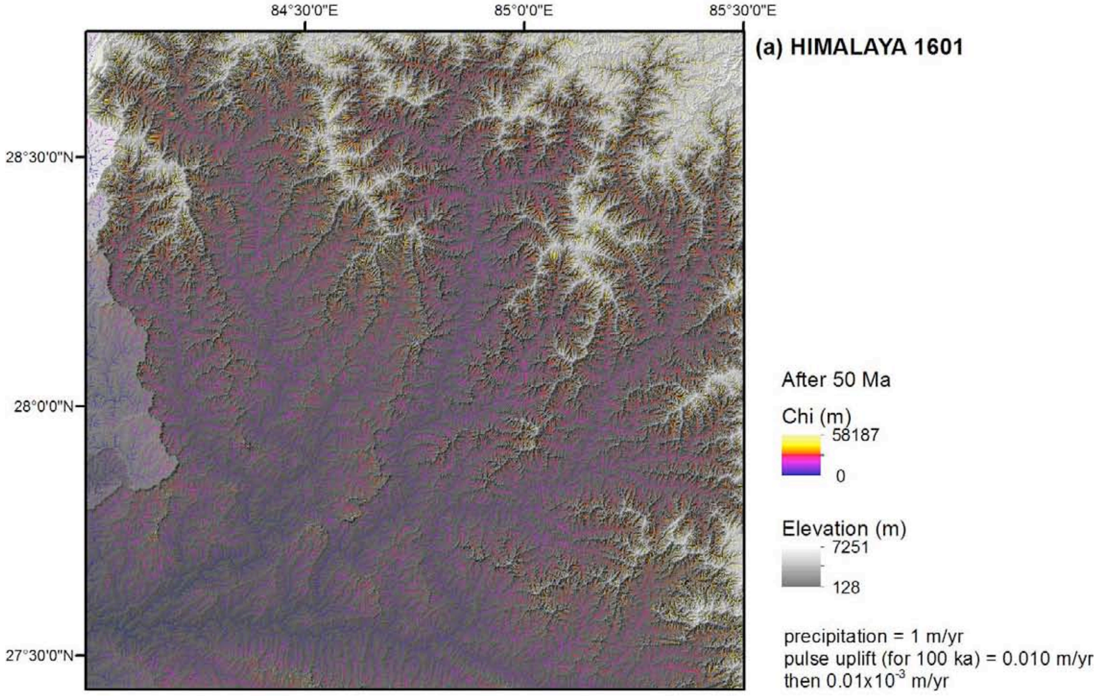

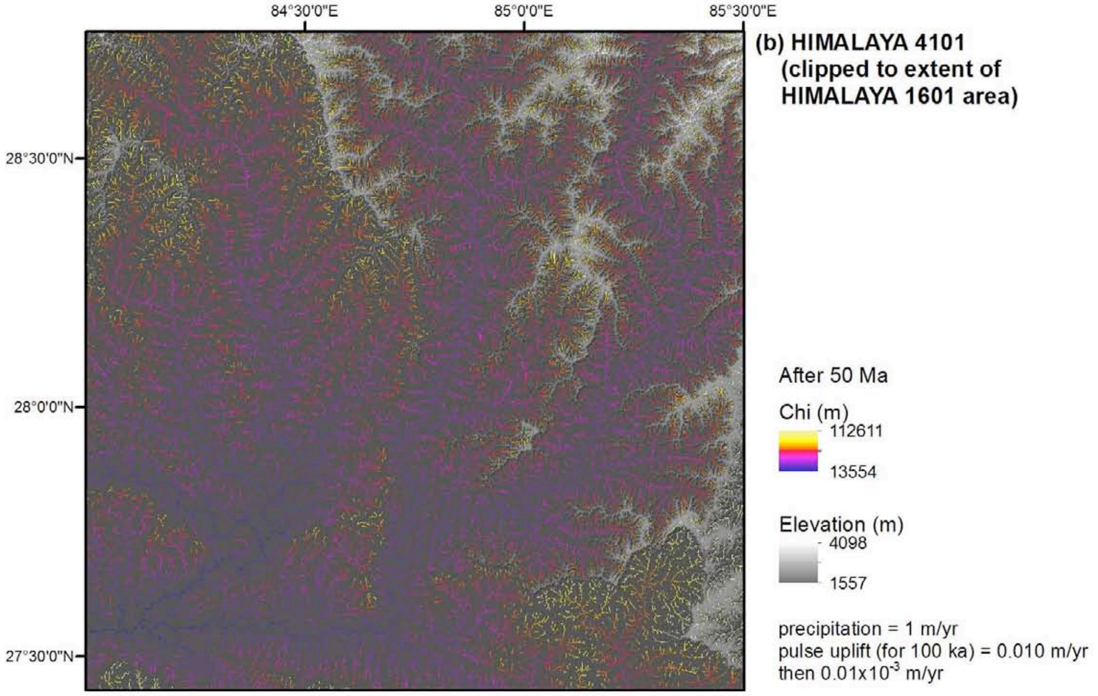

Figure 21. FastScape chi-value and topographic, 90-m shaded-relief DEM results after 50 Ma for the (a) Himalaya 1601 study area compared to (b) results clipped from the Himalaya 4101 domain. Precipitation and uplift values used in FastScape input (Table 1) are listed.

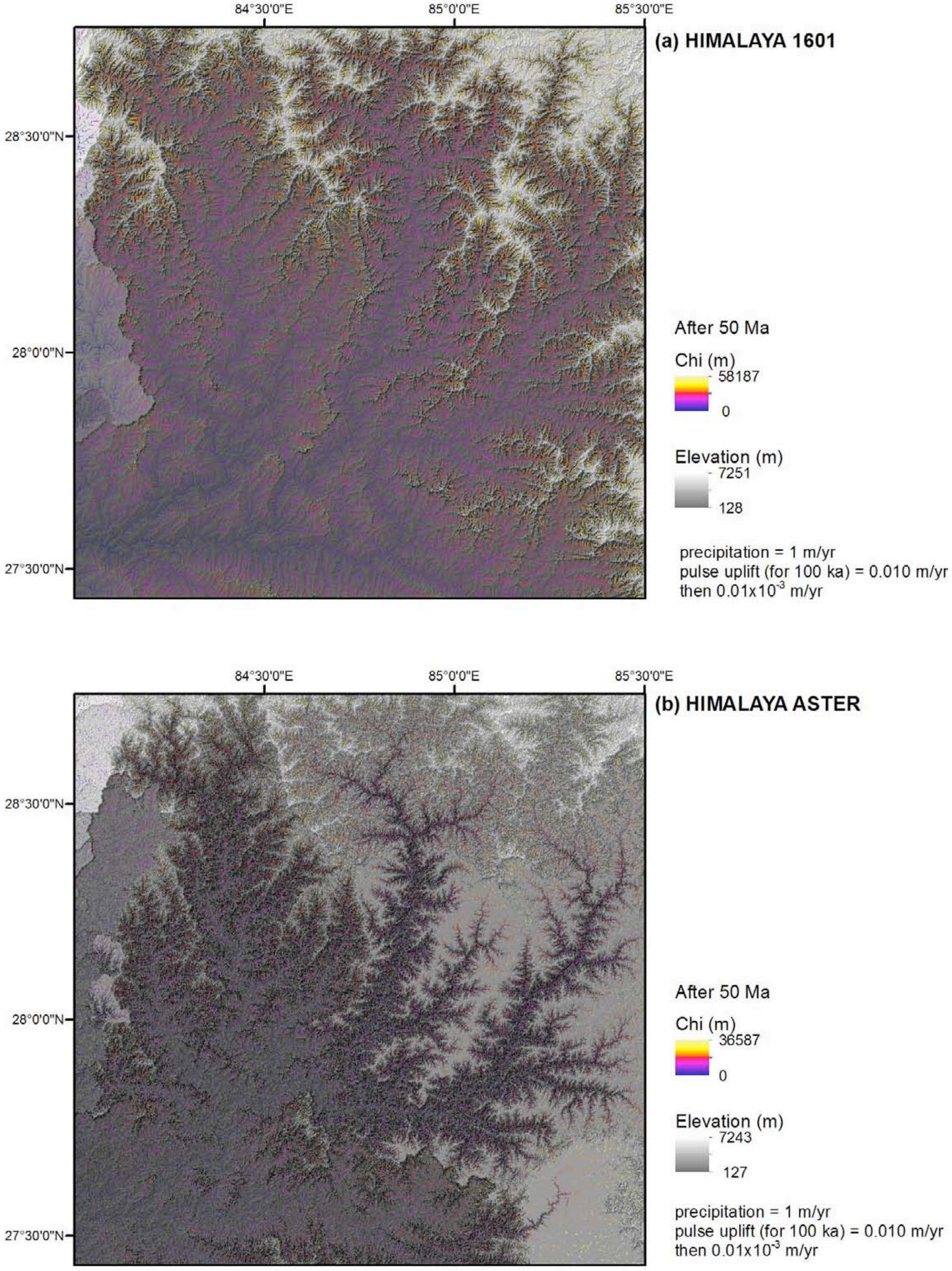

Figure 22. Comparison of FastScape chi values and topography from (a) a 90-m shaded-relief DEM produced after 50 Ma by FastScape for the Himalaya 1601 domain, and (b) a 30-m shaded-relief DEM topography for the Himalaya ASTER domain. Precipitation and uplift values used in FastScape input (Table 1) are listed.

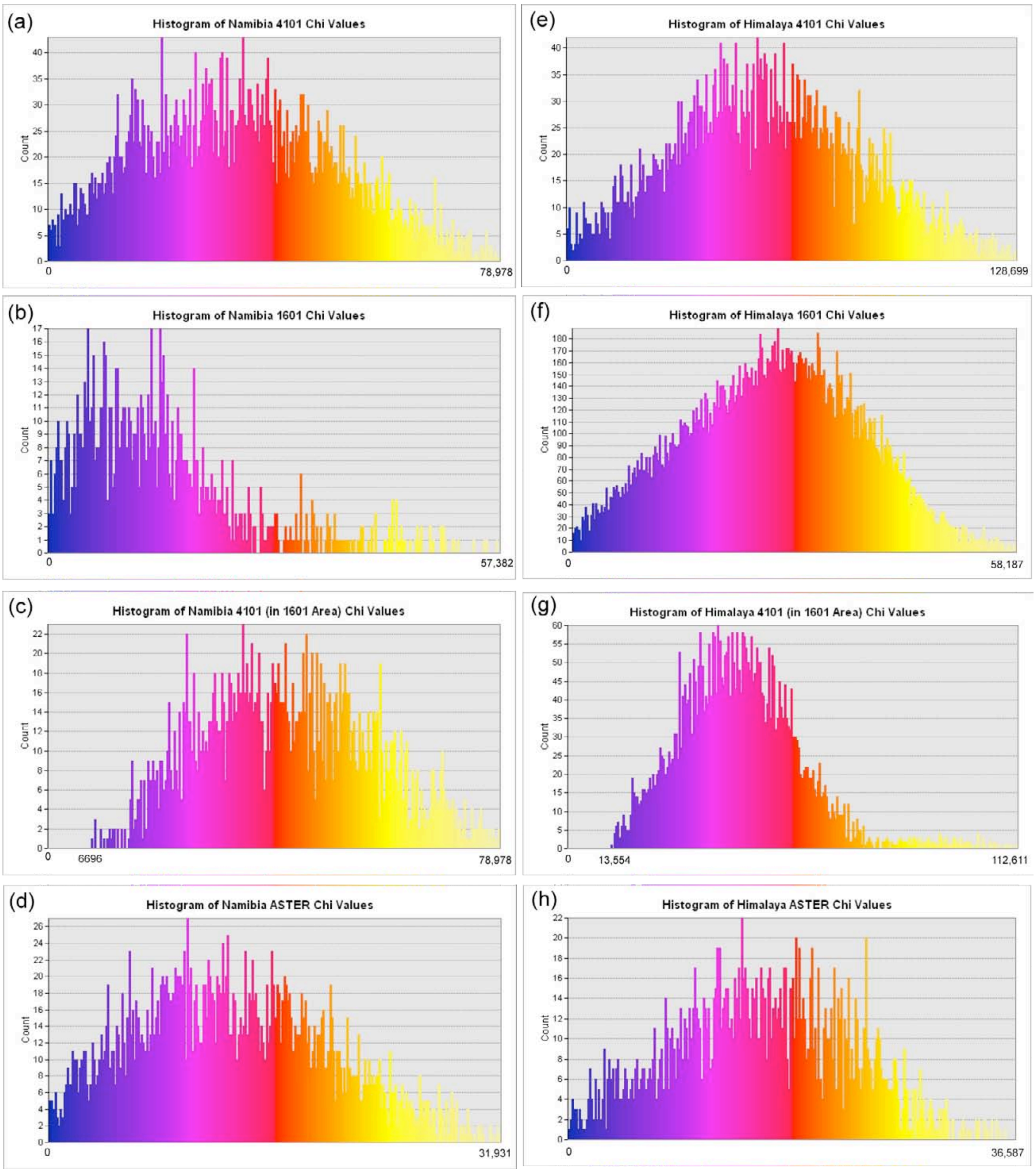

Figure 23. Distribution of FastScape chi values for Namibia and Himalaya domains for a model time of 50 Ma. The chi-value distribution colors are based on the graduated colors used to symbolize chi values in Figures 17 to 22.

5.1.1 Effect of Domain Size on Chi Values

The resampled, clipped Namibia 4101 and Himalaya 4101 FastScape DEMs are shown in Figure 18b and 21b, respectively. Fifty-Ma elevations from the Namibia 1601 DEM were subtracted from the resampled, clipped 50-Ma Namibia 4101 elevations. Likewise, elevations from the 50-Ma Himalaya 1601 DEM were also subtracted from the resampled, clipped 50-Ma Himalaya 4101 elevations. Results are show in Figures 24 and 25.

Shades of blue indicate areas where Namibia 1601 elevations are higher than those of the clipped Namibia 4101 after 50 Ma model time (Figures 18 and 24), and where Himalaya 1601 elevations are higher than those of the clipped Himalaya 4101 (Figures 21 and 25). Shades of orange indicate areas where more erosion and incision has occurred in the clipped Namibia 4101 and clipped Himalaya 4101 domains, resulting in elevations that are lower than those in the Namibia 1601 and Himalaya 1601 domain, respectively. Ninety-nine percent of cells in the Namibia elevation-difference (Figure 24) have a negative elevation difference and 95% of the cells in the central Himalaya elevation-difference raster (Figure 25) have a positive elevation difference. This indicates that the clipped Namibia 4101 area underwent significantly more erosion in 50 Ma than did the same area in the Namibia 1601 domain. Clipped Himalaya 4101 experienced significantly more net uplift than did Himalaya 1601 over the same time period.

The most significant differences in Namibia erosion occur along the Great Escarpment, major river channels, and model boundaries (Figures 18 and 24). Erosional patterns are more dendritic and have more extensive headward erosion into regions of higher elevation on the east side of the clipped Namibia 4101 area, in comparison to erosion in the Namibia 1601 domain (Figure 18). Differences in amounts of erosion in the Namibia domains are likely due to a lower, sea-level base level and greater total drainage areas in the full Namibia 4101 model than in the Namibia 1601 model. After 50 Ma, the clipped Namibia 4101 has a minimum elevation of 96 m, which is 491 m lower than the minimum elevation (e.g., 587 m) in that area before FastScape modeling. The minimum elevation, which is also base level, for Namibia 1601 is the same before and after FastScape modeling (Table 3). Mean elevations of clipped Namibia 4101 and Namibia 1601 are ~1300 m and ~1670 m, respectively.

In contrast, the clipped Himalaya 4101 area shows significantly more uplift over 50 Ma compared to the same area in the Himalaya 1601 domain (Figures 20, 21, and 25). This is corroborated by elevations listed in Table 3. Mean elevations of clipped Himalaya 4101 and Himalaya 1601 are ~1580 m and ~600 m, respectively, after 50 Ma of FastScape modeling.

The clipped Himalaya 4101 region also showed more lateral and vertical erosion than that experienced by the Himalaya 1601 area over 50 Ma of model time (Figure 21). The clipped area shows significantly more modeled erosion of the Greater Himalaya and Tibetan Plateau. The minimum elevation of clipped Himalaya 4101 increased from 128 m to ~1560 m over 50 Ma, even though this domain lost nearly half of its maximum elevation, decreasing from ~8050 m to ~4100 m in that same time. Minimum elevations for before-and-after Himalaya 1601 domains stayed the same, at a base level of 128 m. The maximum elevation only decreased by 800 m (Table 3; Figure 21).

Chi values are significantly different for larger domains (e.g., Namibia 4101 and Himalaya 4101) than for the smaller subset domains (e.g., Namibia 1601 and Himalaya 1601). For the full Namibia 4101 domain, non-zero chi ranges from 3 to ~79,000 m. Non-zero chi values in the clipped Namibia 4101 area range from ~6700 to 79,000 m (Table 3; Figures 18 and 23). Namibia 1601 has non-zero chi values of 3 to ~57,000 m. Similarly, non-zero chi values (~13,000 - 113,000 m) in the clipped Himalaya 4101 area are higher than those for the same area in the Himalaya 1601 domain (3 - ~58,100 m; Table 3; Figures 21 and 23). FastScape analysis indicates that maximum and mean, non-zero chi values are larger for larger domain sizes within given domains in Namibia and in the central Himalaya (Table 3). Himalaya 4101 yielded higher maximum and mean, non-zero chi values than those in the Namibia model at the 50 Ma time step; however, smaller domains yielded very similar maximum chi values of ~57,000 and ~58,000 for both the Namibia 1601 and Himalaya 1601 model domains, respectively, despite their very different uplift and precipitation rates. Mean chi values and their standard deviations are, however, lower for Namibia 1601 (~13,000 ± 10,000 m) than for Himalaya 1601 (~20,000 ± 8,000 m).

Though Namibia 4101 and Himalaya 4101 both have model domains defined by $nx = ny = 4101$, the actual area of those domains are different (Table 3) because of different cell resolutions of input DEMS. Namibia 4101 and Namibia 1601 domains have initial cell sizes of 89.73 m x 89.73 m. Similarly, Himalaya 4101 and Himalaya 1601 domains start with a resolution of 91.66 m x 91.66 m (Table 1). The surface area within the Himalaya 4101 (e.g., ~141,000 km^2) is 4.2% greater than the area within the Namibia 4101 domain (e.g., ~136,000 km^2). Though the mean chi values produced for Himalaya 4101 (~49,000 ± 14,000 m; ± standard deviation) are on average higher than those calculated for the Namibia 4101 domain (~29,000 ± 14,000 m; ± standard deviation), it is likely that they would be more similar, such as chi values in the Namibia 1601 and Himalaya 1601 domains, if the total domain areas were equal.

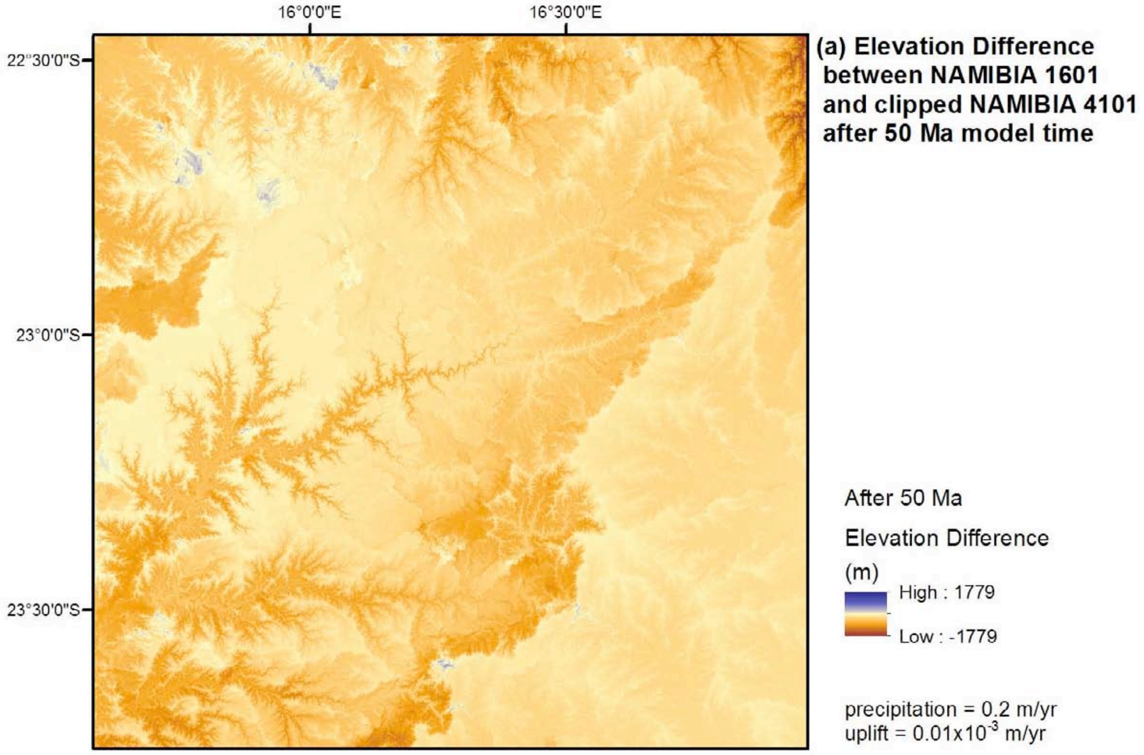

Figure 24. Positive and negative elevation differences between Namibia 1601 and Namibia 4101 for the 1601x1601 domain extent after 25 Ma.

5.1.2 Effects of Cell Size on Chi Values

To examine the effect that grid resolution has on the calculation of chi, FastScape was used to analyze the same domain (e.g., Namibia 1601) but with two different cell sizes. Namibia 1601 and Namibia ASTER cover the same geographic extent in Namibia (Figures 11 and 13) as does Himalaya 1601 and Himalaya ASTER in the central Himalaya (Figures 12 and 13). Namibia 1601 and Himalaya 1601, however, have a coarser resolution (~90-m cell size) than that of Namibia ASTER and Himalaya ASTER (~30-m cell size).

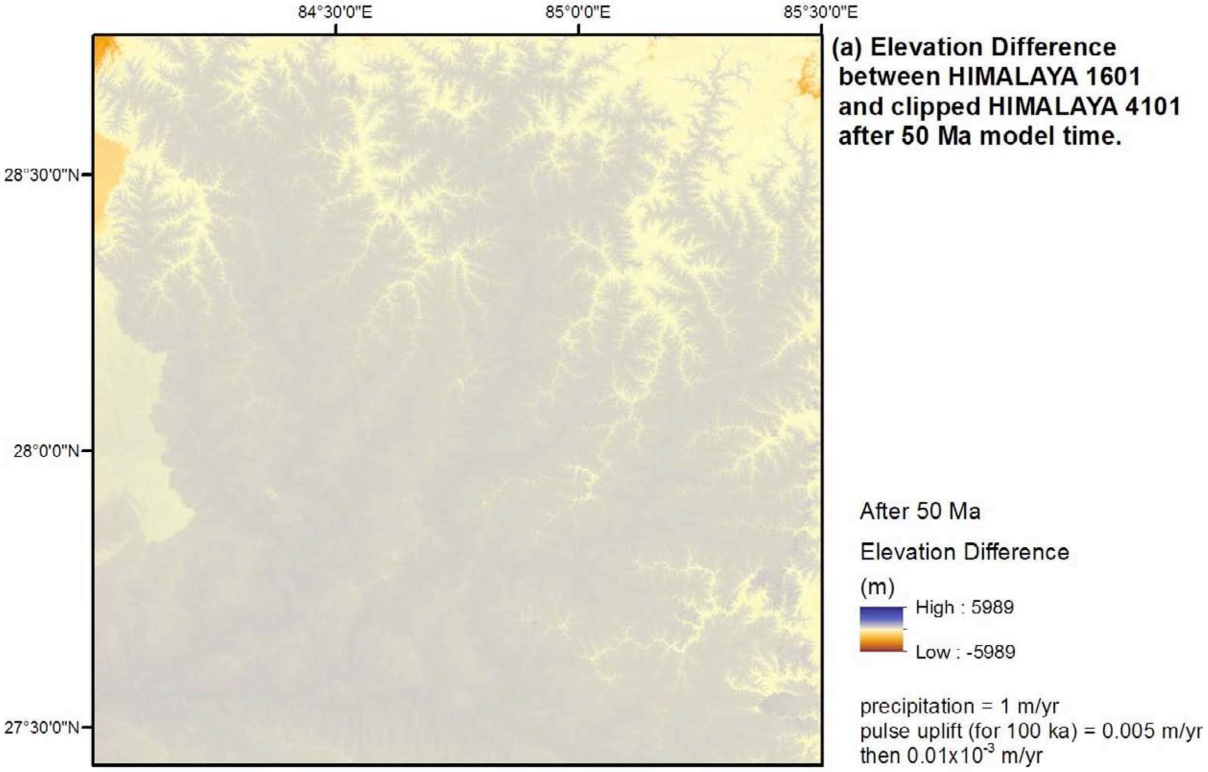

Figure 25. Positive and negative elevation differences between Himalaya 1601 and Himalaya 4101 for the 1601x1601 domain extent after 25 Ma.

After 50 Ma of model time, Namibia 1601 and Namibia ASTER have non-zero chi values that range from 3 to ~57,000 m and 1 to ~32,000 m, respectively. The non-zero chi values resulting from the FastScape analysis of Himalaya 1601 and Himalaya ASTER are 3 to ~58,000 m and 1 to ~37,000 m, respectively. FastScape analysis of finer resolution raster DEMs results in lower chi values than those calculated with a coarser resolution for the same domain. Again, FastScape evolution of the smaller subset domains returned maximum chi values (~32,000 m and ~37,000 m) and mean chi values (~11,000 and ~13,000 m) for Namibia ASTER and Himalaya ASTER that are very similar, despite differences in precipitation and uplift rates. ASTER domains have the same surface area as the Namibia 1601 and Himalaya 1601 domains (~160,000 km^2; Table 3).

Results from FastScape analysis of Namibia 1601 and Namibia ASTER have cell sizes of ~90 m and ~30 m, respectively, as do results from Himalaya 1601 and Himalaya ASTER. Without resampling rasters to a larger or smaller cell size, which adds uncertainty to chi values, a direct pixel-by-pixel comparison of the nature of erosion in the two models cannot be made. Qualitatively, it is shown in Namibia (Figure 19) that erosion is broader in extent, affecting hillslopes as much as stream beds, at the finer 30-m resolution, and erosion appears to be more dendritic and stream-channel incision in nature at the coarser 90-m cell resolution. Conversely, Himalaya erosion appears to be broader in extent at the coarser 90-m cell resolution (Figure 22).

5.1.3 Model Time Effect on Chi Values

As landscape evolves through FastScape modeling, chi values vary with model time and with changes in channel elevations, catchment areas, and channel length (Figures 17, 19, and 26 to 40). Maximum, non-zero chi values for Namibia 4101 (uniform precipitation) decreased from ~83,000 m to ~79,000 m, and mean, non-zero chi values decreased from ~28,000 ± 14,000 m (± standard deviation) to ~29,000 ± 14,000 m (± standard deviation) between 25 Ma and 50 Ma, respectively (Table 3; Figures 17, 26, and 27). Mean elevations and standard deviations for Namibia 4101 are ~1200 ± 500 m and ~1100 ± 600 m at 25 Ma and 50 Ma, respectively. Maximum elevations were ~2400 m and ~2350 at 25 Ma and 50 Ma, respectively.

Maximum and mean, non-zero chi values for Himalaya 4101 increase from ~122,000 m and ~42,000 ± 20,000 m (± standard deviation), respectively, at 25 Ma to ~129,000 m and ~49,000 ± 22,000 m (± standard deviation), respectively, at 50 Ma (Table 3; Figures 19, 32, and 33). Mean elevations and standard deviations for Himalaya 4101 are ~3200 ± 2000 m and ~2600 ± 1600 m at 25 Ma and 50 Ma, respectively. Maximum elevations for this domain at these time steps are ~7100 m and ~6200 m, respectively.

5.2 FastScape Results after 25 Ma (model time)

FastScape analysis of the larger domains, Namibia 4101 and Himalaya 4101, resulted in fully connected stream and chi networks by the 25 Ma time step. The original aim of this study was to compute ‘present-day’ chi values for Namibia 4101 and Himalaya 4101. Because significantly less change occurs in each landscape over 25 Ma compared to change occurring over 50 Ma of model time, the elevation and chi results for the 25 Ma time steps are presented here to compare chi values with basin-wide cosmogenic ^{10}Be erosion rates in the Namibia 4101 and Himalaya 4101 regions.

Chi values are dependent on domain size, thus, it is important to use larger domains so that values across a region can be directly compared to assess relative states of dynamic equilibrium or disequilibrium within a model domain. The computer available for this study was not able to allocate enough memory for FastScape evolution of ASTER GDEMs for the 4101-cell x 4101-cell domain size, thus only 25Ma FastScape results for Namibia 4101 (90-m cell size) and Himalaya 4101 (90-m cell size) are presented here. The finer resolution was more resource intensive. FastScape elevation results after 25 Ma for Namibia 4101 and Himalaya 4101 were resampled using the nearest-neighbor technique to set the cell sizes to those of the original DEMs. Present-day topography was subtracted from these resampled rasters to visualize the changes in landscape over 25 Ma of model time.

The precipitation rate for the Namibia 4101 model was adjusted to correspond more closely to arid conditions (0.05 m/yr) on the Namibian coast and wetter conditions (0.25 to 0.45 m/yr) on the highlands inland of the Great Escarpment (Table 1; Bierman and Caffee, 2001). FastScape creates a bilinear interpolation of these rates across the domain (Braun, 2013). Figures 26 to 31 illustrate differences in elevation between present-day topography and 25-Ma FastScape topographies in Namibia 4101, as well as chi values at the 25-Ma time step. Table 4 lists chi values and cosmogenic ^{10}Be erosion rates of present-day basins within the Omaruru, Swakop, and Gaub River catchments in the Namibia 4101 domain (90-m cell size).

Shades of blue in Figure 28 indicate areas where positive net elevation gain has occurred over 25 Ma of FastScape model time. Shades of orange to red indicate areas more affected by erosion and with a net loss of elevation. Cell values in the Namibia 4101 elevation-difference raster range from -1205 m to 251 m with a mean elevation difference and standard deviation of 103 ± 132 m. Eighty-three percent of cells in the raster have an elevation gain (Figure 28). Ninety-eight percent of cells with negative elevation differences have values greater than -500 m. The scale for Figures 28 to 31 were set to a range of -500 m to +500 m to most clearly visualize the positive and negative elevation differences between FastScape topographic results at 25 Ma and present-day topography for Namibia 4101. Shades of blues and oranges were otherwise too pale to see clearly, using a scale of -1205 m to +1205 m.

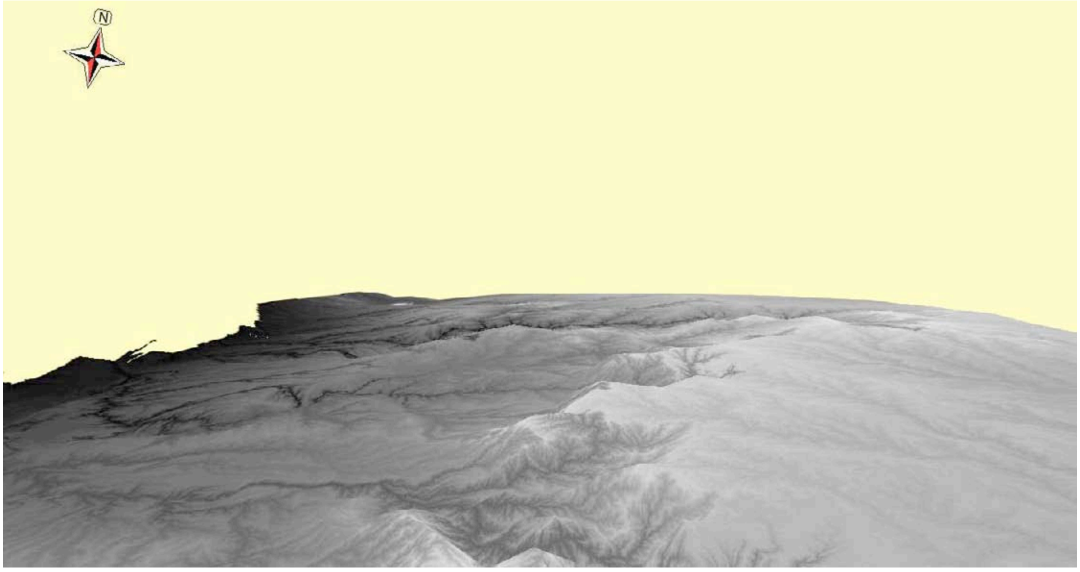

Figure 26. An oblique ArcGlobe view of a FastScape results for Namibia 4101 after 25 Ma of model time. The elevation scale (0 to 2651 m) and scale colors are the same as those in Figure 27a. A vertical exaggeration of 7 is used to demonstrate the steep transition topography that occurs at the Great Escarpment. ArcGlobe does not display scales or legends. ArcGlobe does not display scales or legends.

The maximum, non-zero chi value and maximum elevation for Namibia 4101 using a bilinear interpolation of precipitation rates is ~91,000 and ~2650 m, respectively, at the 25 Ma time step. These values are higher of than those for Namibia 4101 (uniform precipitation) at 25 Ma (~83,000 m and ~2400 m, respectively) when a uniform precipitation rate was used in FastScape. Mean elevations (± standard deviations) for both precipitation-rate models are ~1200 ± 500 m at the 25-Ma time step. The mean, non-zero chi value resulting from the bilinear rate is ~32,000 ± 14,000 m (± standard deviation). Uniform precipitation resulted in a lower mean chi value (~29,000 ± 14,000 m; ± standard deviation) for Namibia 4101 at the 25-Ma time step (Table 3). Lower precipitation rates lead to a decrease in erosion in FastScape modeling, which allows higher landforms to persist, even with slow uplift rates. When the uniform precipitation rate of 0.2 m/yr was used across the Namibia 4101 domain, erosion was stronger, causing subsequent lowering of elevation, and thus a lower maximum chi value for that domain model.

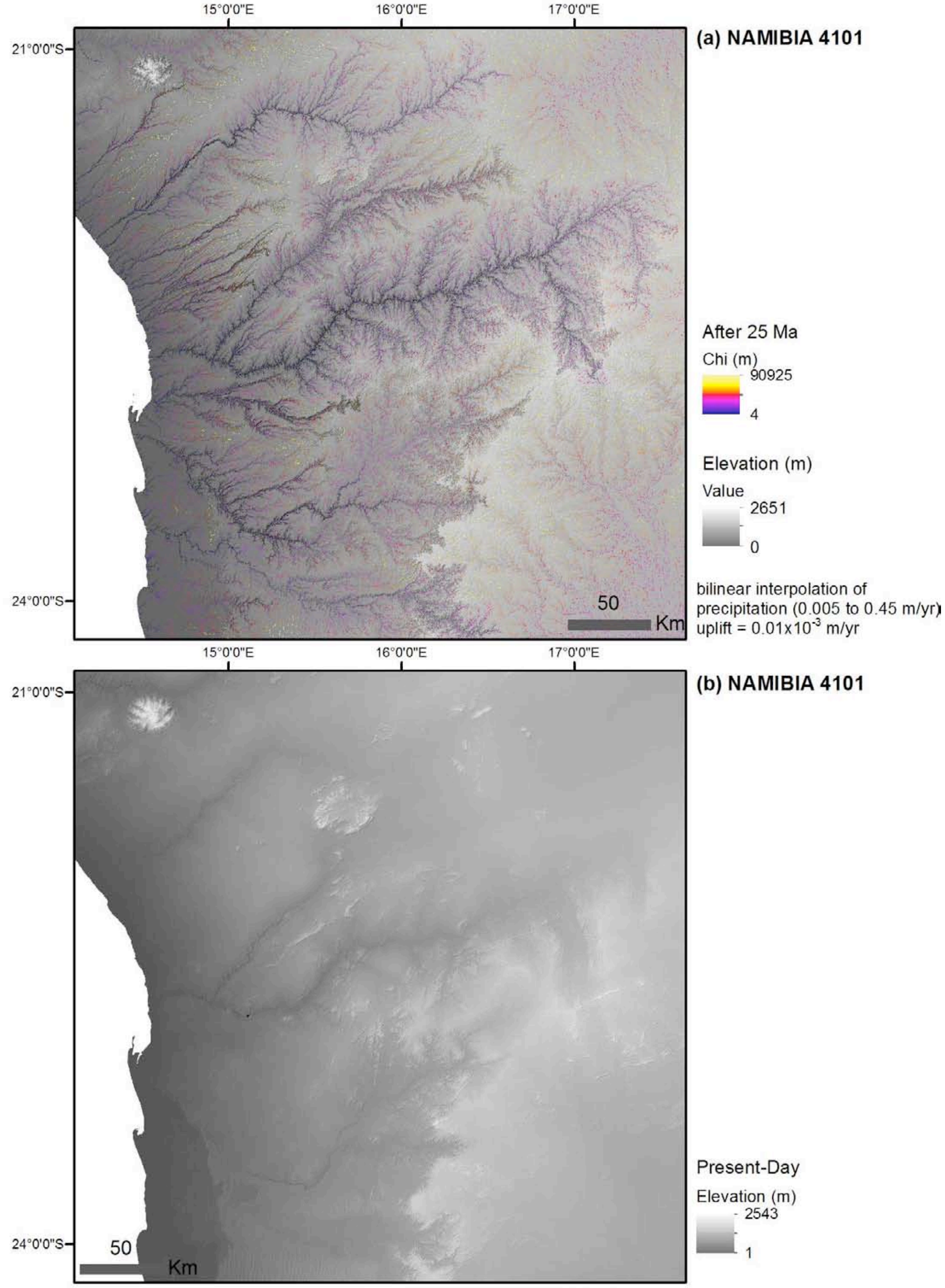

Figure 27. Comparison of topography from a (a) 90-m shaded-relief DEM produced after 25 Ma by FastScape and (b) present-day shaded-relief topography for the Namibia 4101 study area. Chi values are also shown overlying the 25 Ma topography. Bilinear interpolation of four different precipitation values is used along with a uniform uplift rate in FastScape input (Table 1).

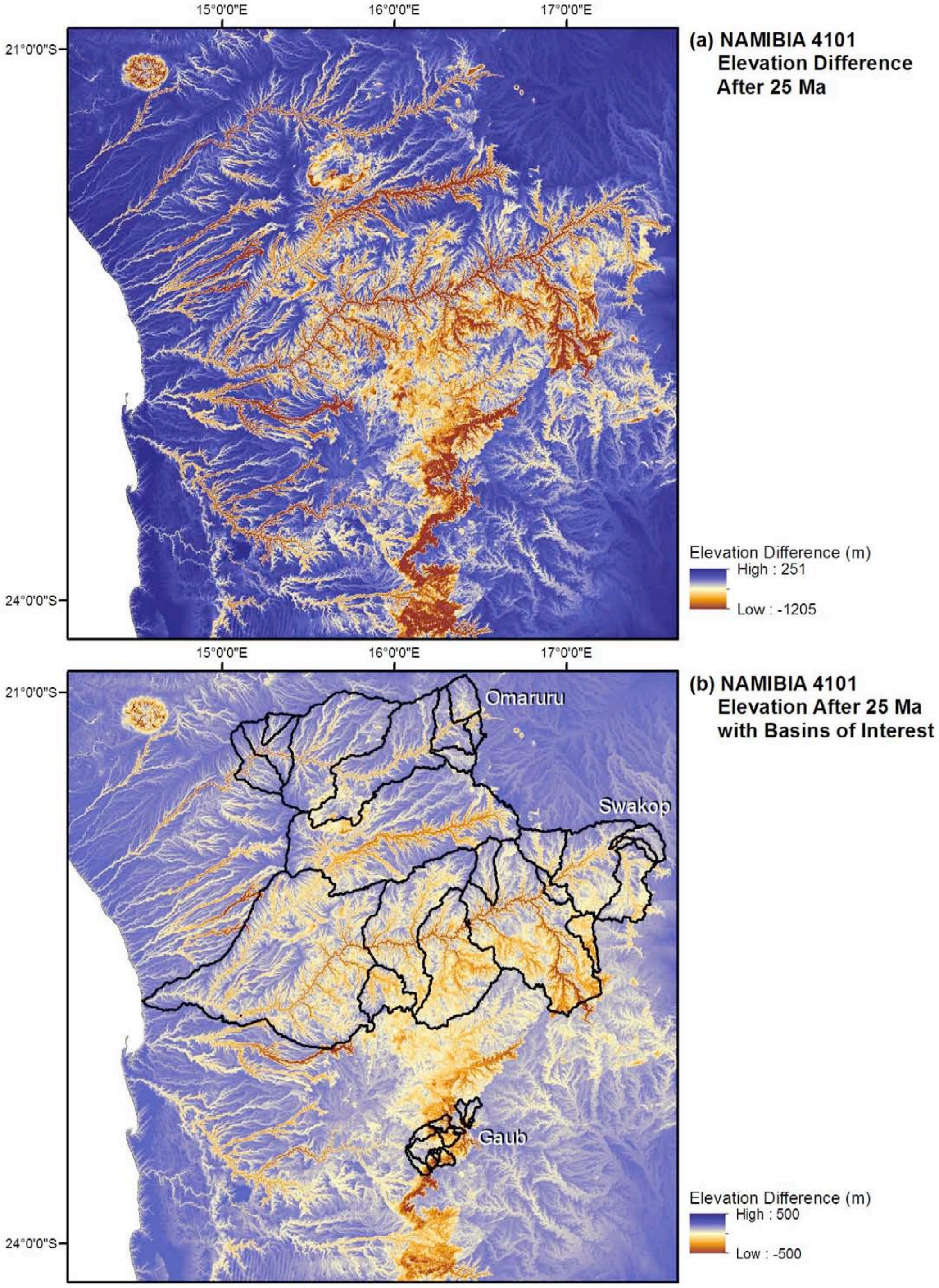

Figure 28. Positive and negative elevation differences (a) between Namibia 4101 after 25 Ma and present-day Namibia 4101 topography. The same elevation differences are (b) shown with basins in the Omaruru, Swakop, and Gaub River catchments. Basins of interest are based on present-day topography.

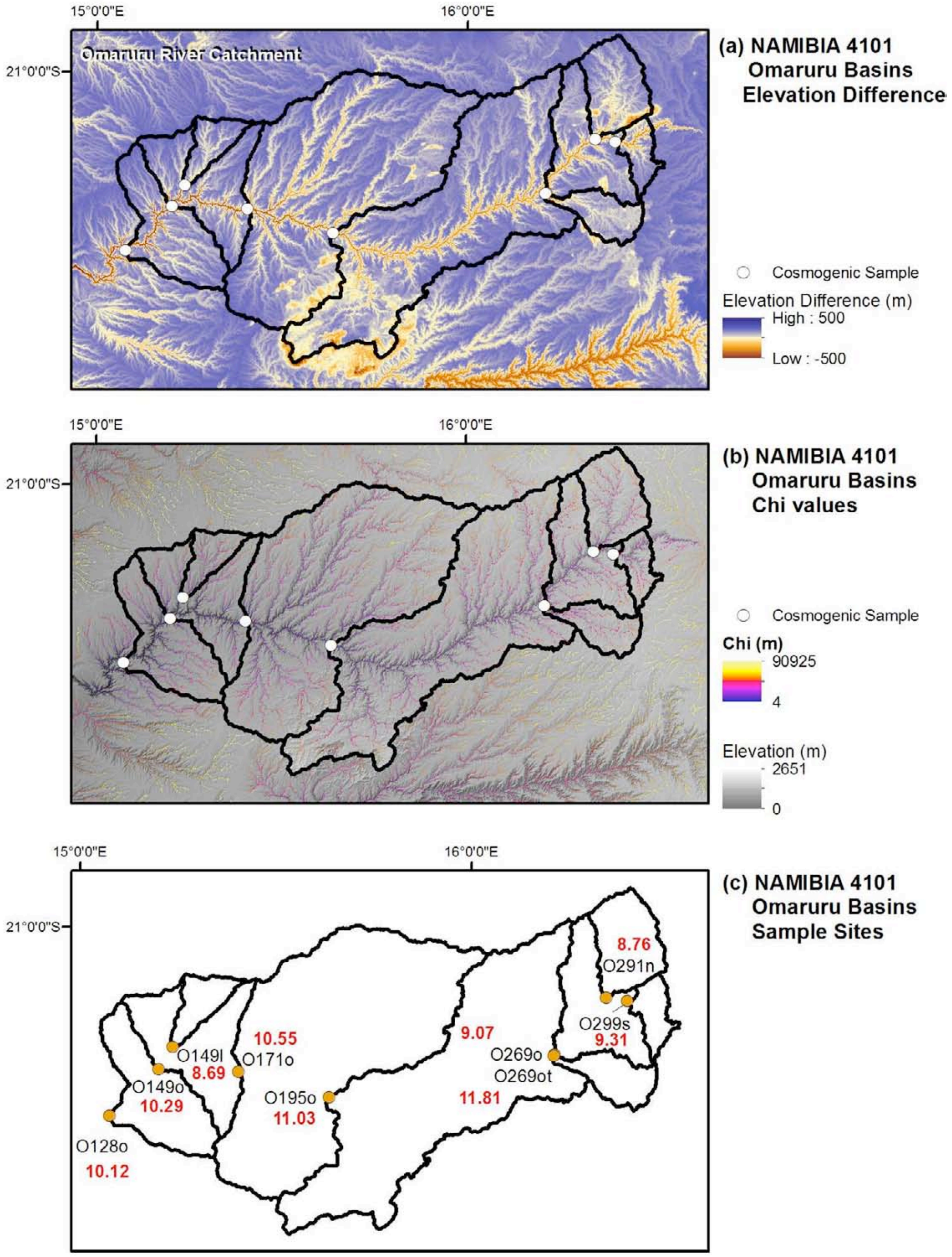

Figure 29. Positive and negative elevation differences (a) between Namibia 4101 after 25 Ma and present-day Namibia 4101 topography for the Omaruru River catchment, with (b) associated FastScape chi values and (c) associated basins. White circles indicate cosmogenic ^{10}Be sample sites. Erosion rates (m/Ma) are in red.

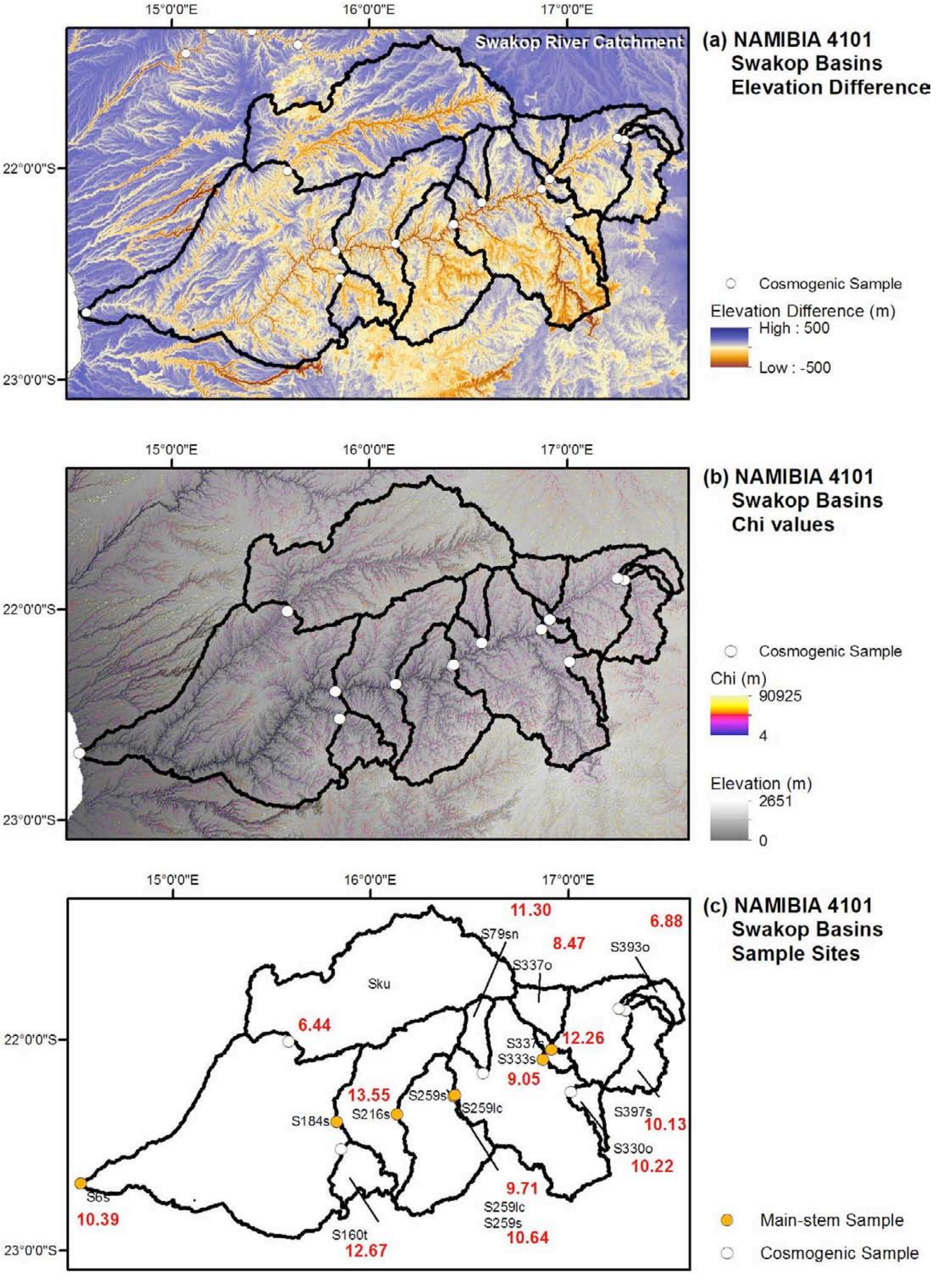

Figure 30. Positive and negative elevation differences (a) between Namibia 4101 after 25 Ma and present-day Namibia 4101 topography for the Swakop River basins, and (b) associated FastScape chi values.

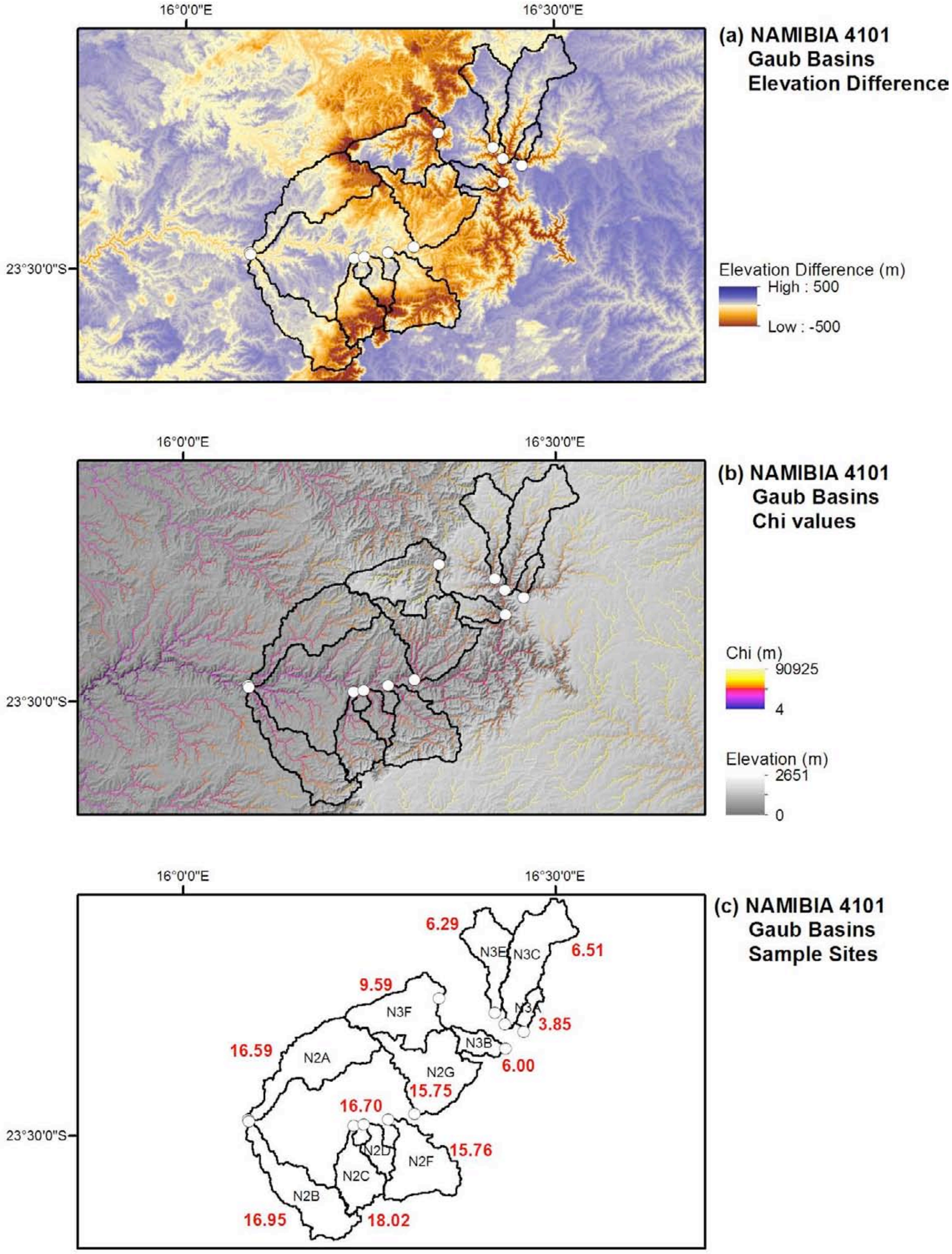

Figure 31. Positive and negative elevation differences (a) between Namibia 4101 after 25 Ma and present-day Namibia 4101 topography for the Gaub River basins, and (b) associated FastScape chi values.

Differences in elevation between present-day topography and the 25-Ma FastScape topography in Himalaya 4101, as well as chi values at the 25-Ma time step are shown in Figures 32 to 40. Table 5 lists chi values and cosmogenic ^{10}Be erosion rates of present-day basins within the Marsyangdi, Bhudi-Gandaki, Trishuli, Bhote Koshi, and Tama Koshi catchments within the larger Himalaya 4101 domain (90-m cell size). Uniform precipitation and uplift rates of 1 m/yr and 0.01 m/yr were used for results presented at the 25 Ma time step for the Himalaya 4101 domain (Figures 32, 33 and 34).

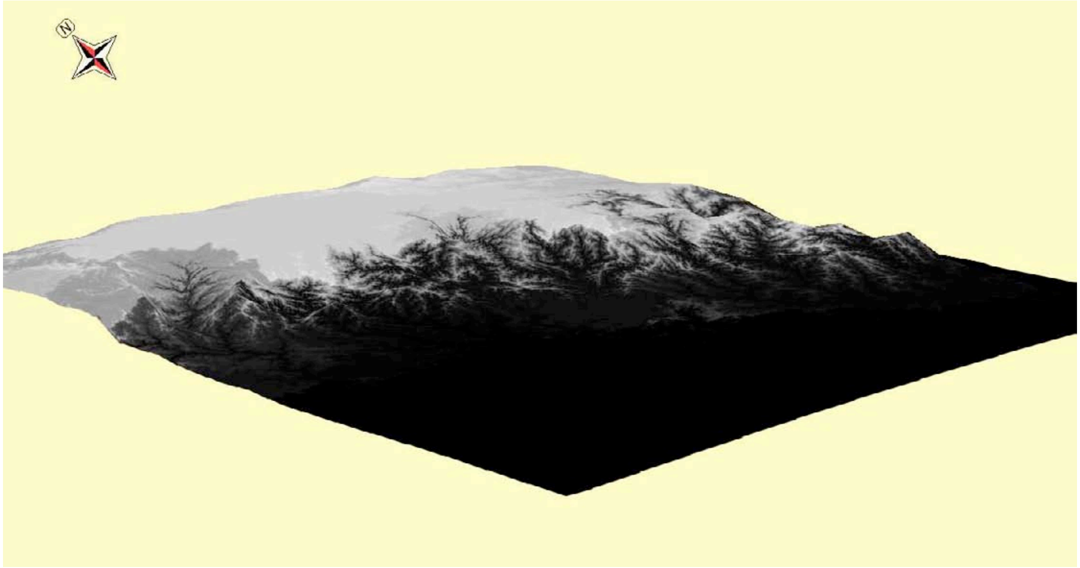

Figure 32. An oblique ArcGlobe view of a FastScape results for Himalaya 4101 after 25 Ma of model time. The elevation scale (1307 m to 7092 m) and scale colors are the same as those in Figure 33a. A vertical exaggeration of 5 is used. ArcGlobe does not display scales or legends.

Shades of blue in Figure 35 indicate areas where positive net elevation gain has occurred over 25 Ma of FastScape model time. Shades of orange to red indicate areas that are more affected by erosion and have a net loss of elevation. Cell values in the Himalaya 4101 elevation-difference raster range from -1250 m to 6310 m, with a mean elevation difference and standard deviation of -110 ± 1178 m. Thirty-three percent of cells in the raster have a negative elevation difference (Figure 35a). The scales in Figure 35 to 38 were adjusted to a range of -6310 m to +6310 m, in order to best visualize the net positive and negative elevation changes that occurred during FastScape modeling over 25 Ma in Himalaya 4101. A mean elevation difference of 2389 ± 6280 m is calculated this elevation range.

Non-zero chi values for Himalaya 4101 at 25 Ma range from 3 to ~122,000 m with a corresponding elevation range of ~1300 to ~7100 m, respectively. Mean elevation (± standard deviation) increased from 3100 ± 2200 to 3200 ± 1900 m between present-day and 25-Ma time-step topographies. Original elevations before FastScape evolution of the landscape ranged from ~60 to ~8800 m. This indicates there was substantial uplift in the Himalaya domain accompanied by erosion of higher landforms, and thus, significant loss of higher elevations.

5.3 Chi Values and ^{10}Be Erosion Rates

A true test of the chi-erosion-rate hypotheses presented at the end of Chapter 2 would include chi values calculated for present-day topography, as ^{10}Be erosion-rate samples were collected from present-day river basins. During this study, however, it was not possible to calculate chi values for the present-day, because FastScape did not remove local minima and create fully connected stream networks until after $\geq$ 25 Ma of model time. It is important to note, however, that Namibian ^{10}Be erosion rates are integrated over timescales ranging from 10^3 to 10^6 years ago until the present-day (Bierman and Nichols, 2004), and it is likely that basin geometries have changed over the past 10^5 to 10^6 years in both Namibia and the Himalaya. Cosmogenic ^{10}Be concentrations in Himalaya stream sediment measure catchment-scale erosion rates integrated over the past the 10^2 – 10^3 years (von Blanckenburg, 2005; Godard et al., 2014). In general, the slow uplift and low precipitation values (bilinear precipitation values; Table 1) used to mimic present-day climate in the Namibia 4101model resulted in slow erosion, such that basin geometry did not change drastically from today's geometry to basin geometry 25 million model years into the future. FastScape modeling of Himalaya 4101, on the other hand, resulted in significant changes to basin geometries.

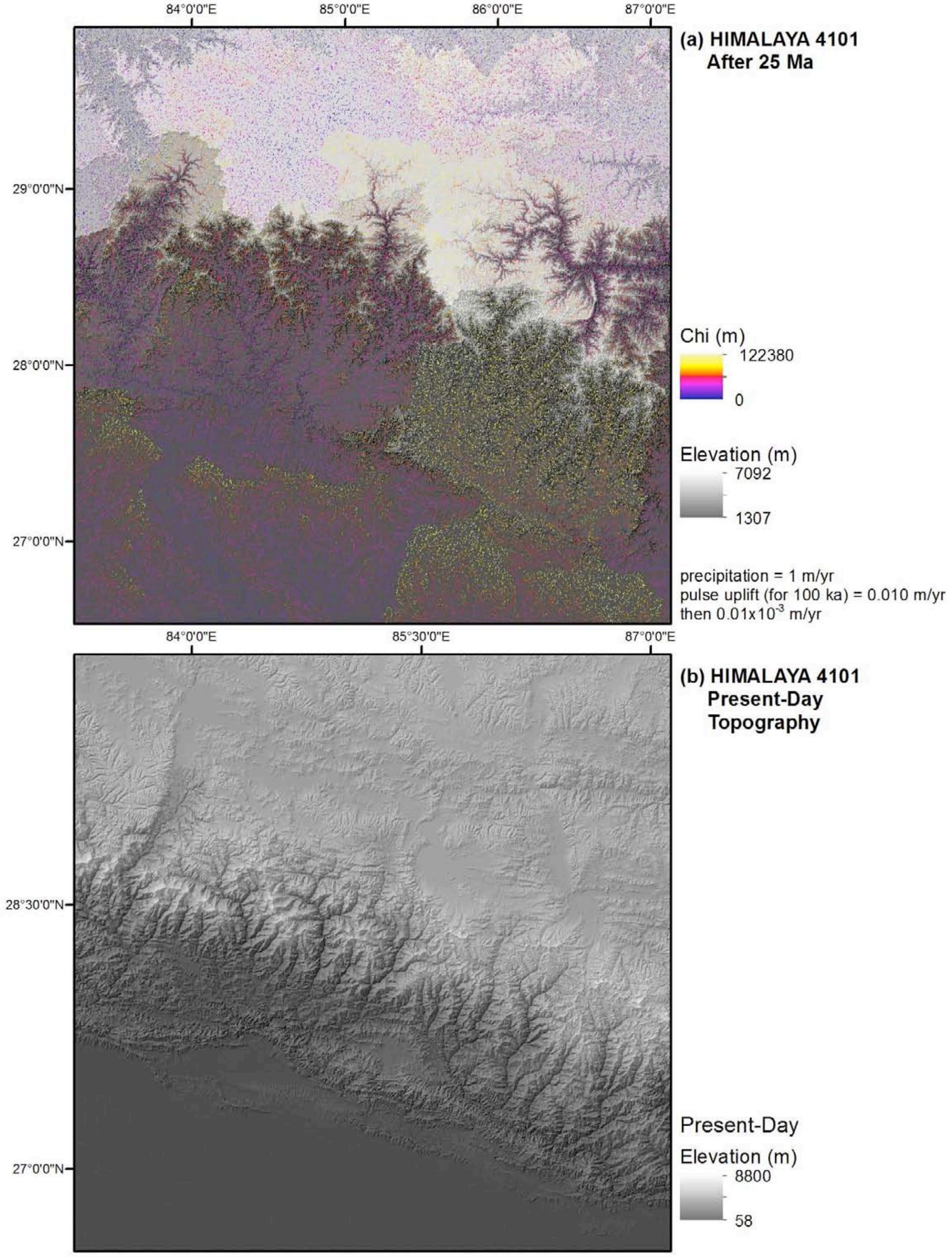

Figure 33. Comparison of topography from a (a) 90-m shaded-relief DEM produced after 25 Ma by FastScape and (b) present-day shaded-relief topography for the Himalaya 4101 study area. Chi values are also shown for the 25 Ma topography. Precipitation and uplift rates used in FastScape input (Table 1) are listed.

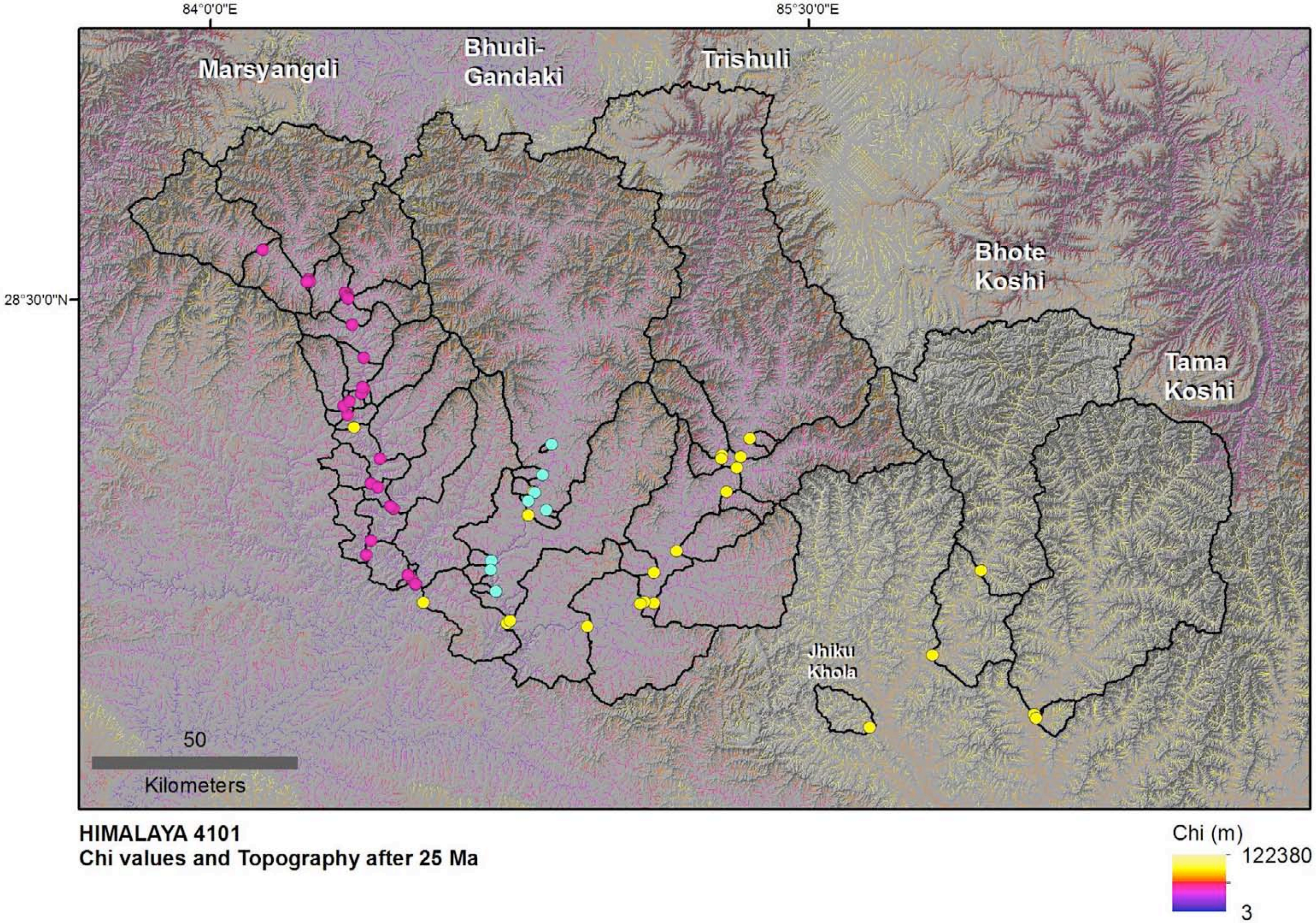

Figure 36. FastScape chi values and shaded-relief DEM after 25 Ma of model time in the Himalaya 4101 domain. Yellow, magenta, and blue circles indicate positions of ^{10}Be samples sites and associated drainage basins (black lines) in the Marsyangdi, Bhudi Gandaki, Trishuli, Bhote Koshi, and Tama Koshi catchments from Andermann (2011), Godard et al. (2012), and Wobus et al. (2005), respectively

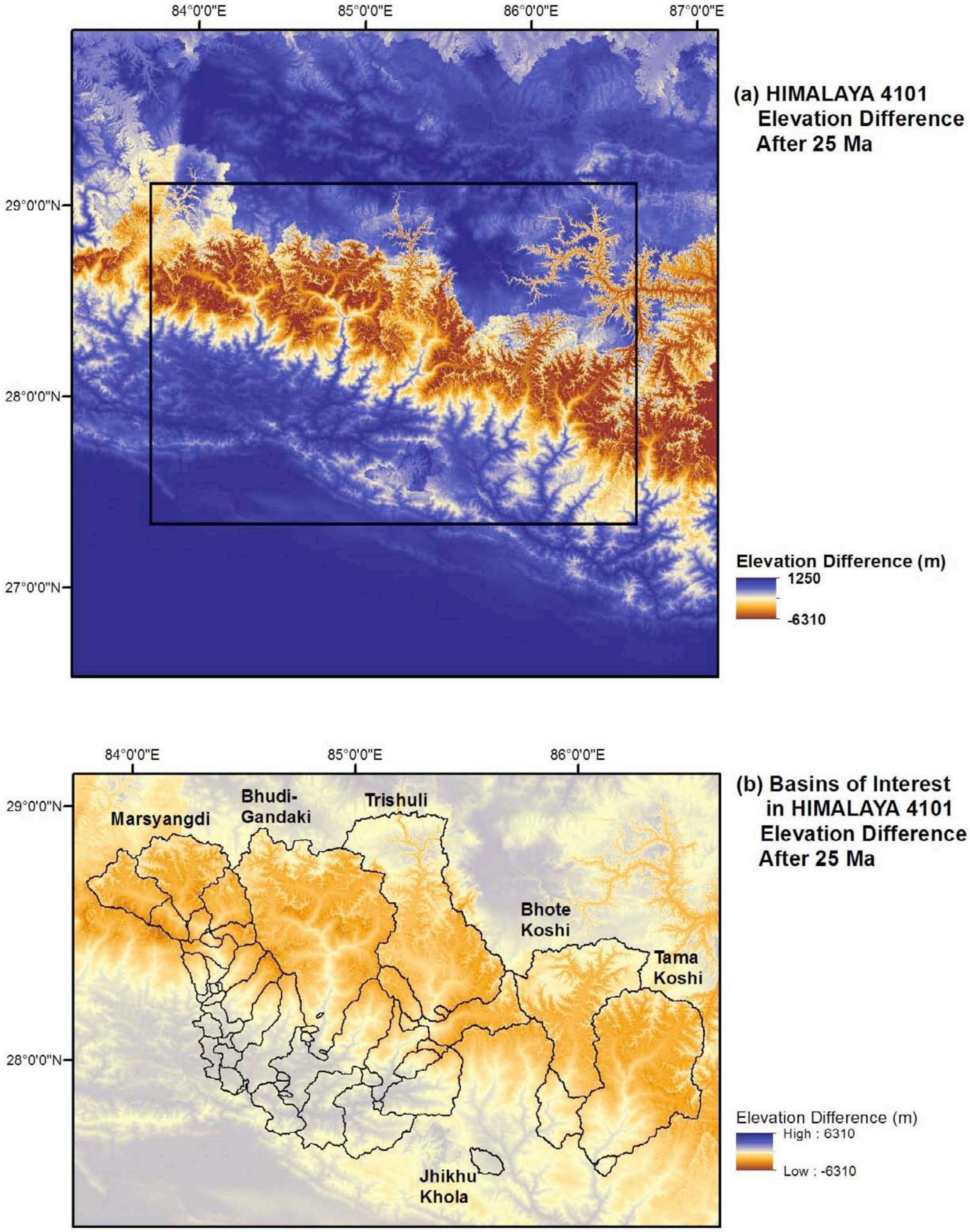

Figure 35. Positive and negative elevation differences (a) between Himalaya 4101 after 25 Ma and present-day Himalaya 4101 topography, and (b) same elevation difference shown with basins in the Marsyangdi, Bhudi Gandaki, Trishuli, Bhote Koshi, and Tama Koshi catchments. Basins of interest are based on present-day topography. The scale represents the elevation difference in both maps.

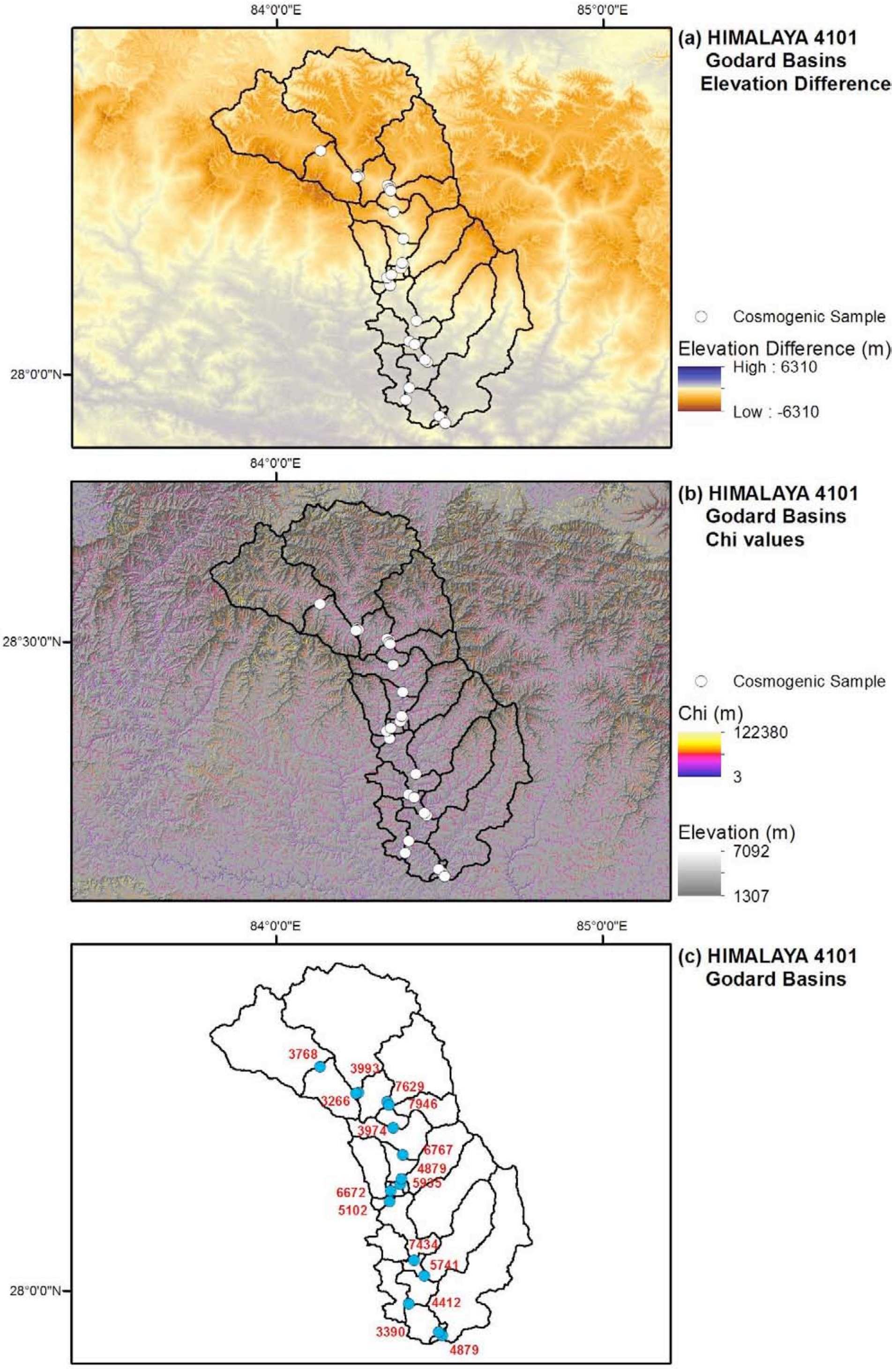

Figure 36. Positive and negative elevation differences (a) between Himalaya 4101 after 25 Ma and present-day Himalaya 4101 topography for the Marsyangdi River basins from Godard et al. (2012), and (b) associated FastScape chi values. White circles indicate cosmogenic ^{10}Be sample sites. (c) Erosion rates (m/Ma) (in red) are shown for main-stem basins. Sample numbers were too long to include in the figure, and can be found in Table 5.

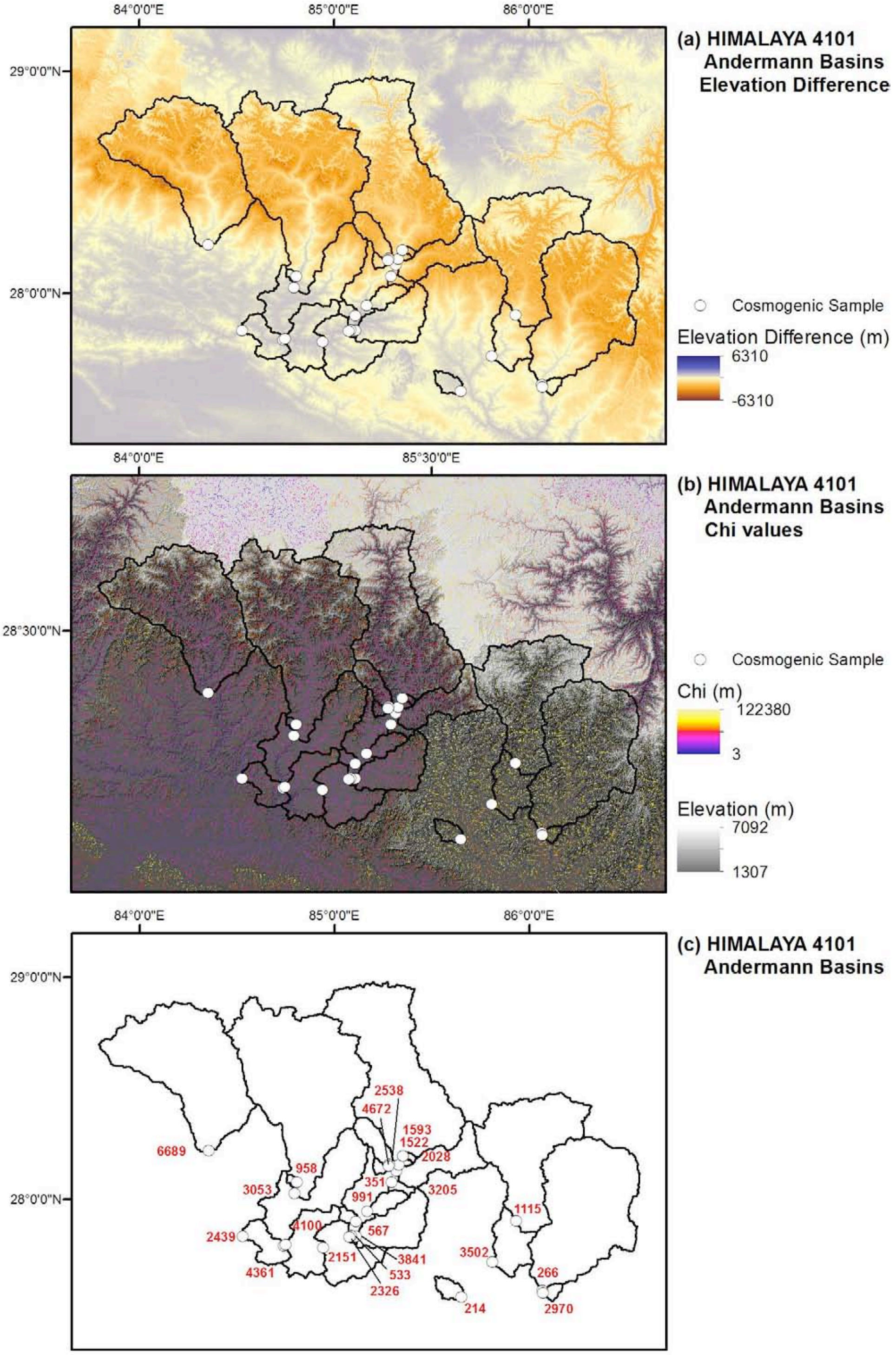

Figure 37. Positive and negative elevation differences (a) between Himalaya 4101 after 25 Ma and present-day Himalaya 4101 topography for the various basins sampled by (Godard et al., 2012), and (b) associated FastScape chi values. White circles indicate cosmogenic ^{10}Be sample sites. (c) Erosion rates (m/Ma) are shown in red. Sample numbers were too long to include in the figure, and can be found in Table 5.

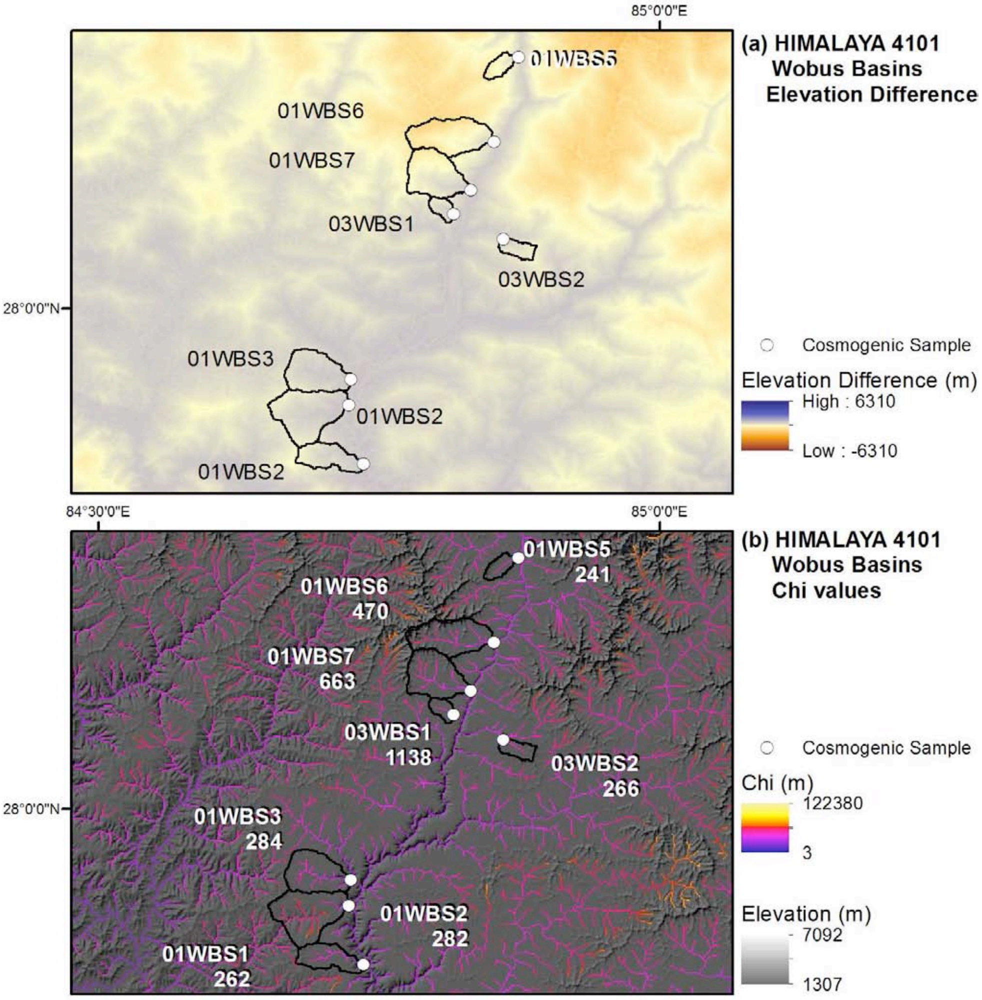

Figure 38. Positive and negative elevation differences (a) between Himalaya 4101 after 25 Ma and present-day Himalaya 4101 topography for the Bhudi Gandaki River basins from Wobus et al. (2005), and (b) associated FastScape chi values. White circles indicate cosmogenic ^{10}Be sample sites. White text list sample numbers and associated ^{10}Be erosion rates.

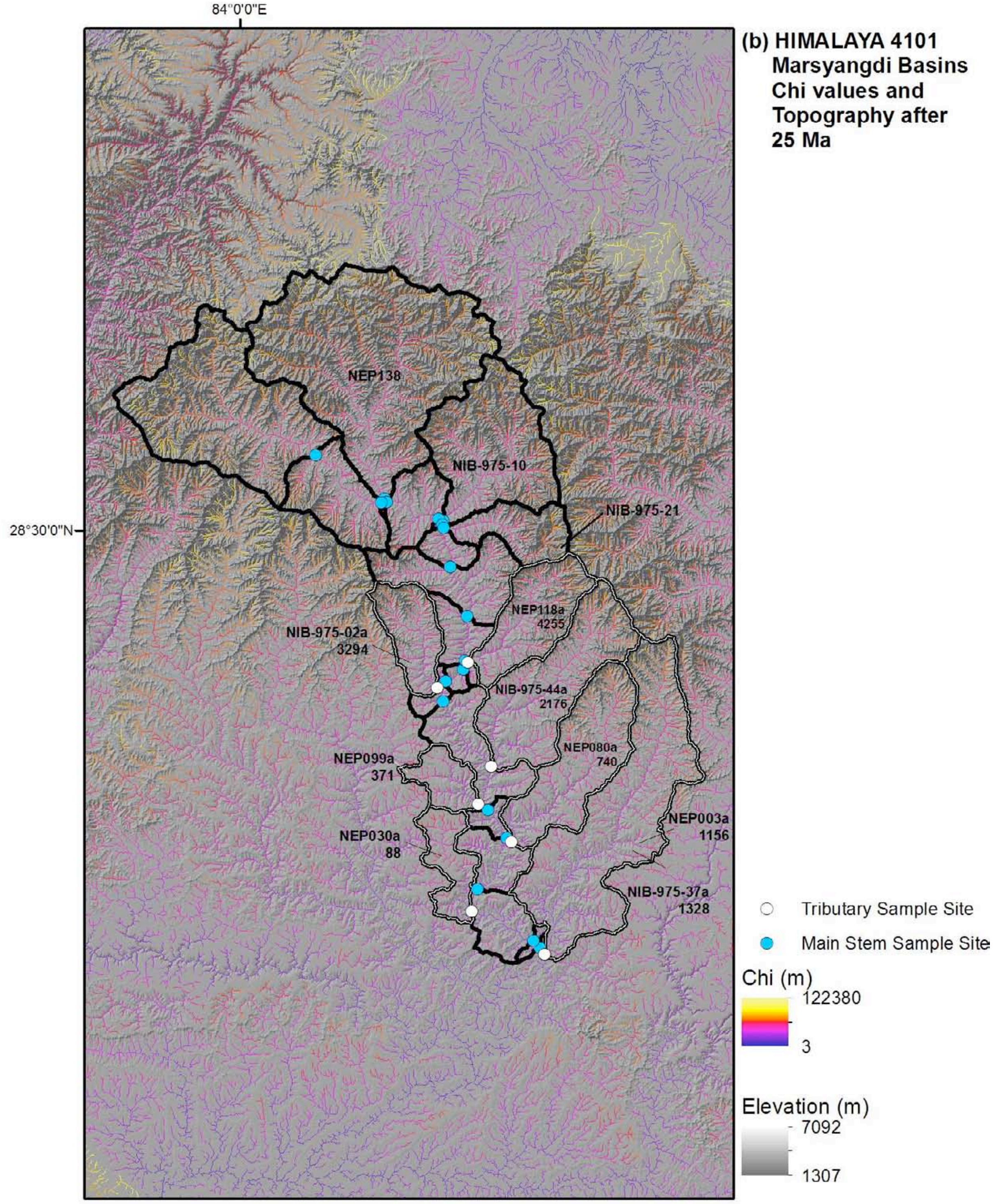

Figure 39. Shaded-relief DEM and chi values for Himalaya 4101 after 25 Ma in the Marsyangdi River basins from Godard et al. (2012). Blue circles and white circles indicate cosmogenic ^{10}Be sample sites from glaciated main stem river basins (black outlines) and unglaciated tributary basins (white in black outlines), respectively. White text list sample numbers and associated ^{10}Be erosion rates. Rates for main-stem samples are shown in Figure 36.

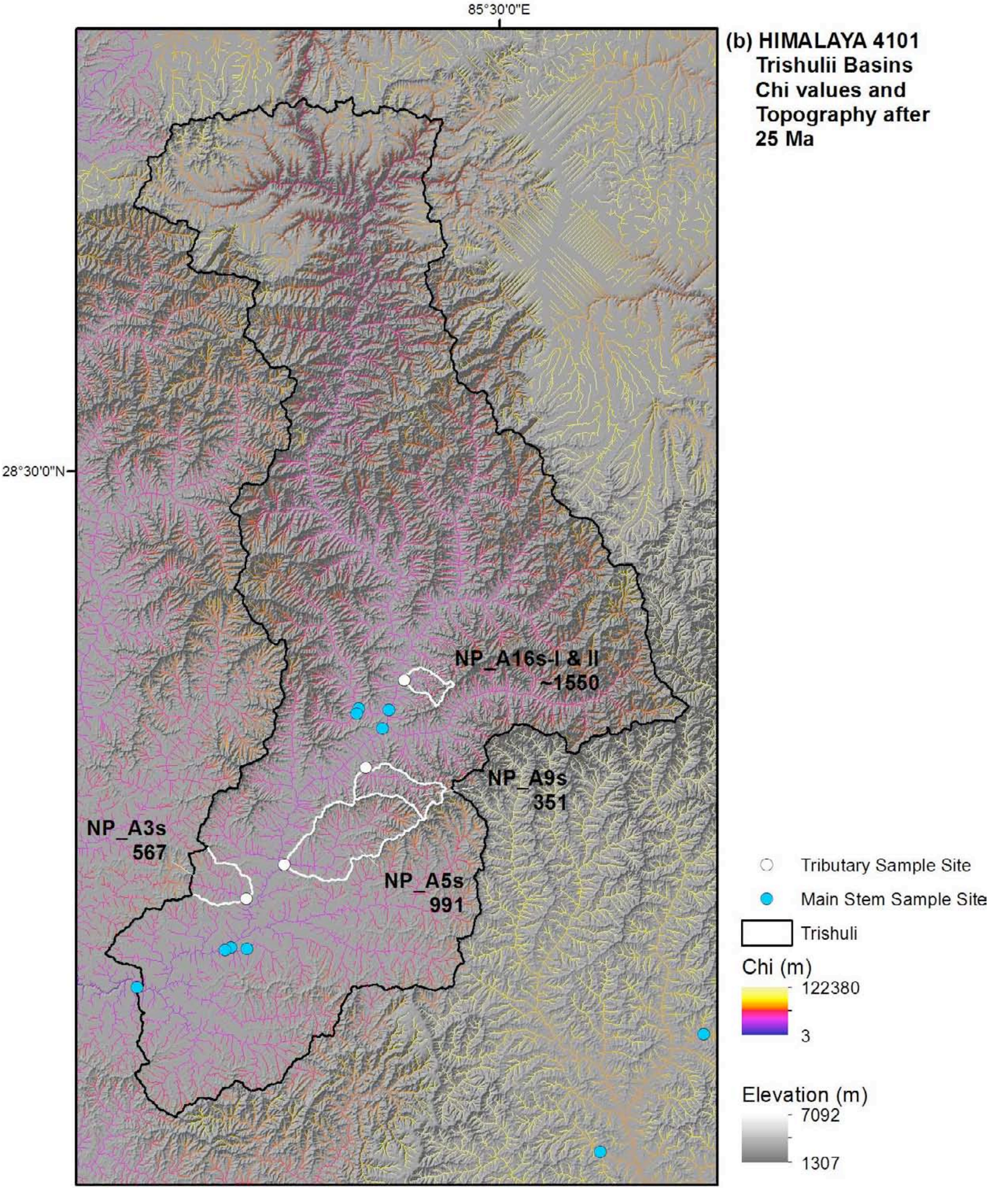

Figure 40. Shaded-relief DEM and chi values for Himalaya 4101 after 25 Ma in the Trishuli River basins from Andermann (2011). Blue circles and white circles indicate cosmogenic ^{10}Be sample sites from glaciated main stem river basins and unglaciated tributary basins (white outlines), respectively. White text list sample numbers and associated ^{10}Be erosion rates.

5.3.1 Namibia 4101: Results for Uniform Uplift and Bilinear Interpolation of Precipitation

Published ^{10}Be erosion rates from three major river catchments, the Omaruru, Swakop, and Gaub, in Namibia (Codilean et al., 2008, 2014; Bierman et al., 2007) are compared with mean, non-zero chi values calculated within those catchments (Figures 41 and 42). Cosmogenic ^{10}Be sample site were collected either from main-stem or tributary basins, and are associated with present-day basin geometries. These same geometries were used to extract non-zero chi values for each basin (Table 4).

Basins in the Omaruru catchment have mean, non-zero chi values ranging from ~25,000 to ~65,000 m and ^{10}Be erosion rates ranging from 8.69 to 11.81 m/Ma (Table 4; Bierman et al., 2007). Erosion rates overlap within uncertainty, giving the Omaruru River catchment an average ^{10}Be erosion rate of 9.96 ± 1.08 m/Ma (± standard deviation). Basins in the Swakop catchment have erosion rates ranging from 6.88 to 13.55 m/Ma, with an average ^{10}Be erosion rate and standard deviation of 10.51 ± 1.80 (m/Ma). Mean, non-zero chi values in the Swakop basins range from ~11,000 to ~39,000 m. Erosion rates for the two catchments are within uncertainty and indistinguishable from one another (Figure 41).

Cosmogenic ^{10}Be sample O128o from the Omaruru catchment and samples S337s, and S216s from the Swakop catchment were collected at the mouths of tributary basins, which, according to FastScape analysis, have expanded their basin areas mostly in their headwaters after 25 Ma. Extraction of chi values based on present-day geometry does not include this increase in drainage area, nor the associated lower chi values associated with lower elevation channels. If these additional chi values were included in the basin statistics, chi values for the O128o, S337s, and S216s basins would be lower than values listed in Table 4 and shown Figure 41. As such, these samples are considered outliers during assessment of whether there is a relationship between mean, non-zero chi values and ^{10}Be erosion rates. Similarly, sample S259lc from the Swakop catchment records ^{10}Be erosion rates for a small basin, which after 25 Ma of FastScape analysis, has lost a considerable amount of higher ground to lateral expansion of a lower elevation main stem bed. This increase in lower chi values has decreased the mean, non-zero chi value, such that sample S259lc is also excluded as an outlier (Figure 41).

Removing the Omaruru and Swakop outliers from a trend analysis results in much smaller ranges of mean, non-zero chi values for both catchments. Basins in the Omaruru and Swakop catchments have mean chi values and standard deviations of ~28,000 ± 2000 and ~28,000± 3000 m, respectively, and chi-value ranges of ~6000 and ~7000 m, respectively (Table 4; Figure 42).

The Omaruru and Swakop catchments have indistinguishable ^{10}Be erosion rates and mean chi values and all basin data points fall within an error ellipse (mean ± 2 standard deviations), except for outliers. Basins with similar chi values, particularly at ridgelines separating the basins, are considered to be in a state of dynamic equilibrium (Willett et al., 2014). Based on FastScape chi values and measured ^{10}Be erosion rates, the Omaruru and Swakop catchments are eroding slowly and the basins within the Omaruru catchment are in equilibrium with one another. It can be argued that the Swakop basins show a weak inverse correlation between chi values and erosion rates, indicating the catchment is approaching equilibrium (Figure 41). This is in agreement with conclusions drawn by Bierman et al. (2007) and Nichols (2007) for the same catchments. Bierman et al. (2007) and Nichols (2007) state that the Omaruru and Swakop rivers basins (Figures 29 to 31) are in a state of dynamic equilibrium, thus, the Namibia landscape is evolving through slow but uniform landscape erosion. The Omaruru and Swakop are in more subdued topography, where the Great Escarpment is more dissected. Erosion may perhaps be in equilibrium with uplift in this region of Namibia, but the basins in the Gaub River catchment to the south show a different behavior.

Overall, erosion rates in the Gaub catchment are low, but the steeper Great Escarpment zone is eroding more rapidly than the more subdued topography of the sloping coastal plain or the upland plateau (Figures 26, 27, and 28). Codilean et al. (2008, 2014) report that basins in the Gaub catchment, which straddle the Great Escarpment, have varying ^{10}Be erosion rates ranging from 3.85 to 18.02 m/Ma (Table 4; Figure 31). In general, the erosion is occurring at rates of ~8 and ~5 m/Ma on the coastal plain and highland plateau respectively, and ~16 m/Ma on the escarpment itself (Codilean et al., 2008, 2014).

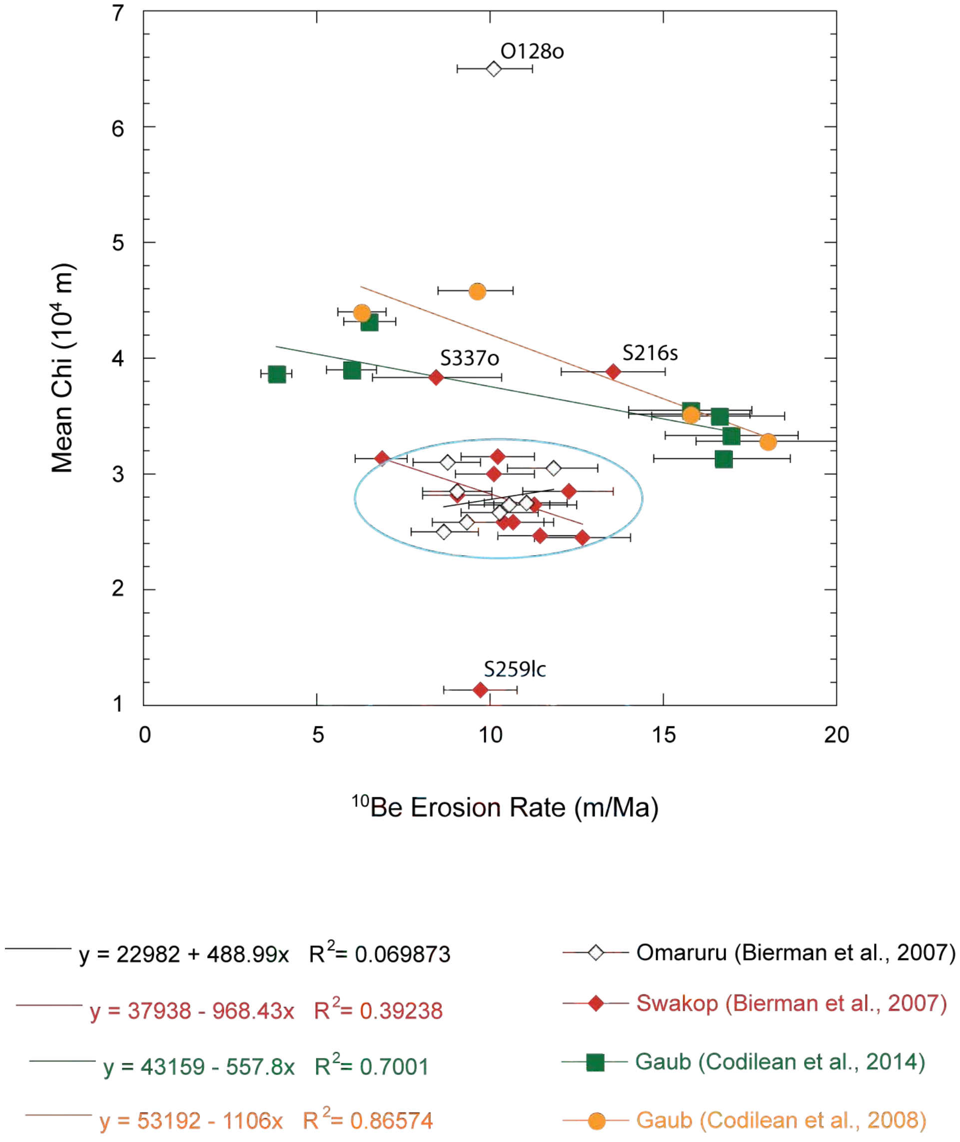

Figure 41. Mean, non-zero chi values in relation to associated ^{10}Be erosion rates for basins in the Omaruru, Swakop, and Gaub River basins in the Namibia 4101 domain after 25 Ma of FastScape model time. The blue line indicates all samples that are within or touching the error ellipse created by the average mean chi values for the Omaruru and Swakop basins and their average ^{10}Be erosion rates.

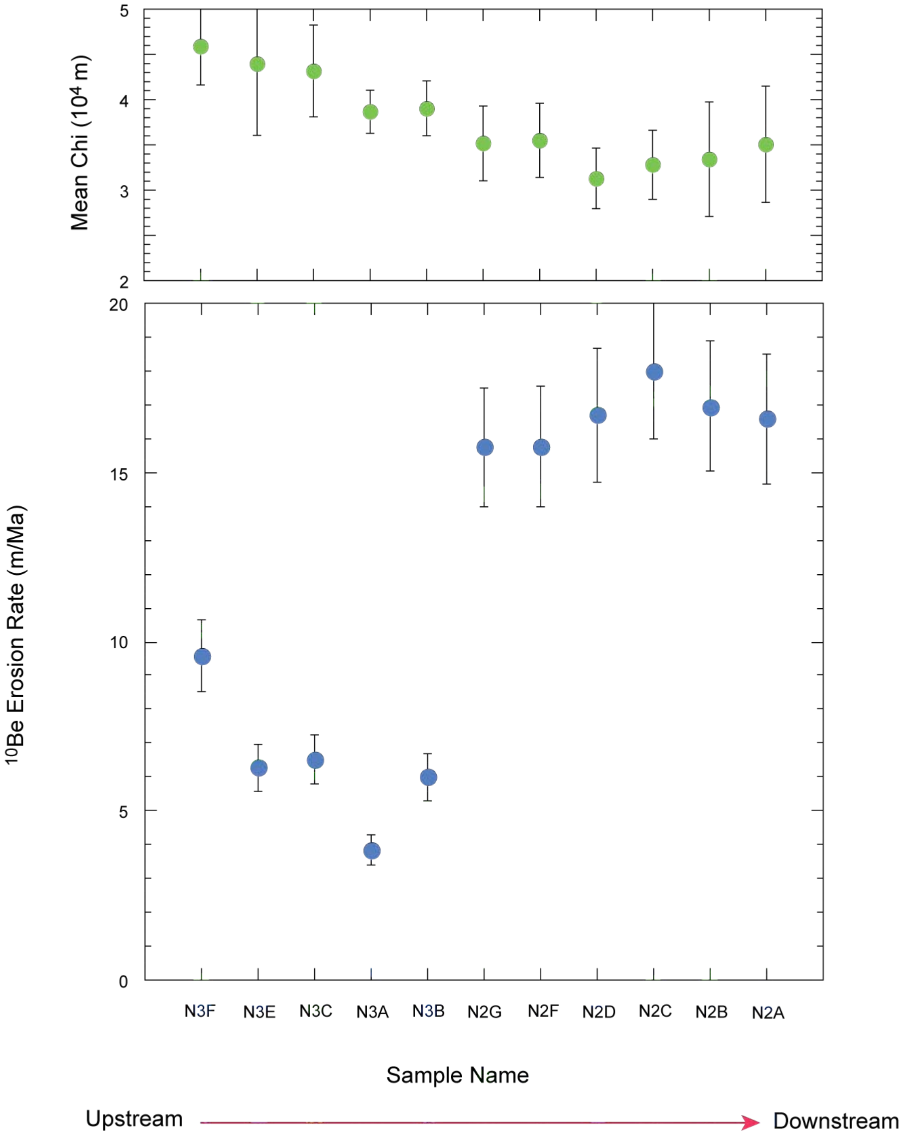

Figure 42. Mean, non-zero chi values and associated ^{10}Be erosion rates listed for tributary basins by sample number in a downstream direction along the Gaub River. Results are from FastScape modeling of the Namibia 4101 domain after 25 Ma.

Table 4. Published cosmogenic ^{10}Be erosion rates and maximum, minimum, and mean chi values for basins with the Omaruru, Swakop, and Gaub River catchments in Namibia.

Author	**River Catchment**	**^{10}Be Sample Number**	**^{10}Be Erosion Rate (m/Ma)**	**^{10}Be Erosion Rate Uncertainty (m/Ma)**	**Basin Minimum Chi (m)**	**Basin Maximum Chi (m)**	**Basin Mean Chi (m)**
Bierman et al. (2007)	Omaruru	O128o	10.12	1.08	7,505	72,543	**65,038***
		O149l	8.69	0.98	11,855	42,395	24,959
		O149o	10.29	1.12	8,769	72,543	26,733
		O171o	10.55	1.16	10,302	72,543	27,361
		O195o	11.03	1.21	12,202	72,543	27,586
		O269o	9.07	1.01	17,051	56,082	28,586
		O269ot	11.81	1.31	17,238	72,543	30,568
		O291n	8.76	0.96	18,786	56,082	31,038
		O299s	9.31	1.00	19,139	41,137	25,906
Bierman et al. (2007)	Swakop	S160t	12.67	1.38	11,877	53,986	24,479
		S184s	11.42	1.21	7,132	60,714	24,712
		S216s	13.55	1.48	28,110	43,844	**38,822***
		S259lc	9.71	1.07	11,396	11,396	**11,396***
		S259s	10.64	1.19	10,505	60,714	25,921
		S279sn	11.30	1.21	12,462	55,120	27,408
		S330o	10.22	1.08	22,037	44,029	31,483
		S333s	9.05	1.01	14,303	60,714	28,158
		S337o	8.47	1.87	38,349	38,349	**38,349***
		S337s	12.26	1.29	17,167	14,900	28,567
		S393o	6.88	0.75	19,913	43,844	31,272
		S397s	10.13	1.14	20,098	47,546	29,938
		S6s	10.39	1.14	4	85,449	25,800
Codilean et al. (2008; 2014)	Gaub	N3E	6.29	0.70	36,521	53,317	43,968
		N3F	9.59	1.08	38,055	57,694	45,902
		N2G	15.75	1.75	27,898	45,363	35,173
		N2C	18.02	2.05	25,978	41,476	32,813
		N2A	16.59	1.92	22,553	49,261	35,074
		N2B	16.95	1.92	22,525	48,696	33,418
		N2D	16.70	1.99	26,141	39,312	31,304
		N2F	15.76	1.78	26,915	45,090	35,502
		N3A	3.85	0.44	35,812	43,891	38,679
		N3B	6.00	0.70	33,987	45,528	39,026
		N3C	6.51	0.74	34,930	54,116	43,172

Note: * indicates samples that are considered outliers when calculating a non-zero chi value relationship with measured cosmogenic ^{10}Be erosion rates. See text for details.

Mean, non-zero chi values in the Gaub basins range from ~31,000 to ~46,000 m/Ma, and basins with higher ^{10}Be erosion rates have lower mean, non-zero chi values (Figure 41). Trend analysis shows that there is an inverse relationship between ^{10}Be erosion rates and chi values with correlation coefficients (R^2) of 0.70 and 0.87 for ^{10}Be data reported in Codilean et al. (2014) and Codilean et al. (2008), respectively. The correlation coefficient is 0.79 if both Gaub ^{10}Be erosion-rate data sets are combined.

Codilean et al. (2008; 2014) conclude that catchments in which erosion rates are slope dependent are not in topographic steady state; landscapes in disequilibrium have steeper slopes that erode more quickly. Chi values decrease in a downstream direction in the Gaub catchment (Figure 42). Chi is directly related to elevation, and thus to slope. Landforms that create higher elevations within a landscape often have steeper hillslopes due to hillslope erosion and channel incision. Basins in the Gaub River catchment have overall higher mean chi values than basins in the Omaruru and Swakop catchments, indicating the Gaub catchment is in disequilibrium relative to catchments to its north.

5.3.2 Himalaya 4101: Results for Uniform Uplift and Precipitation

Published ^{10}Be erosion rates from the Marsyangdi, Bhudi Gandaki, Trishuli, Bhote Koshi, and Tama Koshi catchments in the central Himalaya (Andermann, 2011; Godard et al., 2012; Wobus et al., 2005) are compared with mean, non-zero chi values calculated by FastScape within those catchments (Figure 43). Cosmogenic ^{10}Be sample sites were either from main-stem or tributary basins, some of which have active glaciers (Andermann, 2011; Godard et al., 2012; Wobus et al., 2005). Present-day basin geometries were used to extract non-zero chi values for each basin (Table 5). Mean, non-zero chi values are compared with cosmogenic ^{10}Be erosion rates for basins with reported erosion rates (Figures 44 to 47).

After 25 Ma of FastScape model time, basins in the Marsyangdi, Bhudi Gandaki, and Trishuli River catchments in the western part of the Himalaya 4101 domain have overall lower chi values (<57,000 m; shades of blues and purples) than basins of the Bhote Koshi, Tama Koshi, and Jhikhu Khola catchments in the east (>63,000 m; shades of oranges and yellows; Figure 34). In the east-west direction, the transition occurs primarily between the Trishuli and Bhote Kashi catchments, indicating that with continued landscape evolution, the Bhote Kashi catchment will lose area to the Trishuli catchment as basins with lower chi values expand into areas with higher chi values (Willett et al., 2014).

Reported cosmogenic ^{10}Be erosion rates are, in general, much higher in main-stem river sediments collected from basins with active glaciers than erosion rates of sediment collected from unglaciated tributaries to the main rivers. ^{10}Be erosion rates of the main-stem rivers in the five catchments range from ~1100 m/Ma to ~7900 m/Ma, except for sample NP_A1s from the main-stem Trishuli River, which has a reported erosion rate of 533 m/Ma (Figure 43; Andermann, 2011; Godard et al., 2012; Wobus et al., 2005). There is no correlation between mean, non-zero chi values and ^{10}Be erosion rates in basins with glaciers in their headwaters (Table 5; Figure 43).

Main-stem Marysangdi River basins have ^{10}Be erosion rates ranging from 3266 to 7946 m/Ma and mean, non-zero chi values range from ~22,000 to ~50,000 m. Reported ^{10}Be erosion rates range from 2349 to 4100 m/Ma for sediment samples collected from the main-stem Bhudi Gandaki River. Mean, non-zero chi values in these Bhudi-Gandaki basins range from ~31,000 to ~47,000 m. ^{10}Be erosion rates along the main-stem Trishuli River range from 533 to 4671 m/Ma, but are in general >2000 m/Ma. Corresponding basins have mean chi values ranging from ~28,000 to 47,000 m.

There are only 3 reported ^{10}Be erosion rates for the main-stem Bhote Koshi and Tama Koshi Rivers. Rates range from ~3000 m/Ma in the Tama Koshi catchment to ~3500 m/Ma in the Bhote Koshi catchment (Table 5; Figure 43). Non-zero chi values are ~30,000 – 106,000 m in the one sampled basin in the Tama Koshi catchment. Non-zero chi values range from ~57,000 m to ~115,000 m in the two sampled basins of the Bhote Koshi catchment, with mean chi values of ~84,000 and ~69,000 m.

Table 5. Published cosmogenic ^{10}Be erosion rates and maximum, minimum, and mean chi values for basins with the Marsyangdi, Bhudi Gandaki, Trishuli, Bhote Koshi, and Tama Koshi River catchments in the central Himalaya.

Author	**River Catchment**	**^{10}Be Sample Number**	**^{10}Be Erosion Rate (m/Ma)**	**^{10}Be Erosion Rate Uncertainty (m/Ma)**	**Basin Minimum Chi (m)**	**Basin Maximum Chi (m)**	**Basin Mean Chi (m)**
	Tributary to						
Wobus et al. (2005)	Bhudi Gandaki	01WBS5	241.44	29.34	27,664	37,677	31,684
	Bhudi Gandaki	01WBS6	470.09	55.72	26,441	44,823	34,043
	Bhudi Gandaki	01WBS7	663.33	106.95	25,694	42,746	33,543
	Bhudi Gandaki	**03WBS1**	1138.24	151.08	27,945	35,615	**31,404***
	Bhudi Gandaki	03WBS2	266.38	30.57	29,824	39,175	33,767
	Bhudi Gandaki	**01WBS3**	284.07	37.92	23,224	38,191	**30,377***
	Bhudi Gandaki	**01WBS2**	281.97	36.85	23,282	51,852	**40,265***
	Bhudi Gandaki	01WBS1	261.89	32.77	22,364	39,677	30,537
Andermann (2011)	**Main stem**						
	Bhote Koshi	NP080912A	1115.18	133	57,286	115,353	84,238
	Bhote Koshi	NP080913A	3501.82	407.13	58,652	87,564	69,351
	Bhudi Gandaki	Arr_3A	4100.23	856.24	20,059	66,447	39,537
	Bhudi Gandaki	Arr_3B	4361.49	629.87	18,443	59,043	33,430
	Bhudi Gandaki	Arr_4	2438.97	326.52	18,332	59,508	34,020
	Bhudi Gandaki	NP_A39s	3052.66	603.9	24,242	75,323	46,801
	Marsyangdi	NP081016A	6689.39	1593.5	24,905	74,771	46,601
	Tama Koshi	NP080913B	2969.75	433.73	30,363	105,766	76,215
	Trishuli	Arr_2	2151.3	307.52	21,155	54,702	34,851
	Trishuli	CAJ_7	2028.13	262.83	27,980	81,038	46,634
	Trishuli	NP_A10s	3205.73	571.41	27,621	108,332	45,588
	Trishuli	NP_A12s	4671.82	796.11	29,902	68,378	45,190
	Trishuli	NP_A14s	2537.86	356.6	30,585	51,090	39,901
	Trishuli	NP_A18s	3840.52	700.27	23,063	62,155	33,538
	Trishuli	NP_A1s	533.22	81.59	24,208	65,362	40,705
	Trishuli	NP_A20s	2326.19	531.36	22,954	37,889	28,310
Andermann (2011)	**Tributary to**						
	Jhiku Khola	NP080924A	213.89	24.05	59,806	85,343	71,683
	Bhudi Gandaki	NP_A23s	958.16	121.7	26,008	42,746	33,651
	Tama Koshi	NP080929A	266.55	31.63	56,367	79,740	66,748
	Trishuli	NP_A16s-I	1593.77	301.17	29,382	49,561	37,650
	Trishuli	NP_A16s-II	1521.7	258.93	29,382	49,561	37,650
	Trishuli	NP_A3s	567.33	70.87	25,156	54,109	35,460
	Trishuli	NP_A5s	990.55	116.09	25,096	57,823	39,347
	Trishuli	NP_A9s	350.83	37.11	29,293	55,715	38,879
	Main Stem						
Godard et	Marsyangdi	NEP006	4207.08	648.77	17,159	31,989	22,318

al (2012)								
	Marsyangdi	NEP065	4411.97	585.80	19,544	38,661	26,243
	Marsyangdi	NEP106	7433.97	1211.71	22,021	42,602	28,964
	Marsyangdi	NEP124	6766.98	977.23	28,367	74,865	48,412
	Marsyangdi	NEP139	3266.39	500.61	33,374	74,865	51,123
	Marsyangdi	NEP140	3993.00	539.09	33,601	74,865	50,754
	Marsyangdi	NEP151	3767.54	521.42	37,804	74,771	53,004
	Marsyangdi	NEP171	6671.55	852.76	25,463	42,405	30,589
	Marsyangdi	NIB-975-03	5101.70	618.93	26,062	64,987	38,960
	Marsyangdi	NIB-975-04	5934.86	918.28	26,813	74,865	47,480
	Marsyangdi	NIB-975-06	4879.44	578.37	27,066	74,865	48,047
	Marsyangdi	NIB-975-09	3973.95	635.14	29,965	74,865	49,179
	Marsyangdi	NIB-975-19	7945.61	1157.76	31,396	74,865	50,395
	Marsyangdi	NIB-975-20	7628.87	1142.59	31,176	74,865	49,654
	Marsyangdi	NIB-975-36	3390.02	408.37	17,337	41,783	23,702
	Marsyangdi	NIB-975-52	5740.95	793.29	21,124	34,253	25,383
	Tributary to Marsyangdi						
	Glaciated	NEP138	2807.87	333.35	33,471	73,584	51,375
	Glaciated	NIB-975-10	5912.93	755.25	31,258	70,948	46,512
	Glaciated	NIB-975-21	1555.32	207.47	31,099	66,494	45,815
	Unglaciated	NEP003a	1155.78	143.61	17,055	64,394	36,302
	Unglaciated	NEP030a	88.04	10.28	19,404	51,030	35,137
	Unglaciated	NEP080a	740.10	94.08	21,297	58,897	38,535
	Unglaciated	NEP099a	371.18	43.77	22,659	49,277	33,637
	Unglaciated	NEP118a	4255.15	548.57	27,092	61,723	41,539
	Unglaciated	NIB-975-02a	3293.53	791.78	26,190	55,661	38,978
	Unglaciated	NIB-975-37a	1327.62	155.85	17,213	64,499	36,439
	Unglaciated	NIB-975-44a	2175.99	257.25	23,370	65,298	39,324

Note: * indicates samples that are considered outliers when calculating a non-zero chi value relationship with measured cosmogenic ^{10}Be erosion rates. See text for details.

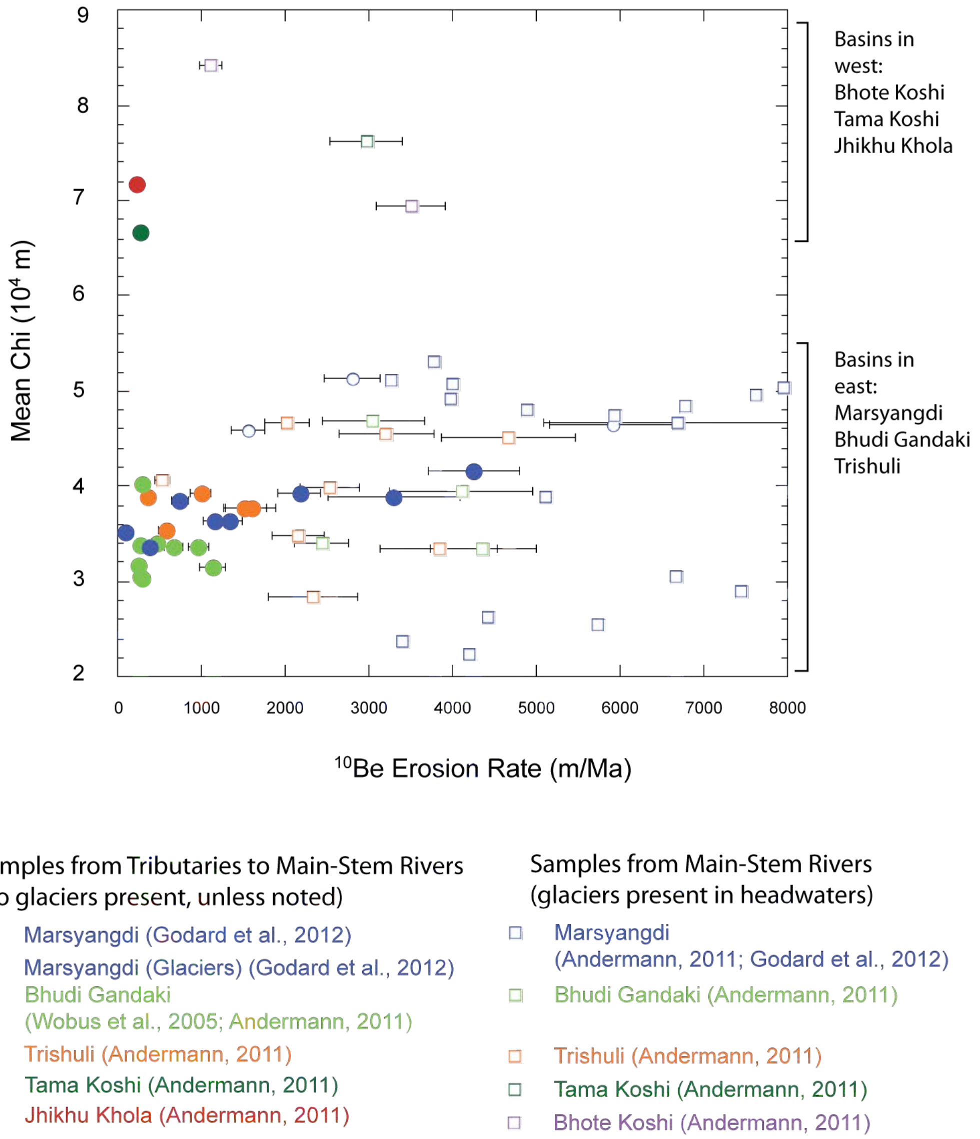

Figure 43. Mean, non-zero chi values and associated ^{10}Be erosion rates for basins in the Marsyangdi, Bhudi Gandaki, Trishuli, Bhote Koshi, Tama Koshi, and Jhikhu Khola basins in the Himalaya 4101 domain after 25 Ma of FastScape model time.

5.3.2.1 Himalaya Tributaries

Tributary basins in the central Himalaya that were sampled by Andermann (2011), Godard et al. (2012), and Wobus et al. (2005) for ^{10}Be erosion studies were selected mainly because there are no glaciers present in the headwaters. Erosion rates for unglaciated tributaries show some variation with mean, non-zero chi values in the Marsyangdi and Bhudi Gandaki. Mean chi values in Trishuli River tributary basins remain relatively constant with increasing ^{10}Be erosion rates (Table 5; Figures 44 to 47).

Mean chi values (~34,000 to ~42,000 m) for tributary basins to the Marsyangdi River increase with increasing erosion rate (88 to 4255 m/Ma). This direct relationship has a correlation coefficient (R^2) of 0.74 (Figure 44). Mean chi values and ^{10}Be erosion rates for these tributary basins also decrease in a downstream, north-to-south direction along the river (Figure 45).

Cosmogenic ^{10}Be erosion rates in Bhudi Ghandaki tributaries vary from 241 to 1138 m/Ma (Figures 44 to 47). Associated mean chi values range from ~30,000 to ~41,000 m. There is a very weak positive correlation ($R^2 = 0.28$) between mean chi values and increasing ^{10}Be erosion rates (Figures 44 and 46); however, three samples were removed from the trend analysis. ^{10}Be erosion rates start around 250 m/Ma, increase along the Bhudi Gandaki with increasing distance downstream and to the south, and then drop abruptly to a constant value of ~250 m/Ma again. Mean chi values are relatively constant, except for basin 01WBS2.

The cosmogenic samples in these Bhudi Gandaki tributaries were taken at the mouths of valleys, where they meet the main stem Bhudi Gandaki. Migration of the main stem Bhudi Gandaki in the FastScape model has occurred in an easterly direction (Figures 34 and 38), thus, the confluences of tributary streams and the main stem have also migrated eastward. Calculation of mean chi values for the present-day tributary basin geometries excludes new, lower chi values associated with this basin migration. This migration does not effect basin 03WBS2, as that basin is located eastward of the main stem Bhudi Gandaki. Basins most affected include 03WBS1 and 01WBS3. These values are also considered outliers when calculating a correlation between mean chi values and ^{10}Be erosion rates for tributaries to the Bhudi Gandaki River. In addition, basin 01WBS2 has lost more than half of its drainage area to a basin that expanded northeastward and captured a stream (Figure 38). The present-day basin geometry includes this stream capture, and thus, includes higher chi values during calculation of a mean chi value for this basin. Basin 01WBS2 is considered an outlier when correlating mean chi values with ^{10}Be erosion rates.

Mean chi values in tributary basins of the Trishuli catchment remain constant with ^{10}Be erosion rates (Figures 44 and 47). Mean chi values range from ~35,000 to ~39,000, with an average value of ~39,000 ± 1500 m (± standard deviation). There is much greater range in erosion rates (351 to 1594 m/Ma), but chi values do not vary with increasing erosion.

Migration of the main stem Trishuli River occurred over 25 Ma of FastScape modeling (Figures 34 and 40). Near basin NP_A3s, the main-stem river migrated eastward, thus, lower chi values associated with migration of the tributary mouth are not included in the calculation of a mean chi value for present-day basin geometry. Furthermore, this basin experienced loss of drainage area in its headwaters to a basin to the northwest. Higher chi values from the adjacent basin are within the boundary of the basin's present-day geometry, and are, thus, included in the mean chi value. There is a small amount of expansion of the basin's western margin into adjacent basin; however, these higher chi values are not contained within the present-day geometry. The mean chi value of basin NP_A3s is overestimated because of these changes to the basin geometry and chi values. Upstream of this basin, the main stem Bhudi Gandaki migrated westward. Small stretches of tributary streams with lower chi values associated with this migration are excluded from mean chi values calculated for basins NP_A5s and NP_A16sI &-II. The mean chi values may be slightly overestimated. Because all basins have potentially excluded both lower and higher chi values from the present-day basin geometries, all chi values are included in the correlation between mean chi values and ^{10}Be erosion rates.

Figure 47 illustrates that erosion rates of Trishuli tributaries decrease in a downstream direction along the main-stem river. Tributaries, however, were only sampled in the southern part of the Trishuli catchment. Chi values in the southern part of the catchment show that basins there are in equilibrium with one another, but in the northern part, the catchment is in disequilibrium to its north and east. Expansion has occurred in the northeast, as well as a stream capture with expansion to the north (Figures 34 and 40). Were there erosion rates reported for unglaciated basins in this northern part of the Trishuli catchment, they might reflect differential erosion between basins in the north and south, and thus disequilibrium within the catchment, as reflected in higher chi values in the north.

Mean chi values of tributaries to the Marsyangdi, Bhudi Gandaki, and Trishuli Rivers overlap, but Bhudi Gandaki basins have the lowest mean chi values. This catchment is positioned between the Marsyangdi and Trishuli catchment, should, theoretically expand into the adjacent basins with continued landscape evolution.

Overall, ^{10}Be erosion rates of tributary basins to the Marsyangdi and Trishuli Rivers are highest upstream and they decrease progressively downstream and to the south. Mean chi values also decrease, from north to south, for Marsyangdi basins. Mean chi values decrease, but only slightly, from north to south in the Bhudi Gandaki catchment. Mean chi values for the Trishuli basins remain relatively constant in a north-to-south direction. In the eastern part of the central Himalaya study area, there appears to be a weak to moderate direct relationship between mean chi values and increasing erosion rates. This is in stark contrast to the inverse relationship between mean chi values and erosion rates in FastScape analysis of Namibia 4101.

There is only one ^{10}Be sample each for the tributaries to the Tama Koshi and Jhiku Khola Rivers, so no relation can be drawn between erosion rates and mean chi values on a catchment-wide basis. Cosmogenic ^{10}Be erosion rates (213 and 266 m/Ma; Table 5) are similar to other rates for non-glaciated tributaries elsewhere in the central Himalaya (Figure 44), but mean chi values (~67,000 and ~72,000 m) are higher than chi values of catchments to the west.

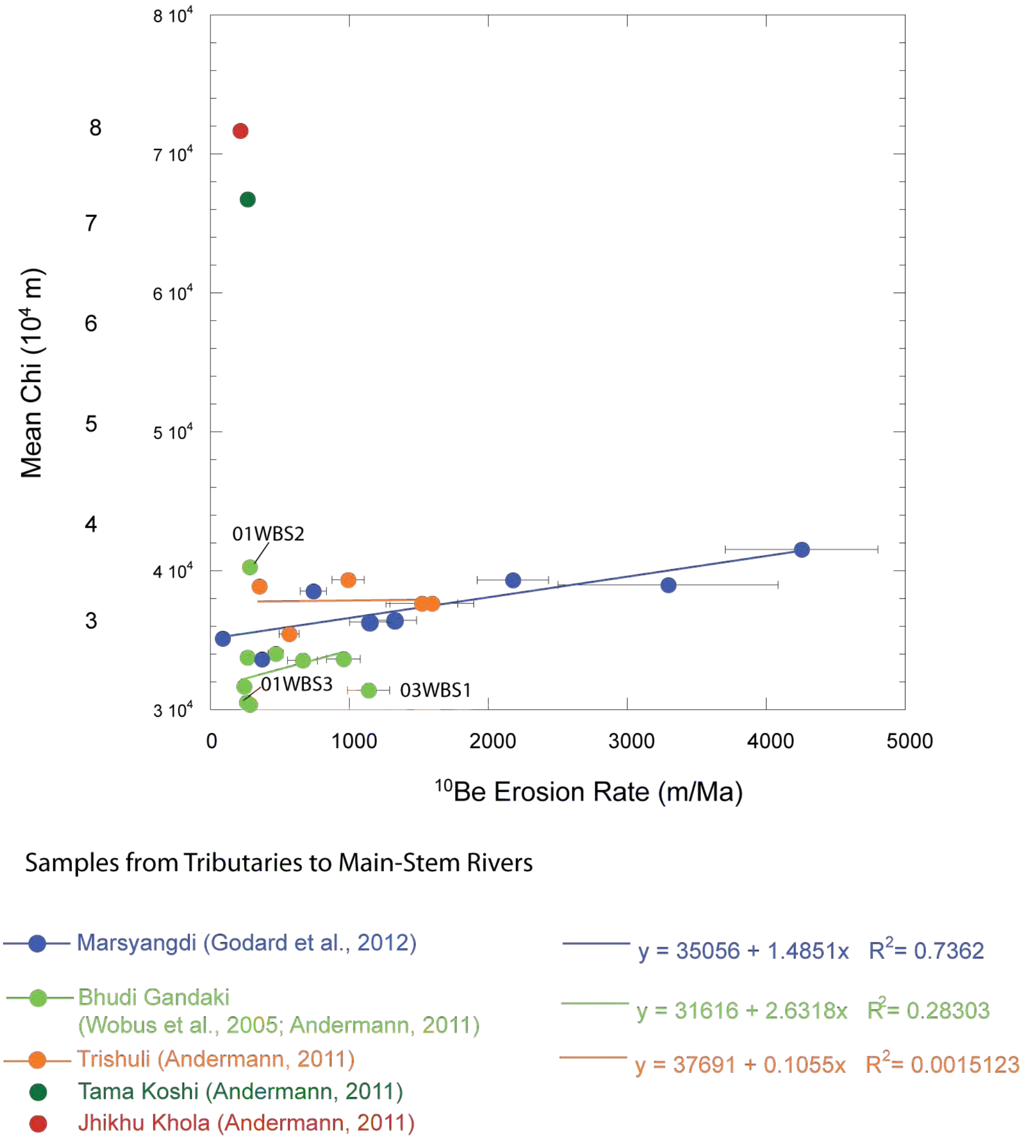

Figure 44. Mean, non-zero chi values and associated ^{10}Be erosion rates for tributary basins in the Marsyangdi, Trishuli, Bhote Koshi, Tama Koshi, and Jhikhu Khola basins in the Himalaya 4101 domain after 25 Ma of FastScape model time.

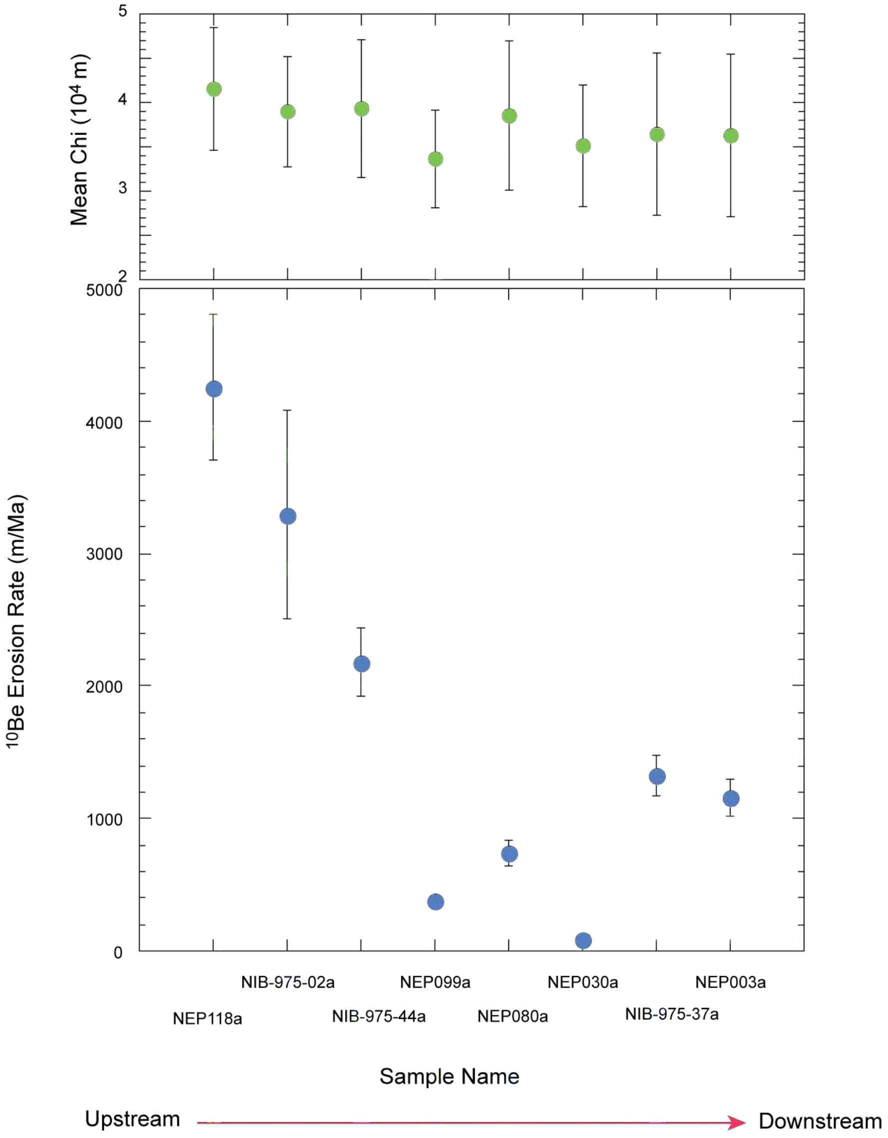

Figure 45. Mean, non-zero chi values and associated ^{10}Be erosion rates listed for tributary basins by sample number in a downstream direction along the Marsyangdi River. Results are from FastScape modeling of the Himalaya 4101 domain after 25 Ma.

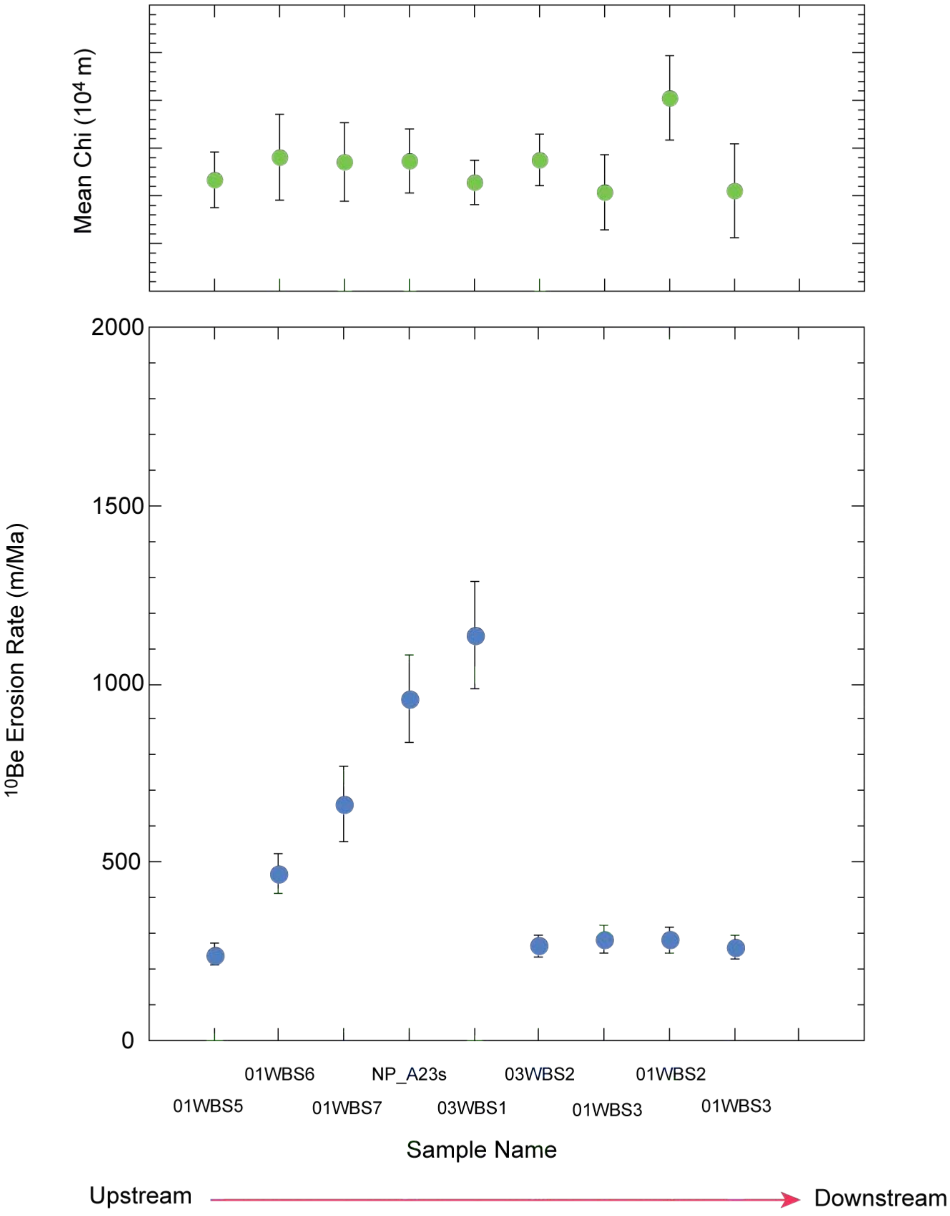

Figure 46. Mean, non-zero chi values and associated ^{10}Be erosion rates listed for tributary basins by sample number in a downstream direction along the Bhudi Gandaki River. Results are from FastScape modeling of the Himalaya 4101 domain after 25 Ma.

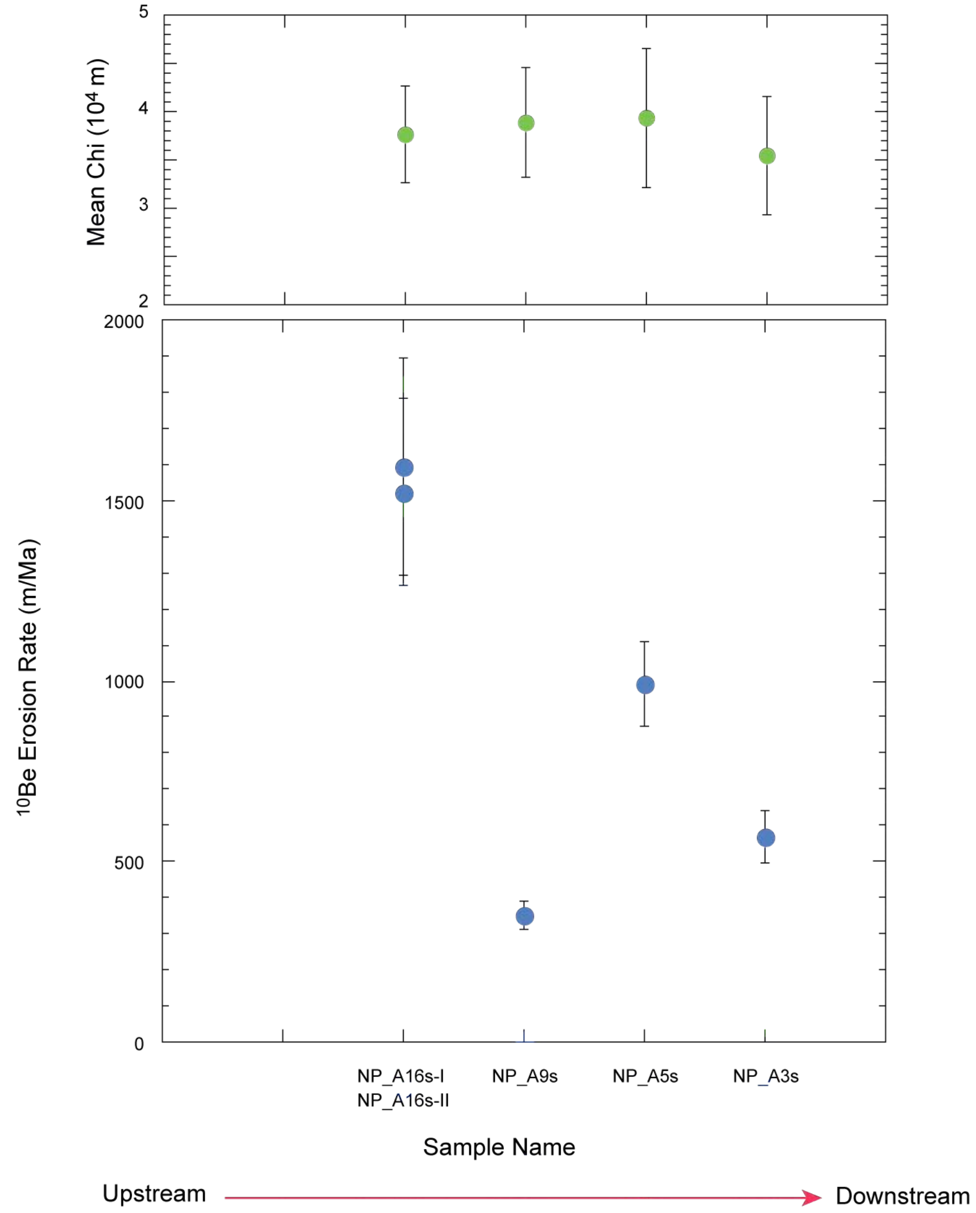

Figure 47. Mean, non-zero chi values and associated ^{10}Be erosion rates listed for tributary basins by sample number in a downstream direction along the Trishuli River. Results are from FastScape modeling of the Himalaya 4101 domain after 25 Ma.

CHAPTER 6: DISCUSSION AND CONCLUSIONS

FastScape erosion is driven by the stream-power law and is directly related to discharge. FastScape chi is dependent on elevation, base level, and catchment area (Equations 7 and 8) Because absolute chi values at the higher-elevation, uppermost reaches of a catchment depend on the catchment area of the basin at base level, chi is very sensitive to domain size.

Subset domains (1601 cells x 1601 cells) yield significantly lower chi values for the same 90-m cell size and same area of interest within a bigger domain (4101 cells x 4101 cells). Subset domains result in lower chi values due to smaller differences between $z(x)$ and z_b, and decreases in total drainage area (~20,000 km^2 vs. ~140,000 km^2). Namibia 1601 and Himalaya 1601 have very similar areas (~20,000 km^2) and maximum chi values (~58,000 m); however, Himalaya 1601 has a mean chi value (~20,000 ± 9,000 m) that is higher than that of Namibia 1601 (~13,000 ± 10,000 m). Himalaya 4101 has 4% more total area than Namibia 4101, and the mean chi value in the former (~42,000 ± 20,000 m) is higher than that in the latter (~28,000 ± 14,000 m).

For example, Namibia 4101 covers approximately 136,000 km^2 and has a base level set at 0 m. The subset Namibia 1601 domain covers approximately 21,000 km^2 and base level is set at 587 m. Some catchments are truncated on the top, right, and bottom boundaries of the 1601 model domain, and are thus smaller in size than those same catchments in Namibia 4101. Truncated basin areas are thus not part of the chi calculations for Namibia 1601. For the same uniform precipitation rate in FastScape, the Namibia 4101 domain has ~6.5 times as much surface area, and thus 6.5 times as much precipitation ‘collected’ in the model that must be routed to base level in order to maintain conservation of water (Braun and Willett, 2013). If base level is set at sea level, chi will be higher than a chi value calculated by FastScape for the same position in the same network where base level starts at 500 m. Comparison of the clipped Namibia 4101 and Namibia 1601 results (Figure 18) shows much more extensive lateral erosion of hillslopes in the former than in the latter. The mean elevation (~1300 m) in the former is also lower than in the latter (~1700 m).

Similar differences are seen when comparing erosion patterns and amounts between clipped Himalaya 4101 and Himalaya 1601 (Figure 21); mean elevations are, however, ~1600 m and ~600 m, respectively. Higher precipitation rates in the central Himalaya drive more rapid erosion than that seen in Namibia modeling.

Chi values are directly related to elevation, and they are higher for the same area with increasing DEM resolution. Chi values are lower in the Namibia ASTER and Himalaya ASTER (30-m cell size) domains than in the Namibia 1601 and Himalaya 1601 domains (90-m cell sizes). Coarser 90-m cells in a DEM capture more variation in elevation within a cell than does a 30-m cell size. Given the sensitivity of chi to domain size, using a finer resolution will not necessarily improve the usefulness of absolute chi values in assessment of states of equilibrium in a landscape.

Because of FastScape chi's sensitivity to domain size, base level, and cell resolution, absolute chi values cannot be directly compared between different regions (e.g., Namibia 4101 and Himalaya 4101) to assess comparative states of landscape equilibrium. Relationships between mean, non-zero chi values and ^{10}Be erosion rates, however, can be compared within each domain. FastScape chi-value results in combination with ^{10}Be erosion rates indicate that northern Namibia catchments, in more subdued topography, are in or approaching equilibrium, where chi values are constant or have a weak inverse correlation with increasing ^{10}Be erosion rates. Constant mean chi values in basins can be either high or low in nature, but if they do not vary with ^{10}Be rates, those basins are in equilibrium (Figure 48). In contrast, catchments, like the Gaub River, which cross the steep Great Escarpment in the south of Namibia, are not in equilibrium. According to FastScape results erosion in Namibia is predominantly driven by precipitation, as uplift rates are minimal. Where disequilibrium occurs in this climatic and tectonic setting, chi values are inversely proportional to reported ^{10}Be erosion rates for tributary basins.

In contrast, the central Himalaya experience precipitation and uplift rates that are one to three orders of magnitude higher than rates in Namibia. Main-stem basins which have glaciers present in their headwaters have ^{10}Be erosion rates that are ~1100 to ~8000 m/Ma, whereas, ^{10}Be erosion rates in unglaciated tributary basins are between ~90 and ~5900 m/Ma in this climatic and tectonic setting. FastScape does not incorporate glacial or hillslope processes into its algorithm. Model erosion is driven solely by precipitation, uplift, and the stream-power law (Equation 5), thus the FastScape landscape derived after 25 Ma of model time is driven by channel migration and incision. FastScape chi values help identify anomalously high ^{10}Be rates that are likely related to the addition of youthful glacially-derived sediment with low ^{10}Be concentrations to main-stem rivers. Godard et al. (2012) conclude that ^{10}Be erosion rates in the main stem Marsyangdi River are significantly impacted by the addition of young, glacially derived sediments, which agrees with the findings of this study. There appears to be no relationship between main-stem erosion rates, which are likely affected by glaciers, and basin, mean chi values. Though erosion rates in unglaciated Marsyangdi River tributaries overlap high erosion rates from glacier-fed, main-stem rivers, the higher rates correlate directly with higher chi values in the tributary basins (Figures 44 and 45). It can be argued that the moderate to weak, positive relationship between chi values and ^{10}Be erosion rates in the Marsyangdi and Bhudi Gandaki tributary basins indicate that these basins are in disequilibrium, and that this disequilibrium may be explained by differential uplift in the north and south of the central Himalaya. Reported erosion rates are higher in the north than in the south, as are uplift rates (Andermann, 2011; Godard et al., 2012, 2014; Wobus et al., 2005). Godard et al. (2014) report a trend of higher erosion rates in the northern central Himalaya and progressively lower erosion rates in the south; along a north-south transect across the central Himalaya, average erosion rates increase significantly from 500 m/Ma in the Lesser Himalayas to ~1000 m/Ma across the Physiographic Transition, and then finally to ~2000 to 3000 m/Ma in the Higher Himalayas (Godard et al., 2012). They infer that differential uplift in the north and south are the primary control on erosion rates, with precipitation having a second order influence.

Chi values of the Trishuli tributaries appear to indicate that these basins in the southern part of the catchment are in equilibrium. Differential chi values in the northern part of the Trishuli catchment, however, indicate strong disequilibrium with a catchment to the north and the Bhote Koshi catchment to the east. In fact, FastScape models a stream capture by the Trishuli catchment, where it has rerouted a river from the northern catchment into the Trishuli River (Figure 40). There are not yet reported ^{10}Be erosion rates for the northern Trishuli catchment to corroborate this.

Chi values alone provide a visual 'snapshot' of a landscape at a given model time, which indicate whether parts or the whole of a landscape within the model domain are in a state of equilibrium (Willet et al., 2014). Using chi values in combination with cosmogenic ^{10}Be erosion rates is shown to be a powerful approach to investigate states of equilibrium. Chi values also provide an independent assessment of ^{10}Be erosion rates, such that glacial settings with high erosion rates show no relationship to chi values. This would likely be true in basins affected by young mass movements, such as landslides and/or debris flows (Kober et al., 2013; Salcher et al., 2014).

Furthermore, chi values remain constant with increasing ^{10}Be erosion rates for unglaciated tributary basins in equilibrium. An inverse relationship between chi values and ^{10}Be erosion rates in unglaciated tributary basins indicate disequilibrium in a setting where erosion is driven predominantly by precipitation. Positive correlations between chi values and ^{10}Be erosion rates indicate disequilibrium in a setting where erosion is dominated by tectonic uplift (Figure 48).

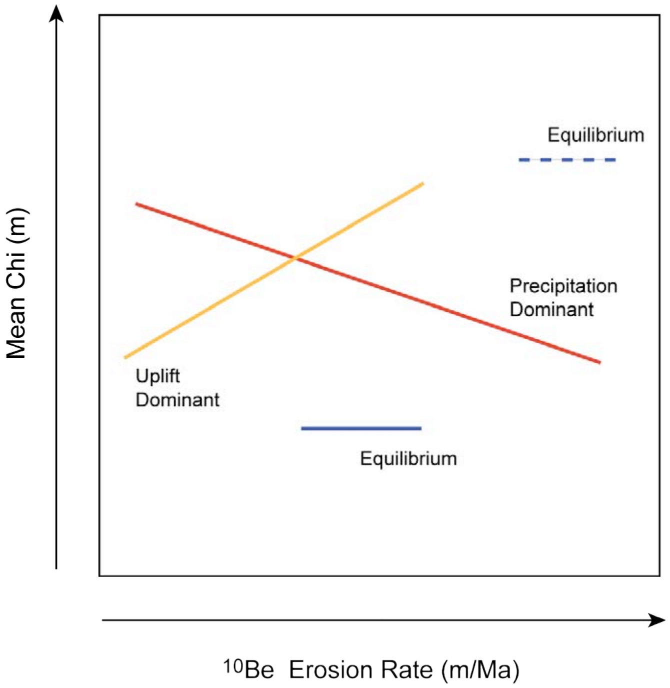

Figure 48. Schematic diagram of relationships between chi-value and ^{10}Be erosion rates in basins/regions of uplift-dominant disequilibrium (orange line), precipitation-dominant disequilibrium (red line), and equilibrium (blue dashed and blue solid lines).

CHAPTER 7: FUTURE OUTLOOK

FastScape uses raster DEMS in its modeling. It is possible that the local-minima problem may result from the use of a regular, rectangular grid, and that using a TIN surface may eliminate the local-minima problem earlier in FastScape modeling. It would be useful to model the Namibia 4101 and Himalaya 4101 domains using TIN surfaces to test whether 'present-day' chi values can be calculated. Because a certain amount of model time is needed in order to remove local minima, 'present-day' (e.g., < 10 ka) is defined in terms of geologic time on the timescale of mountain-building process (>10 Ma).

Cosmogenic ^{10}Be samples are collected from mainstream and tributary stream sediments in present-day streambeds. Stream networks migrate laterally and vertically in the FastScape as landscape evolves in FastScape model time. Thus, after 25 Ma of FastScape modeling, sample locations (e.g., GPS locations recorded during ^{10}Be studies) might no longer be located in a streambed, but perhaps on a hill slope or ridgeline. Building off this study, it would be to useful estimate the location of the present-day cosmogenic sample site in future FastScape stream networks, and compute new catchments for each of the ^{10}Be samples. One could then compare the drainage area of the present-day catchments to the future drainage area and compare losses or gains of area with ^{10}Be erosion rates. In theory, basins with higher erosion rates should have increased their catchment size, and basins with lower rates might have lost catchment area, or have increased their catchment sizes but with smaller increases than basins with higher erosion rates. If no significant change to basin geometry occurred, this would indicate dynamic equilibrium. More accurate mean, non-zero chi values could be extracted from FastScape basin geometries and compared to ^{10}Be erosion rates. Also, the chi value of a point on the landscape will have a longer averaging timescale than that of cosmogenic ^{10}Be erosion rates. For example, the Namibian landscape changed on the order of only 1 or 2 m over the time recorded by the ^{10}Be in river- sand samples (Bierman et al., 2007; Codilean 2008; 2014). This means that the way points will plot on a mean chi vs. ^{10}Be erosion-rate plot, might not depend so much on the ^{10}Be rate, but on the evolution history of their catchments. Catchment geometries might have been very different prior to the time interval captured by ^{10}Be signatures in sediment samples.

Landscapes in other geomorphic, tectonic, and climatic settings, as well as geographic locations, which also have reported cosmogenic ^{10}Be erosion rates, should be analyzed in order to further test the relationship between chi values and ^{10}Be erosion rates and their combined use to assess whether disequilibrium is driven by climate or by tectonics.

REFERENCES CITED

Andermann C. 2011. Climate, topography and erosion in the Nepal Himalayas, PhD, Université de Rennes 1.

Bierman PR. 1994. Using in situ produced cosmogenic isotopes to estimate rates of landscape evolution: A review from the geomorphic perspective. Journal of Geophysical Research: Solid Earth **99** : 13885–13896. DOI: 10.1029/94JB00459

Bierman PR, Caffee M. 2001. Slow Rates of Rock Surface Erosion and Sediment Production across the Namib Desert and Escarpment, Southern Africa. American Journal of Science **301** : 326–358. DOI: 10.2475/ajs.301.4-5.326

Bierman, PR, Nichols KK, Matmon A, Enzel Y, Larsen J, Finkel RC. 2007. 10-Be shows that Namibian drainage basins are slowly, steadily and uniformly eroding. Quaternary International, 167 : 168.

Bierman PR, Nichols KK. 2004. Rock to Sediment—Slope to Sea with ^{10}Be—Rates of Landscape Change. Annual Review of Earth and Planetary Sciences **32** : 215–255. DOI: 10.1146/annurev.earth.32.101802.120539

Bishop P. 2007. Long-term landscape evolution: linking tectonics and surface processes. Earth Surface Processes and Landforms **32** : 329–365. DOI: 10.1002/esp.1493

Bogdon C. 2013. Groundwater Modeling Numerical Methods: Which One Should You Use? [online] Available from: http://www.novametrixgm.com/blog/groundwater-modeling-numerical-methods-which-one-should-you-use (Accessed 21 May 2015)

Braun J. 2013. FastScape User Guide. Universite Joseph Fourier De Grenoble : 129 pp.

Braun J, Simon-Labric T, Murray KE, Reiners PW. 2014. Topographic relief driven by variations in surface rock density. Nature Geoscience **7** : 534–540. DOI: 10.1038/ngeo2171

Braun J, Willett SD. 2013. A very efficient O(n), implicit and parallel method to solve the stream power equation governing fluvial incision and landscape evolution. Geomorphology **180-181** : 170–179. DOI: 10.1016/j.geomorph.2012.10.008

Bull WB. 1991. Geomorphic responses to climatic change. New York, NY; Oxford University Press : 326 pp.

Cerling TE, Craig H. 1994. Cosmogenic ^{3}He production rates from 39°N to 46°N latitude, western USA and France. Geochimica et Cosmochimica Acta **58** : 249–255. DOI: 10.1016/0016-7037(94)90462-6

CGIAR-CSI. n.d. SRTM 90m Digital Elevation Database v4.1 | CGIAR-CSI [online] Available from: http://www.cgiar-csi.org/data/srtm-90m-digital-elevation-database-v4-1 (Accessed 2 March 2015)

Chen A, Darbon J, Morel J-M. 2014. Landscape evolution models: A review of their fundamental equations. Geomorphology **219** : 68–86. DOI: 10.1016/j.geomorph.2014.04.037

Cockburn HAP, Summerfield MA. 2004. Geomorphological applications of cosmogenic isotope analysis. Progress in Physical Geography **28** : 1–42. DOI: 10.1191/0309133304pp395oa

Codilean AT. 2006. Calculation of the cosmogenic nuclide production topographic shielding scaling factor for large areas using DEMs. Earth Surface Processes and Landforms **31** : 785–794. DOI: 10.1002/esp.1336

Codilean AT, Bishop P, Hoey TB. 2006. Surface process models and the links between tectonics and topography. Progress in Physical Geography **30** : 307–333. DOI: 10.1191/0309133306pp480ra

Codilean AT, Bishop P, Stuart FM, Hoey TB, Fabel D, Freeman SPHT. 2008. Single-grain cosmogenic 21Ne concentrations in fluvial sediments reveal spatially variable erosion rates. Geology **36** : 159–162. DOI: 10.1130/G24360A.1

Codilean AT, Fenton CR, Fabel D, Bishop P, Xu S. 2014. Discordance between cosmogenic nuclide concentrations in amalgamated sands and individual fluvial pebbles in an arid zone catchment. Quaternary Geochronology **19** : 173–180. DOI: 10.1016/j.quageo.2012.04.007

Coulthard TJ. 2001. Landscape evolution models: a software review. Hydrological Processes **15** : 165–173. DOI: 10.1002/hyp.426

Davy P, Lague D. 2009. Fluvial erosion/transport equation of landscape evolution models revisited. Journal of Geophysical Research : Earth Surface **114** : F03007. DOI: 10.1029/2008JF001146.

Deren L, Xiao-Yong C. 1991. Automatically generating triangulated irregular digital terrain model networks by mathematical morphology. ISPRS Journal of Photogrammetry and Remote Sensing **46** : 283–295. DOI: 10.1016/0924-2716(91)90045-W

DIVA-GIS. 2015. Download data by country [online] Available from: http://www.diva-gis.org/gdata

Dortch JM, Dietsch C, Owen LA, Caffee MW, Ruppert K. 2011. Episodic fluvial incision of rivers and rock uplift in the Himalaya and Transhimalaya. Journal of the Geological Society **168** : 783–804. DOI: 10.1144/0016-76492009-158

Dunai TJ. 2010. Cosmogenic Nuclides: Principles, Concepts and Applications in the Earth Surface Sciences. 1st edition. Cambridge University Press: Cambridge, UK ; New York

Dupont-Nivet G, Lippert PC, Hinsbergen DJJV, Meijers MJM, Kapp P. 2010. Palaeolatitude and age of the Indo–Asia collision: palaeomagnetic constraints. Geophysical Journal International **182** : 1189–1198. DOI: 10.1111/j.1365-246X.2010.04697.x

Evans IS. 2012. Geomorphometry and landform mapping: What is a landform? Geomorphology **137** : 94–106. DOI: 10.1016/j.geomorph.2010.09.029

Farr TG, et al. 2007. The Shuttle Radar Topography Mission. Reviews of Geophysics **45** DOI: 10.1029/2005RG000183 [online] Available from: http://doi.wiley.com/10.1029/2005RG000183 (Accessed 27 May 2015)

Finnegan NJ, Hallet B, Montgomery DR, Zeitler PK, Stone JO, Anders AM, Yuping L. 2008. Coupling of rock uplift and river incision in the Namche Barwa–Gyala Peri massif, Tibet. Geological Society of America Bulletin **120** : 142–155. DOI: 10.1130/B26224.1

Gerya TV, May DA, Duretz T. 2013. An adaptive staggered grid finite difference method for modeling geodynamic Stokes flows with strongly variable viscosity. Geochemistry, Geophysics, Geosystems **14** : 1200–1225. DOI: 10.1002/ggge.20078

Giannoni F, Roth G, Rudari R. 2005. A procedure for drainage network identification from geomorphology and its application to the prediction of the hydrologic response. Advances in Water Resources **28** : 567–581. DOI: 10.1016/j.advwatres.2004.11.013

Gilbert GK. 1877. Report on the geology of the Henry Mountains [Utah]. US Government Printing Office.

Godard V, Bourlès DL, Spinabella F, Burbank DW, Bookhagen B, Fisher GB, Moulin A, Léanni L. 2014. Dominance of tectonics over climate in Himalayan denudation. Geology **42** : 243–246. DOI: 10.1130/G35342.1

Godard V, Burbank DW, Bourlès DL, Bookhagen B, Braucher R, Fisher GB. 2012. Impact of glacial erosion on ^{10}Be concentrations in fluvial sediments of the Marsyandi catchment, central Nepal. Journal of Geophysical Research: Earth Surface **117** : F03013. DOI: 10.1029/2011JF002230

Goren L, Willett SD, Herman F, Braun J. 2014. Coupled numerical-analytical approach to landscape evolution modeling. Earth Surface Processes and Landforms **39** : 522–545. DOI: 10.1002/esp.3514

Gosse JC, Phillips FM. 2001. Terrestrial in situ cosmogenic nuclides: theory and application. Quaternary Science Reviews **20** : 1475–1560. DOI: 10.1016/S0277-3791(00)00171-2

Granger DE, Kirchner JW, Finkel R. 1996. Spatially Averaged Long-Term Erosion Rates Measured from in Situ-Produced Cosmogenic Nuclides in Alluvial Sediment. The Journal of Geology **104** : 249–257.

Granger DE, Schaller M. 2014. Cosmogenic Nuclides and Erosion at the Watershed Scale. Elements **10** : 369–373. DOI: 10.2113/gselements.10.5.369

Hack JT. 1975. Dynamic equilibrium and landscape evolution. Theories of Landform Development **1** : 87–102.

Hancock GR, Evans KG. 2006. Channel head location and characteristics using digital elevation models. Earth Surface Processes and Landforms **31** : 809–824. DOI: 10.1002/esp.1285

Hancock GR, Willgoose GR, Lowry J. 2013. Transient landscapes: gully development and evolution using a landscape evolution model. Stochastic Environmental Research and Risk Assessment **28** : 83–98. DOI: 10.1007/s00477-013-0741-y

Henck AC, Huntington KW, Stone JO, Montgomery DR, Hallet B. 2011. Spatial controls on erosion in the Three Rivers Region, southeastern Tibet and southwestern China. Earth and Planetary Science Letters **303** : 71–83. DOI: 10.1016/j.epsl.2010.12.038

Hengl T, Evans IS. 2009. Chapter 2 Mathematical and Digital Models of the Land Surface. In Developments in Soil Science , . Elsevier; 31–63. [online] Available from: http://linkinghub.elsevier.com/retrieve/pii/S0166248108000020 (Accessed 30 April 2015)

Hengl T, MacMillan RA. 2009. Chapter 19 Geomorphometry — A Key to Landscape Mapping and Modelling. In Developments in Soil Science , . Elsevier; 433–460. [online] Available from: http://linkinghub.elsevier.com/retrieve/pii/S0166248108000196 (Accessed 30 April 2015)

Hirschmiller J, Grujic D, Bookhagen B, Coutand I, Huyghe P, Mugnier J-L, Ojha T. 2014. What controls the growth of the Himalayan foreland fold-and-thrust belt? Geology **42** : 247–250. DOI: 10.1130/G35057.1

International Centre for Integrated Mountain Development (ICIMOD). 2015. [online] Available from: http://rds.icimod.org/DatasetMasters/Download/9352

Kim B, Sanders BF, Schubert JE, Famiglietti JS. 2014. Mesh type tradeoffs in 2D hydrodynamic modeling of flooding with a Godunov-based flow solver. Advances in Water Resources **68** : 42–61. DOI: 10.1016/j.advwatres.2014.02.013

Kirby E, Harkins N. 2013. Distributed deformation around the eastern tip of the Kunlun fault. International Journal of Earth Sciences **102** : 1759–1772. DOI: 10.1007/s00531-013-0872-x

Kirby E, Whipple KX. 2012. Expression of active tectonics in erosional landscapes. Journal of Structural Geology **44** : 54–75. DOI: 10.1016/j.jsg.2012.07.009

Kirby E, Whipple KX, Tang W, Chen Z. 2003. Distribution of active rock uplift along the eastern margin of the Tibetan Plateau: Inferences from bedrock channel longitudinal profiles. Journal of Geophysical Research: Solid Earth **108** : 2217. DOI: 10.1029/2001JB000861

Kober, F, Hippe, K, Salcher, B, Grischott, R, Christl, M, Hählen, N. 2013. Sediment tracing, mixing and budgets in debris flow catchments: a cosmogenic nuclide perspective. In EGU General Assembly Conference Abstract*s* **15** : 9897.

Lavé J, Avouac JP. 2000. Active folding of fluvial terraces across the Siwaliks Hills, Himalayas of central Nepal. Journal of Geophysical Research: Solid Earth **105** : 5735–5770. DOI: 10.1029/1999JB900292

Lavé J, Avouac JP. 2001. Fluvial incision and tectonic uplift across the Himalayas of central Nepal. Journal of Geophysical Research: Solid Earth **106** : 26561–26591. DOI: 10.1029/2001JB000359

Longley P, Goodchild, M. 2005. Geographic Information Systems and Science . John Wiley & Sons : 540 pp.

METI NASA. 2012. ASTER Global Digital Elevation Model (ASTER GDEM): Easy-to-use topographic information of the global terrain [online] Available from: http://www.jspacesystems.or.jp/ersdac/GDEM/E/index.html

Molnar P, Tapponnier P. 1975. Cenozoic tectonics of Asia: effects of a continental collision. Science **189** : 419–426.

Montgomery DR, Dietrich WE. 1992. Channel Initiation and the Problem of Landscape Scale. Science **255** : 826–830.

Montgomery DR, Foufoula-Georgiou E. 1993. Channel network source representation using digital elevation models. Water Resources Research **29** : 3925–3934. DOI: 10.1029/93WR02463

Nichols KK. 2007. Namibia: Interesting landscapes but monotonous erosion rates. presented at the GSA Annual Meeting (28–31 October 2007). Denver. 603 pp.

NOAA NCEI. 2015. Digital Elevation Model (DEM) Discovery Portal [online] Available from: http://www.ngdc.noaa.gov/mgg/dem/demportal.html (Accessed 27 May 2015)

O'Callaghan JF, Mark DM. 1984. The extraction of drainage networks from digital elevation data. Computer Vision, Graphics, and Image Processing **28** : 323–344. DOI: 10.1016/S0734-189X(84)80011-0

Okabe A, Yamada I. 2001. The K-function method on a network and its computational implementation. Geographical Analysis **33** : 271–290.

Ouimet WB, Whipple KX, Granger DE. 2009. Beyond threshold hillslopes: Channel adjustment to base-level fall in tectonically active mountain ranges. Geology **37** : 579–582. DOI: 10.1130/G30013A.1

Ouimet W, Whipple K, Royden L, Reiners P, Hodges K, Pringle M. 2010. Regional incision of the eastern margin of the Tibetan Plateau. Lithosphere **2** : 50–63. DOI: 10.1130/L57.1

Pazzaglia FJ. 2003. Landscape Evolution models. Development in Quaternary Science **1** : 247–274. DOI: DOI:10.1016/S1571-0866(03)01012-1

Peiró J, Sherwin S. 2005. Finite Difference, Finite Element, and Finite Volume Methods for Partial Differential Equations. In Handbook of Materials Modeling. Springer; 1–32. [online] Available from: http://wwwf.imperial.ac.uk/ssherw/spectralhp/papers/HandBook.pdf

Pelletier JD. 2013. A robust, two-parameter method for the extraction of drainage networks from high-resolution digital elevation models (DEMs): Evaluation using synthetic and real-world DEMs. Water Resources Research **49** : 75–89. DOI: 10.1029/2012WR012452

Peuquet DJ. 1984. A conceptual framework and comparison of spatial data models. Cartographica **21** : 66–113. DOI: 10.3138/D794-N214-221R-23R5

Pike RJ. 2000. Geomorphometry -diversity in quantitative surface analysis. Progress in Physical Geography **24** : 1–20. DOI: 10.1177/030913330002400101

Pike RJ, Evans IS, Hengl T. 2009. Chapter 1 Geomorphometry: A Brief Guide. In Developments in Soil Science , . Elsevier; 3–30. [online] Available from: http://linkinghub.elsevier.com/retrieve/pii/S0166248108000019 (Accessed 30 April 2015)

Pritchard D, Roberts GG, White NJ, Richardson CN. 2009. Uplift histories from river profiles. Geophysical Research Letters **36** : L24301. DOI: 10.1029/2009GL040928

Rasemann S, Schmidt J, Schrott L, Dikau R. 2004. Geomorphometry in mountain terrain. In Geographic Information Science and Mountain Geomorphology , . Springer: Berlin; 101–145.

Refice A, Giachetta E, Capolongo D. 2012. SIGNUM: A Matlab, TIN-based landscape evolution model. Computers & Geosciences **45** : 293–303. DOI: 10.1016/j.cageo.2011.11.013

Reynhout SA. 2011. Slow denudation within an active orogen: Ladakh Range, northern India, University of Cincinnati [online] Available from: https://etd.ohiolink.edu/ap/10?0::NO:10:P10_ACCESSION_NUM:ucin1307320889 (Accessed 10 June 2015)

Salcher, BC, Kober, F, Kissling, E, Willett, SD. 2014. Glacial impact on short-wavelength topography and long-lasting effects on the denudation of a deglaciated mountain range. Global and Planetary Change **115** : 59-70.

Schaller M, von Blanckenburg F, Hovius N, Kubik PW. 2001. Large-scale erosion rates from in situ-produced cosmogenic nuclides in European river sediments. Earth and Planetary Science Letters **188** : 441–458. DOI: 10.1016/S0012-821X(01)00320-X

Scherler D, Bookhagen B, Strecker MR. 2014. Tectonic control on ^{10}Be-derived erosion rates in the Garhwal Himalaya, India. Journal of Geophysical Research: Earth Surface **119** : 2013JF002955. DOI: 10.1002/2013JF002955

Sklar L, Dietrich WE. 1998. River Longitudinal Profiles and Bedrock Incision Models: Stream Power and the Influence of Sediment Supply. In Rivers Over Rock: Fluvial Processes in Bedrock Channels , Tinkler KJ and Wohl EE (eds). American Geophysical Union; 237–260. [online] Available from: http://onlinelibrary.wiley.com/doi/10.1029/GM107p0237/summary (Accessed 29 July 2014)

Stollhofen H, Stanistreet IG, von Hagke C, Nguno A. 2014. Pliocene–Pleistocene climate change, sea level and uplift history recorded by the Horingbaai fan-delta, NW Namibia. Sedimentary Geology **309** : 15–32. DOI: 10.1016/j.sedgeo.2014.05.008

Tarolli P, Dalla Fontana G. 2009. Hillslope-to-valley transition morphology: New opportunities from high resolution DTMs. Geomorphology **113** : 47–56. DOI: 10.1016/j.geomorph.2009.02.006

Temme AJAM, Claessens L, Veldkamp A, Schoorl JM. 2011. Evaluating choices in multi-process landscape evolution models. Geomorphology **125** : 271–281. DOI: 10.1016/j.geomorph.2010.10.007

Tribe A. 1991. Automated recognition of valley heads from digital elevation models. Earth Surface Processes and Landforms **16** : 33–49. DOI: 10.1002/esp.3290160105

Tribe A. 1992. Automated recognition of valley lines and drainage networks from grid digital elevation models: a review and a new method. Journal of Hydrology **139** : 263–293. DOI: 10.1016/0022-1694(92)90206-B

Tucker GE, Hancock GR. 2010. Modelling landscape evolution. Earth Surface Processes and Landforms **35** : 28–50. DOI: 10.1002/esp.1952

Tucker G, Lancaster S, Gasparini N, Bras R. 2001. The Channel-Hillslope Integrated Landscape Development Model (CHILD). In Landscape Erosion and Evolution Modeling, Harmon RS and III WWD (eds). Springer US; 349–388. [online] Available from: http://link.springer.com/chapter/10.1007/978-1-4615-0575-4_12 (Accessed 28 May 2015)

USGS. 2015. National Elevation Dataset [online] Available from: http://ned.usgs.gov/

USGS EROS. 2012. Elevation Products [online] Available from: http://eros.usgs.gov/elevation-products

Vance D, Bickle M, Ivy-Ochs S, Kubik PW. 2003. Erosion and exhumation in the Himalaya from cosmogenic isotope inventories of river sediments. Earth and Planetary Science Letters **206** : 273–288. DOI: 10.1016/S0012-821X(02)01102-0

Van der Wateren FM, Dunai TJ. 2001. Late Neogene passive margin denudation history—cosmogenic isotope measurements from the central Namib desert. Global and Planetary Change **30** : 271–307. DOI: 10.1016/S0921-8181(01)00104-7

Von Blanckenburg F. 2005. The control mechanisms of erosion and weathering at basin scale from cosmogenic nuclides in river sediment. Earth and Planetary Science Letters **237** : 462–479. DOI: 10.1016/j.epsl.2005.06.030

Whipple KX. 2004. Bedrock Rivers and the Geomorphology of Active Orogens. Annual Review of Earth and Planetary Sciences **32** : 151–185. DOI: 10.1146/annurev.earth.32.101802.120356

Whipple KX, Tucker GE. 1999. Dynamics of the stream-power river incision model: Implications for height limits of mountain ranges, landscape response timescales, and research needs. Journal of Geophysical Research **104** : 17661–17674. DOI: 10.1029/1999JB900120

Willett SD, McCoy SW, Perron JT, Goren L, Chen C-Y. 2014. Dynamic Reorganization of River Basins. Science **343** : 1248765–1248765. DOI: 10.1126/science.1248765

Wobus C, Heimsath A, Whipple K, Hodges K. 2005. Active out-of-sequence thrust faulting in the central Nepalese Himalaya. Nature **434** : 1008–1011. DOI: 10.1038/nature03499

Wohl E. 2014. Time and the rivers flowing: Fluvial geomorphology since 1960. Geomorphology **216** : 263–282. DOI: 10.1016/j.geomorph.2014.04.012

Yanites BJ, Kesler SE. 2015. A climate signal in exhumation patterns revealed by porphyry copper deposits. Nature Geoscience **advance online publication** DOI: 10.1038/ngeo2429 [online] Available from: http://www.nature.com/ngeo/journal/vaop/ncurrent/full/ngeo2429.html (Accessed 21 May 2015)

Appendix A

FastScape Input Files

as viewed in Eclipse

```
FastScape Input File for NAMIBIA 4101 uniform precipitation (NAMBI.bil; 4/22/2015)

Number of threads/cores to use

num_threads = 8

restart = -2
convert = little_endian
DEM = NAMBI.bil

Basic geometry (xl = 4101 * 89.76281625, yl = 4101 *89.76281625)

nx =   4101
ny =   4101
xl =    368117.3094413
yl =    368117.3094413

Time stepping

dt =    100000
nstep =   500
nfreq =    50

Incision law

law = 2
m =   0.400000
n = 0.9
kf =   0.10000E-05

Boundary conditions

boundary_condition = 0001

Precipitation

precipitation_n = 1
precipitation_v1 =    0.200

Uplift rate

uplift_n = 0
uplift_v1 =   0.010E-03

Plotting options

plot_all = 0
plot_topo = 0
plot_rate = 1
plot_catchment = 0
plot_slope = 0
plot_chi = 1
plot_DEM = 2
vtk = 1


```

```
FastScape Input File for NAMIBIA 4101 Bilinear Precipitation (NAMBI.bil; 4/22/2015)

Number of threads/cores to use

num_threads = 8

restart = -2
convert = little_endian
DEM = NAMBI.bil

Basic geometry (xl = 4101 * 89.76281625, yl = 4101 *89.76281625)

nx =   4101
ny =   4101
xl =    368117.3094413
yl =    368117.3094413

Time stepping

dt =    100000
nstep =   500
nfreq =    50

Incision law

law = 2
m =   0.400000
n = 0.9
kf =   0.10000E-05

Boundary conditions

boundary_condition = 0001

Precipitation

precipitation_n = 1
precipitation_v1 =    0.00500
precipitation_v2 =    0.25
precipitation_v3 =    0.45
precipitation_v4 =    0.005

Uplift rate

uplift_n = 0
uplift_v1 =   0.010E-03

Plotting options

plot_all = 0
plot_topo = 0
plot_rate = 1
plot_catchment = 0
plot_slope = 0
plot_chi = 1
plot_DEM = 2
vtk = 1


```

```
FastScape Input File for HIMALAYA 4101 (N4101.bil; 6/3/2015)

Number of threads/cores to use

num_threads = 8

restart = -2
convert = little_endian
DEM = N4101.bil

Basic geometry (xl = 4101 * 91.66406561, yl = 4101 *91.66406561)

nx =   4101
ny =   4101
xl =    375914.33306661
yl =    375914.33306661

Time stepping

dt =    100000.
nstep =    500
nfreq =    250


Incision law

law = 2
m =   0.4
n = 0.9
kf =   0.1E-05

Boundary conditions

boundary_condition = 1000

Precipitation

precipitation_n = 0
precipitation_v1 =   1.0


Uplift rate

!/uplift_start/
uplift=0.010
if (time.gt.1.e5) uplift=uplift/1000.
!/uplift_stop/

plot_all = 0
plot_topo = 0
plot_rate = 1
plot_catchment = 0
plot_slope = 0
plot_chi = 1
plot_DEM = 2
vtk = 1


```

FastScape.in

```
FastScape Input File for NAMIBIA 1601 (NSMAL.bil; 4/22/2015)

Number of threads/cores to use

num_threads = 8

restart = -2
convert = little_endian
DEM = NSMAL.bil

Basic geometry (xl = 1601 * 89.76281625, yl = 1601 *89.76281625)

nx =   1601
ny =   1601
xl =    143710.2688163
yl =    143710.2688163

Time Stepping

dt =    100000
nstep =    500
nfreq =    50

Incision law

law = 2
m =   0.400000
n = 0.9
kf =   0.10000E-05

Boundary conditions

boundary_condition = 0001

Precipitation

precipitation_n = 1
precipitation_v1 =    0.200

Uplift rate

uplift_n = 0
uplift_v1 =   0.010E-03

Plotting options

plot_all = 0
plot_topo = 0
plot_rate = 1
plot_catchment = 0
plot_slope = 0
plot_chi = 1
plot_DEM = 2
vtk = 1


```

```
FastScape Input File for HIMALAYA 1601 (HSMAL.bil; 5/31/2015)

Number of threads/cores to use

num_threads = 8

restart = -2
convert = little_endian
DEM = HSMAL.bil

Basic geometry (xl = 1601 * 91.66406561, yl = 1601 *91.66406561)

nx =   1601
ny =   1601
xl =    146754.1690416
yl =    146754.1690416

Time stepping

dt =    100000.
nstep =    500
nfreq =    50


Incision law

law = 2
m =   0.400000
n = 0.9
kf =   0.10000E-05

Boundary conditions

boundary_condition = 0001

Precipitation

precipitation_n = 0
precipitation_v1 =   1.0


Uplift rate

!/uplift_start/
uplift=0.010
if (time.gt.1.e5) uplift=uplift/1000.
!/uplift_stop/

Plotting options

plot_all = 0
plot_topo = 0
plot_rate = 0
plot_catchment = 0
plot_slope = 0
plot_chi = 1
plot_DEM = 2
vtk = 1


```

```
FastScape Input File for Namibia ASTER (NASTI.bil; 4/30/2015)

Number of threads/cores to use

num_threads = 8

restart = -2
convert = little_endian
DEM = NASTI.bil

Basic geometry (xl = 4794 * 29.98623302, yl = 4794 *29.98623302)

nx =   4794
ny =   4794
xl =    143754.00109788
yl =    143754.00109788

Time Stepping

dt =    100000
nstep =    500
nfreq =    50

Incision law

law = 2
m =   0.4
n = 0.9
kf =   0.1E-05

Boundary conditions

boundary_condition = 0001

Precipitation

precipitation_n = 0
precipitation_v1 =    0.200


Uplift rate

uplift_n = 0
uplift_v1 =   0.010E-03

Plotting options

plot_all = 0
plot_topo = 0
plot_rate = 0
plot_catchment = 0
plot_slope = 0
plot_chi = 1
plot_DEM = 2
vtk = 0


```

```
FastScape Input File for Himalaya ASTER (HASTI.bil; 5/31/2015)

Number of threads/cores to use

num_threads = 8

restart = -2
convert = little_endian
DEM = HASTI.bil

Basic geometry (xl = 4747 * 30.92208078, yl = 4747 * 30.92208078)

nx =   4747
ny =   4747
xl =    146787.11746266
yl =    146787.11746266

Time stepping

dt =    100000.
nstep =    500
nfreq =    250


Incision law

law = 2
m =   0.400000
n = 0.9
kf =   0.10000E-05

Boundary conditions

boundary_condition = 0001

Precipitation

precipitation_n = 0
precipitation_v1 =   1.0


Uplift rate

!/uplift_start/
uplift=0.010
if (time.gt.1.e5) uplift=uplift/1000.
!/uplift_stop/

Plotting options

plot_all = 0
plot_topo = 0
plot_rate = 0
plot_catchment = 0
plot_slope = 0
plot_chi = 1
plot_DEM = 2
vtk = 0


```